INTERNATIONAL JOURNAL OF MODERN ENGINEERING

Fall/Winter 2018
Volume 19, No. 1

WWW.IJME.US
Print ISSN: 2157-8052
Online ISSN: 1930-6628

The Leading Journal of Engineering, Applied Science and Technology

THE LEADING JOURNAL OF ENGINEERING, APPLIED SCIENCE, AND TECHNOLOGY

www.ijme.us

Print ISSN: 2157-8052
Online ISSN: 1930-6628

www.iajc.org

INTERNATIONAL JOURNAL OF MODERN ENGINEERING

ABOUT IJME:

- IJME was established in 2000 and is the first and official flagship journal of the International Association of Journal and Conferences (IAJC).
- IJME is a high-quality, independent journal steered by a distinguished board of directors and supported by an international review board representing many well-known universities, colleges and corporations in the U.S. and abroad.
- IJME has an impact factor of **3.00**, placing it among the top 100 engineering journals worldwide, and is the #1 visited engineering journal website (according to the National Science Digital Library).

OTHER IAJC JOURNALS:

- The International Journal of Engineering Research and Innovation (IJERI)
  For more information visit www.ijeri.org
- The Technology Interface International Journal (TIIJ).
  For more information visit www.tiij.org

IJME SUBMISSIONS:

- Manuscripts should be sent electronically to the manuscript editor, Dr. Philip Weinsier, at philipw@bgsu.edu.

  For submission guidelines visit www.ijme.us/submissions

TO JOIN THE REVIEW BOARD:

- Contact the chair of the International Review Board, Dr. Philip Weinsier, at philipw@bgsu.edu.

  For more information visit www.ijme.us/ijme_editorial.htm

INDEXING ORGANIZATIONS:

- IJME is currently indexed by 22 agencies. For a complete listing, please visit us at www.ijme.us.

Contact us:

Mark Rajai, Ph.D.

Editor-in-Chief
California State University-Northridge
College of Engineering and Computer Science
Room: JD 4510
Northridge, CA 91330
Office: (818) 677-5003
Email: mrajai@csun.edu

www.tiij.org

www.ijeri.org

INTERNATIONAL JOURNAL OF MODERN ENGINEERING

The INTERNATIONAL JOURNAL OF MODERN ENGINEERING (IJME) is an independent, not-for-profit publication, which aims to provide the engineering community with a resource and forum for scholarly expression and reflection.

IJME is published twice annually (fall and spring issues) and includes peer-reviewed research articles, editorials, and commentary that contribute to our understanding of the issues, problems, and research associated with engineering and related fields. The journal encourages the submission of manuscripts from private, public, and academic sectors. The views expressed are those of the authors and do not necessarily reflect the opinions of the IJME editors.

EDITORIAL OFFICE:

Mark Rajai, Ph.D.
Editor-in-Chief
Office: (818) 677-2167
Email: ijmeeditor@iajc.org
Dept. of Manufacturing Systems
Engineering & Management
California State University-
Northridge
18111Nordhoff Street
Northridge, CA 91330-8332

THE INTERNATIONAL JOURNAL OF MODERN ENGINEERING EDITORS

TABLE OF CONTENTS

Editorial Review Board Members

Mohammed Abdallah	State University of New York (NY)
Nasser Alaraje	Michigan Tech (MI)
Ali Alavizadeh	Purdue University Northwest (IN)
Ammar Al-Farga	University of Jiangnan (CHINA)
Aly Mousaad Aly	Louisiana State University (LA)
Paul Akangah	North Carolina A&T State University (NC)
Lawal Anka	Zamfara AC Development (NIGERIA)
Jahangir Ansari	Virginia State University (VA)
Kevin Berisso	Ohio University (OH)
Pankaj Bhambri	Guru Nanak Dev Engineering (INDIA)
Michelle Brodke	Bowling Green State University (OH)
Shaobiao Cai	Penn State University (PA)
Rajab Challoo	Texas A&M University Kingsville (TX)
Vigyan Chandra	Eastern Kentucky University (KY)
Isaac Chang	Illinois State University (IL)
Shu-Hui (Susan) Chang	Iowa State University (IA)
Hans Chapman	Morehead State University (KY)
Rigoberto Chinchilla	Eastern Illinois University (IL)
Sanjeevi Chitikeshi	Murray State University (KY)
Phil Cochrane	Indiana State University (IN)
Curtis Cohenour	Ohio University (OH)
Emily Crawford	Southern Wesleyen University (SC)
Brad Deken	Southeast Missouri State University (MO)
Dongyang (Sunny) Deng	North Carolina A&T State University (NC)
Z.T. Deng	Alabama A&M University (AL)
Sagar Deshpande	Ferris State University (MI)
David Domermuth	Appalachian State University (NC)
Dongliang Duan	University of Wyoming (WY)
Ryan Dupont	Utah State University (UT)
Marilyn Dyrud	Oregon Institute of Technology (OR)
Mehran Elahi	Elizabeth City State University (NC)
Ahmed Elsawy	Tennessee Technological University (TN)
Rasoul Esfahani	DeVry University (OH)
Morteza Firouzi	University of Technology (MALAYSIA)
Ignatius Fomunung	University of Tennessee Chattanooga (TN)
Ahmed Gawad	Zagazig University EGYPT)
Marvin Gonzalez	College of Charleston (SC)
Mohsen Hamidi	Utah Valley University (UT)
Mamoon Hammad	Abu Dhabi University (UAE)
Gene Harding	Purdue Polytechnic (IN)
Bernd Haupt	Penn State University (PA)
Youcef Himri	Safety Engineer in Sonelgaz (ALGERIA)
Delowar Hossain	City University of New York (NY)
Xiaobing Hou	Central Connecticut State University (CT)
Shelton Houston	University of Louisiana Lafayette (LA)
Kun Hua	Lawrence Technological University (MI)
Ying Huang	North Dakota State University (ND)
Charles Hunt	Norfolk State University (VA)
Dave Hunter	Western Illinois University (IL)
Christian Bock-Hyeng	North Carolina A&T University (NC)
Pete Hylton	Indiana University Purdue (IN)
Ghassan Ibrahim	Bloomsburg University (PA)
John Irwin	Michigan Tech (MI)
Toqeer Israr	Eastern Illinois University (IL)
Sudershan Jetley	Bowling Green State University (OH)
Rex Kanu	Ball State University (IN)
Reza Karim	North Dakota State University (ND)
Satish Ketkar	Wayne State University (MI)
Manish Kewalramani	Abu Dhabi University (UAE)
Tae-Hoon Kim	Purdue University Northwest (IN)
Chris Kluse	Bowling Green State University (OH)
Doug Koch	Southeast Missouri State University (MO)
Sally Krijestorac	Daytona State College (FL)
Chakresh Kumar	Uttar Pradesh Tech University (INDIA)
Zaki Kuruppalil	Ohio University (OH)
Edward Land	Johns Hopkins Medical Institute
Shiyoung Lee	Penn State University Berks (PA)
Soo-Yen Lee	Central Michigan University (MI)
Chao Li	Florida A&M University (FL)
Jimmy Linn	Eastern Carolina University (NC)
Dale Litwhiler	Penn State University (PA)
Guoxiang Liu	University of North Dakota (ND)
Louis Liu	University of New Orleans (LA)
Peng Liu	Washington State University (WA)
Mani Manivannan	ARUP Corporation
G.H. Massiha	University of Louisiana (LA)
Thomas McDonald	University of Southern Indiana (IN)
David Melton	Eastern Illinois University (IL)
Shokoufeh Mirzaei	Cal State Poly Pomona (CA)
Sam Mryyan	Excelsior College (NY)
Jessica Murphy	Jackson State University (MS)
Wilson Naik	University of Hyderabad (INDIA)
Arun Nambiar	California State University Fresno (CA)
Aurenice Oliveira	Michigan Tech (MI)
Troy Ollison	University of Central Missouri (MO)
Reynaldo Pablo	Indiana University-Purdue University (IN)
Basile Panoutsopoulos	Community College of Rhode Island (RI)
Shahera Patel	Sardar Patel University (INDIA)
Jose Pena	Purdue University Calumet (IN)
Thongchai Phairoh	Virginia State University (VA)
Huyu Qu	Honeywell Corporation
John Rajadas	Arizona State University (AZ)
Vijaya Ramnath	Sri Sairam Engineering College (CHENNAI)
Desire Rasolomampionona	Warsaw University of Tech (POLAND)
Mohammad Razani	New York City College of Tech (NY)
Sangram Redkar	Arizona State University-Poly (AZ)
Michael Reynolds	University of Arkansas Fort Smith (AR)
Nina Robson	California State University-Fullerton (CA)
Marla Rogers	Wireless Systems Engineer
Dale Rowe	Brigham Young University (UT)
Karen Ruggles	DeSales University (PA)
Anca Sala	Baker College (MI)
Alex Sergeyev	Michigan Technological University (MI)
Balaji Sethuramasamyraja	California State University Fresno (CA)
Mehdi Shabaninejad	Zagros Oil and Gas Company (IRAN)
Hiral Shah	St. Cloud State University (MN)
Ehsan Sheybani	Virginia State University (VA)
Mojtaba Shivaie	Shahrood University of Technology (IRAN)
Musibau Shofoluwe	North Carolina A&T State University (NC)
Siles Singh	St. Joseph University Tanzania (AFRICA)
Ahmad Sleiti	University of North Carolina Charlotte (NC)
Amit Solanki	C.U. Shah University (INDIA)
Jiahui Song	Wentworth Institute of Technology (MA)
Yuyang Song	Toyota Corporation
Carl Spezia	Southern Illinois University (IL)
Michelle Surerus	Ohio University (OH)
Jalal Taheri	Bostan Abad Islamic Azad University (IRAN)
Harold Terano	Camarines Sur Polytechnic (NABUA)
Sanjay Tewari	Louisiana Tech University (LA)
Li-Shiang Tsay	North Carolina A&T State University (NC)
Vassilios Tzouanas	University of Houston Downtown (TX)
Jeff Ulmer	University of Central Missouri (MO)
Abraham Walton	Purdue University (IN)
Haoyu Wang	Central Connecticut State University (CT)
Jyhwen Wang	Texas A&M University (TX)
Liangmo Wang	Nanjing University of Science/Tech (CHINA)
Boonsap Witchayangkoon	Thammasat University (THAILAND)
Alex Wong	Digilent Inc.
Shuju Wu	Central Connecticut State University (CT)
Baijian "Justin" Yang	Ball State University (IN)
Eunice Yang	University of Pittsburgh Johnstown (PA)
Mijia Yang	North Dakota State University (ND)
Xiaoli (Lucy) Yang	Purdue University Northwest (IN)
Faruk Yildiz	Sam Houston State University (TX)
Yuqiu You	Morehead State University (KY)
Pao-Chiang Yuan	Jackson State University (MS)
Biao Zhang	US Corporate Research Center ABB INC.
Jinwen Zhu	Missouri Western State University (MO)

DESIGN AND ANALYSIS OF BLAST-WAVE SENSORS

Jason M Kluga, Northern Illinois University; Ibrahim M. Abdel-Motaleb, Northern Illinois University

Abstract

Accurate blast sensors are critical for studying and monitoring nuclear explosions, jet engine testing, rocket engine testing, space exploration, oil and natural gas exploration, industrial safety, dams, tunnels, road construction and demolition, along with many other applications. These applications require the use of sensors that can withstand extreme forces. A blast wave resulting from an explosion is known as the Friedlander Waveform. The Friedlander Waveform is characterized by a positive pressure spike followed by a negative pressure. The pressure then decays, oscillating between positive and negative values. A full-range blast sensor should withstand up to 300 kPa and be able to measure both positive and negative pressures.

In this study, the authors looked at two 7-cm tall sensors made using 4340 Steel. One had a circular cross-section and the other had a rectangular cross-section. Each was surrounded by 12 equally spaced cantilevers with the dimensions 0.2x1x7 cm for the cylindrical sensor and 0.25x1x7 cm for the rectangular sensor. The separation between the cantilevers and the pillars was 0.3 cm for both devices. The pillar and the cantilevers for each sensor were fixed on a silica base. The capacitance between a cantilever and the pillar determines the magnitude of the pressure on this particular cantilever. For the cylindrical sensor, the cantilever that has the largest change in capacitance determines the direction of the blast.

The performance of the sensors was simulated and analyzed using COMSOL, a finite element, multi-physics, numerical analysis program. Cantilever displacement, strain energy density, volumetric strain, and the von Mises stress were simulated under 300 kPa of pressure. Capacitance as a function was simulated for the two sensors. The pressure varied from 0-300 kPa. The results showed that, at 300 kPa, the maximum displacement was 0.08 cm, the strain energy density was $2.25\text{x}10^5$ J/m^3, the volumetric strain was $0.6\text{x}10^{-3}$ for the cylindrical sensor and $1\text{x}10^{-3}$ for the rectangular sensor, and the von Mises stress was about $2.5\text{x}10^8$ N/m^2. The capacitance measured at the maximum pressure was found to be 35.6 pF for the cylindrical and 31.5 pF for the rectangular sensor. The study proved that both sensors were able to withstand the maximum blast pressure without failure or fatigue.

Introduction

Blast waves are different from hurricane pressure waves in magnitude and property. Because of the extreme high pressure of the blast waves, it is hard to develop a sensor for this type of pressure that can reach 300 kPa. In addition, the variation in blast wave magnitude and speed are highly variable. Therefore, reliable and accurate blast sensors that can withstand such extreme conditions are difficult to develop, but they are critically needed. These sensors are essential for applications related to monitoring nuclear explosions, jet engine testing, rocket engine design and testing, space exploration, oil and natural gas exploration, industrial safety, construction of dams, tunnels, and roads, and many other applications that deal with extreme pressures. Because of the extreme forces resulting from the blast, using common silicon-based microelectromechanical systems (MEMS) may not be practical. Therefore, a new technique for building such devices would be desirable.

A blast wave resulting from an explosion is known as the Friedlander Waveform (Goel & Matsagar, 2014). Figure 1 shows that the wave is a high-frequency oscillating wave, with a sharp spike of supersonic pressure created at the front of the wave. This spike is followed by a negative pressure that is many orders of magnitude lower in strength. The pressure then decays, oscillating between positive and negative pressures, until it disappears.

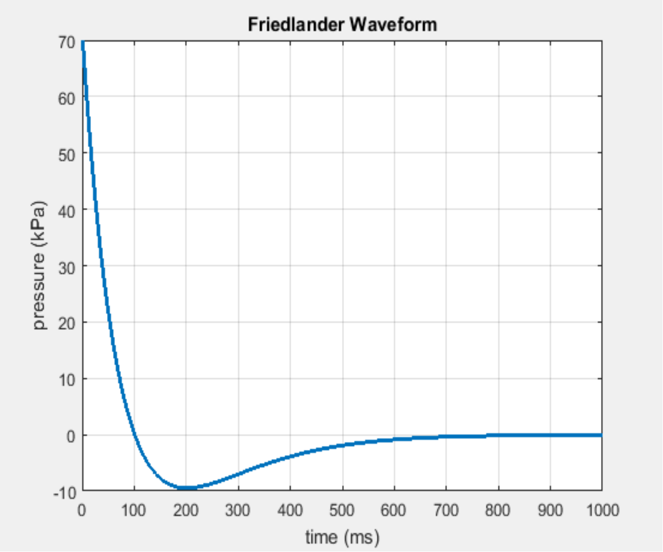

Figure 1. Basic morphology of the Friedlander waveform.

The rapid change in pressure from a spike to a vacuum causes more destruction than the blast peak itself. This waveform explains the severe destructive nature of blast waves that put them in a separate category from just high-wind conditions. The blast pressure as a function of time can be expressed by Equation 1 (Goel & Matsagar, 2014):

$$P(t) = P_s\left(e^{\left(-\frac{t}{t^*}\right)}\right)\left(1 - \frac{t}{t^*}\right) \tag{1}$$

where, P_S is the maximum pressure (static overpressure) of the wave or the initial spike; t is time; and, t^* corresponds to the blast wave lag.

The spike is followed by a dynamic pressure, which fluctuates rapidly and can be immensely destructive. The maximum of the static overpressure of a nuclear blast wave can vary from just under 10 kPa for distant and weak blasts to over 300 kPa close to the origin of a blast (US Department of Health & Human Sciences, 2015). Therefore, a blast sensor should be optimized to function between these pressures. In this paper, the design and analysis of two capacitance-based blast sensors that can withstand a pressure up to 300 kPa are reported. Two different sensors were designed: the first has cylindrical geometry and the second has rectangular geometry. The sensors were designed and analyzed using the finite element, multi-physics, numerical analysis program, COMSOL. This is a ground work for a new class of blast sensors that can be used in the previously mentioned applications.

Geometry

Figure 2 shows the geometries of the cylindrical sensors that were used in COMSOL simulation and analysis. The cylindrical sensor consists of 12 beveled cantilevers surrounding a central cylindrical pillar, with a gap of 0.3 cm between each cantilever and the pillar. The cantilevers and the pillar are all 7 cm each. They are embedded 1.5 cm into a silica base which is 3 cm thick. The cantilevers and the pillar thus rise above the silica to a height of 5.5 cm. The beveled cantilevers measure 1 cm in mean width, spaced evenly with just over 0.4 cm distance from each other. They are 0.2 cm thick and 7 cm tall. The radius of the cylindrical pillar is 2.3 cm and the inner radius of the cantilevers is 2.6 cm. The outer radius of the cantilevers is 2.8 cm. Air functions as the dielectric between the cantilevers and the pillars.

The rectangular sensor, shown in Figure 3, has a square pillar with a side length of 4.6 cm. The pillar was surrounded by 12 unbeveled cantilevers. The separation between the cantilevers and the pillar was 0.3 cm. This separation was chosen to ensure that the sensor could operate at 300 kPa. The cantilevers were 1 cm wide and 0.25 cm thick. They were also 7 cm tall and embedded into silica to a depth of 1.5 cm. This left the cantilevers exposed by 5.5 cm. The width of the cantilevers was 1 cm, and they were placed three per pillar face. The distance between the cantilevers was 0.53 cm, and the far edges of the end cantilevers were placed 0.26 cm from the edge of the pillar face. The cantilevers and the pillars for both sensors were made from 4340 Steel with a tensile strength of 745 MPa, a yield strength of 470 MPa, a bulk modulus of 140 GPa, and a shear modulus of 80 GPa. The property of the silica was taken from the COMSOL library.

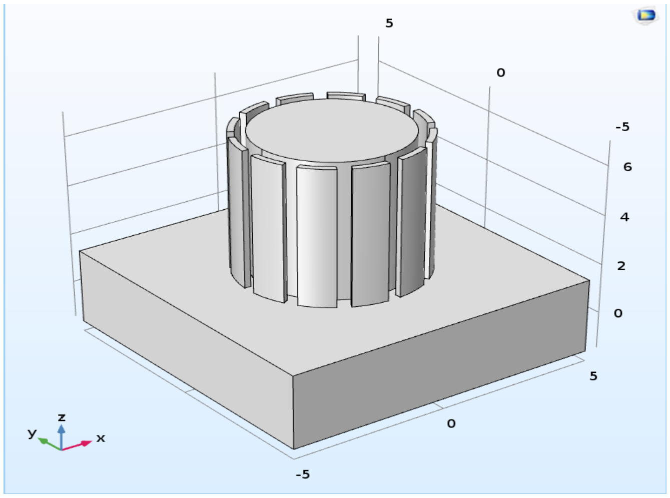

Figure 2. Geometry of the cylindrical sensor used in COMSOL simulation.

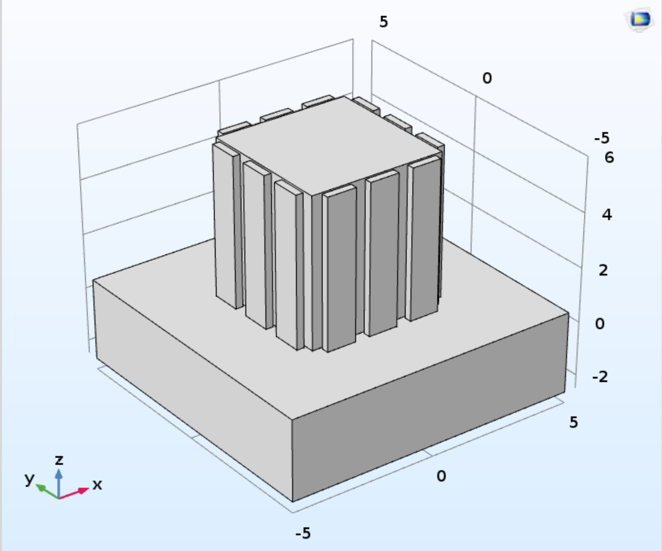

Figure 3. Geometry of the rectangular sensor used in COMSOL simulation.

Numerical Simulation and Analysis

A maximum pressure of 300 kPa was applied to the circular sensor. For the rectangular sensor, the pressure was applied along a 45-degree angle from the face. Using COMSOL, the cantilever displacement, strain energy density, volumetric strain, and the von Mises stress were simulated. Figure 4 shows the displacement at every point on the cantilevers, when a pressure of 300 kPa was applied to the cylindrical sensor. Figure 5 shows the displacement for the rectangular sensor, when the same maximum pressure was applied. The two figures show the maximum displacement for the sensors to be about 0.8 mm at the tip of the cantilever.

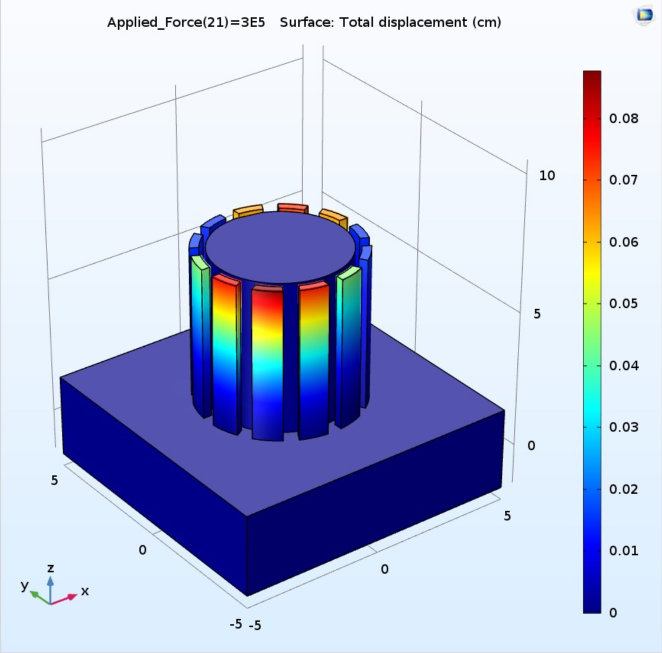

Figure 4. Displacement of the cylindrical sensor cantilevers under a pressure of 300 kPa.

The elastic energy density is defined as the recoverable energy stored in an elastic material per unit volume, which can be expressed by Equation 2 (Senturia, 2001):

$$W = \frac{1}{2} . \frac{1}{\Delta x \Delta y \Delta z} \iiint \begin{matrix} (\sigma_x{}^{\epsilon}{}_x + \sigma_y{}^{\epsilon}{}_y + \sigma_z z + \tau_{yz} \gamma_{yz} \\ + \tau_{zx} \gamma_{zx} + \tau_{xy} \gamma_{xy}) dx dy dz \end{matrix} \tag{2}$$

where, $\acute{o}_x$, $\acute{o}_y$, and $\acute{o}_z$ are the stresses along the principal axes x, y, and z, respectively; ϵ_x, ϵ_y, and ϵ_z are the corresponding strains; $\hat{o}_{zx}$, $\hat{o}_{xy}$, and $\hat{o}_{yz}$ are the shear stresses along the principal axes x, y, and z, respectively; $\tilde{a}_{zx}$, $\tilde{a}_{xy}$, and $\tilde{a}_{yz}$ are the corresponding shear strains; and, *dx, dy,* and *dz* are the deformations along the x, y, and z axes.

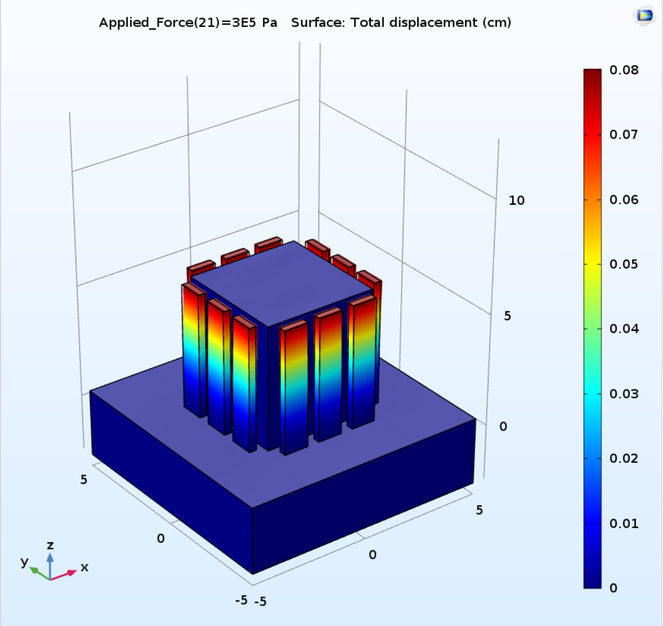

Figure 5. Displacement of the rectangular sensor cantilevers under a pressure of 300 kPa.

The elastic energy density was simulated for both sensors under the maximum pressure. Figure 6 shows the results for the cylindrical sensor, and Figure 7 for the rectangular sensor. The figures show that the strain energy density reached a maximum value of about 2.25×10^5 J/m^3. It appears that both sensors had the same elasticity properties, since they had the same material.

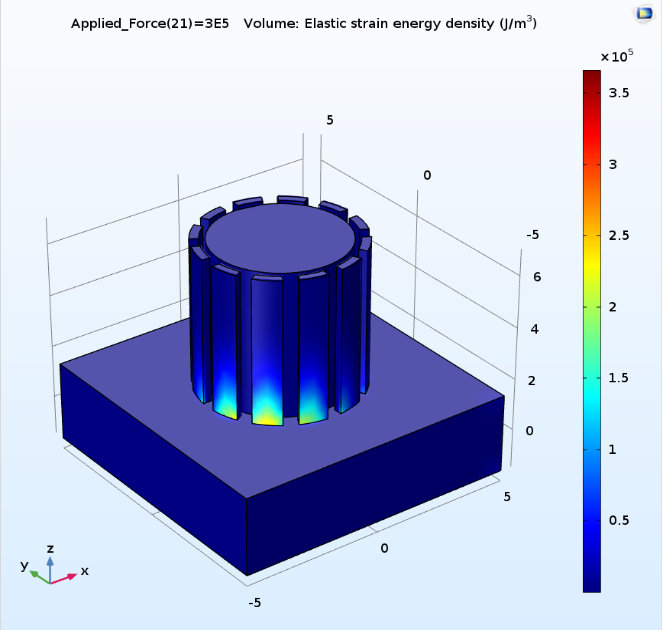

Figure 6. Elastic strain energy density of the cylindrical sensor cantilevers under a pressure of 300 kPa.

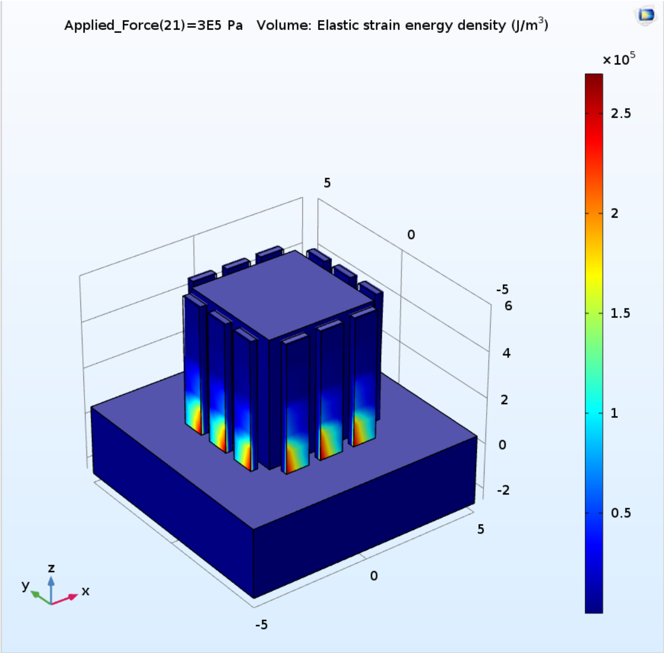

Figure 7. Elastic strain energy density of the rectangular sensor cantilevers under a pressure of 300 kPa.

The volumetric strain is defined as the unit change in volume, or the change in volume over the original volume. The volumetric strain can be obtained from Equation 3 (Kelly, 2015):

$$\frac{\Delta V}{V} = \left(1 + \epsilon_x\right)\left(1 + \epsilon_y\right)\left(1 + \epsilon_z\right) - 1 \tag{3}$$

where, V is the original volume of the material and ΔV is the change in the volume due to stress.

Figures 8 and 9 shows the simulated volumetric strain for the cylindrical and rectangular sensors, respectively. The figures also show that the volumetric strain for the cylindrical sensor was about $0.6 \mathrm{x} 10^{-3}$, while for the rectangular sensor the strain increased to about $1 \mathrm{x} 10^{-3}$. The smaller volumetric strain of the cylindrical may be a result of the curving of the cantilever, which better resisted deformation. The von Mises stress is the effective stress that combines the normal stress, the bending stress, the bending sheer stress, and the torsional sheer stress along all major axes. The value of the von Mises stress can be obtained from Equation 4 (von Mises stress, n.d.):

$$\sigma_{VM} = \left(\begin{array}{l} \frac{1}{2}\left[\left(\sigma_{xx} - \sigma_{yy}\right)^2 + \left(\sigma_{yy} - \sigma_{zz}\right)^2 + \left(\sigma_{zz} - \sigma_{xx}\right)^2\right] \\ +3\left(\tau_{xy}^2 + \tau_{yz}^2 + \tau_{zx}^2\right) \end{array} \right)^{1/2} \tag{4}$$

where, $ó_{xx}$, $ó_{yy}$, and $ó_{zz}$ are the stresses along the principal axes x, y, and z, respectively.

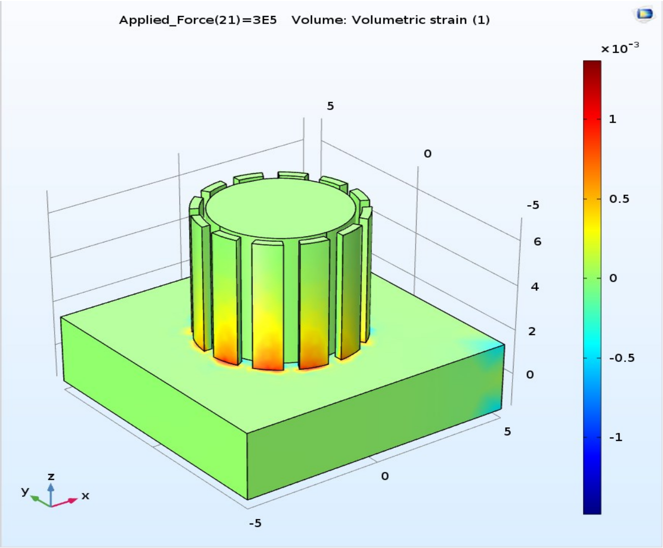

Figure 8. Volumetric strain of the cylindrical sensor cantilevers under a pressure of 300 kPa.

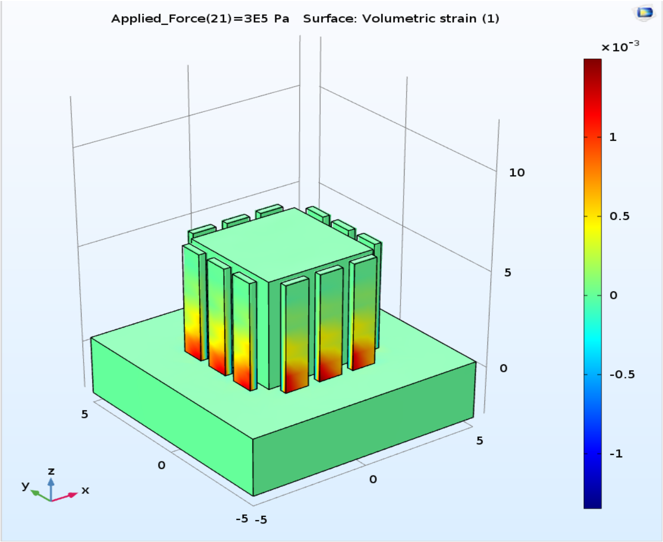

Figure 9. Volumetric strain of the rectangular sensor cantilevers under a pressure of 300 kPa.

The von Mises stress was simulated for both sensors when they were under 300 kPa of pressure. Figures 10 and 11 show the results. The results show that the maximum stress in the cantilevers was at the intersection with the silica plate. The maximum stress reached $2.5 \mathrm{x} 10^{8}$ N/m². The cantilevers thus bend more at the base than any other part of the device, which should alert the designer to ensure that steel yield will not be reached at the cantilever base.

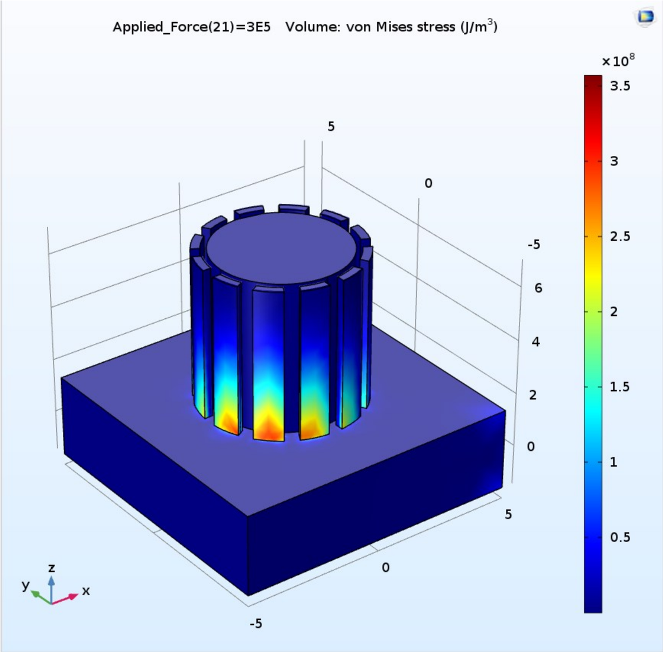

Figure 10. von Mises Stress in the cylindrical sensor under pressure of 300 kPa.

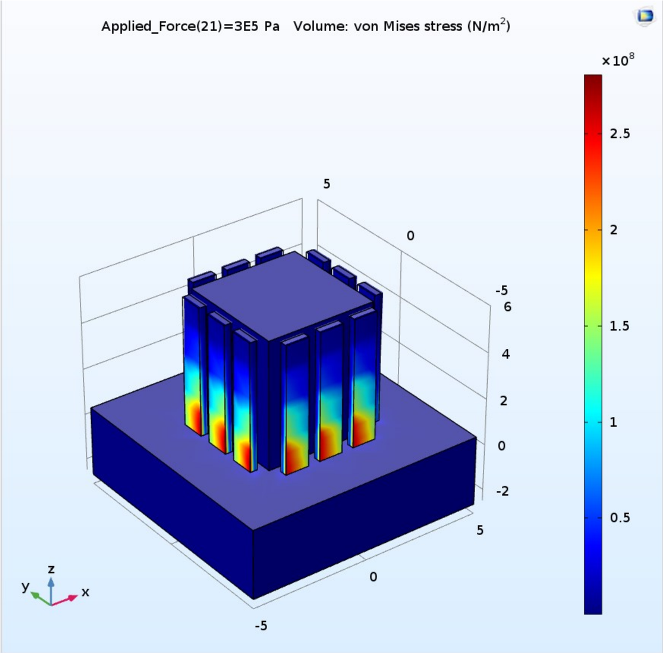

Figure 11. von Mises Stress in the rectangular sensor under pressure of 300 kPa.

Figures 12 and 13 show capacitance as a function of the pressure for the cylindrical sensor and the rectangular sensor, respectively. The results show that, at a pressure of 300 kPa, the capacitance reached about 35.6 pF for the circular sensor and about 31.5 pF for the square cross-section sensor. The results also show that the change in capacitance below the blast cutoff magnitude of 30 kPa was also detectable. For the cylindrical sensor, the capacitance at 30 kPa was about 33.7 pF, while for the rectangular sensor, the capacitance was about 30 pF at the same pressure. Therefore, both sensors are able to differentiate between a pressure due to a hurricane and that due to a blast.

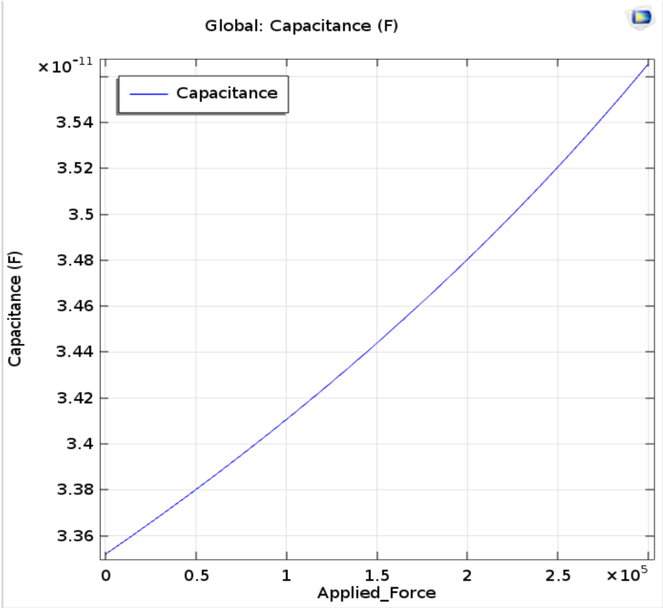

Figure 12. Capacitance versus applied force (in Pascale) for the cylindrical sensor.

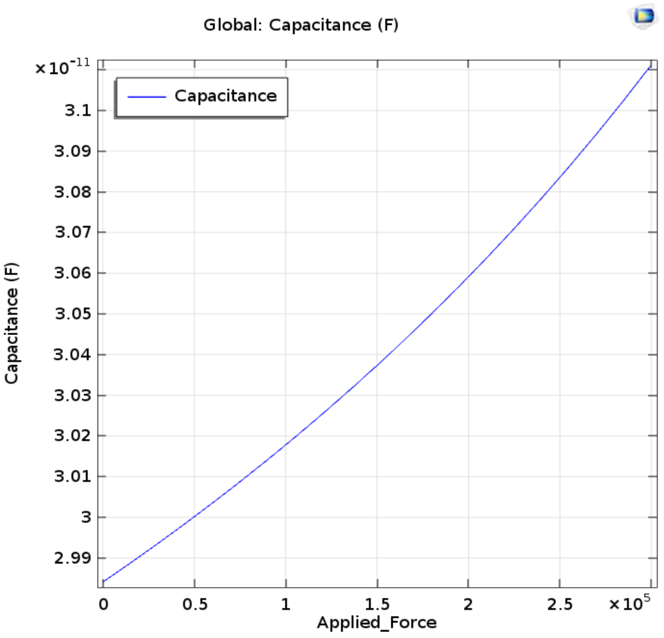

Figure 13. Capacitance versus applied force (in Pascale) for the rectangular sensor.

The high sensitivity of the sensors allows for differentiating between just a wind pressure and a blast. The differentiation can be determined from two factors: If the magnitude of the pressure is below 30 kPa, the pressure would be the result of a wind storm; or, if the pressure is above 30 kPa, it would be due to a blast. The second is that, if there is a negative pressure after the peak pressure, then the pressure is due to a blast. One advantage of the devices from this study is that they can detect negative pressure.

Conclusions

The main purpose of this study was to design and test two sensors for their ability to withstand the maximum pressure of a blast. Therefore, this was considered ground-breaking work for determining the feasibility of building such sensors. The study showed that the cylindrical sensor could determine direction very accurately. Therefore, it could be used to detect blasts of either nuclear explosions or hurricanes. The rectangular sensor could be used in blast testing, where the direction is known and the sensor face can be directed towards the direction of the blast. The study also showed that the back cantilevers were pushed away from the pillar, thereby reducing the total capacitance. Therefore, the correct way of using the sensors is to measure the capacitance for each cantilever. This would determine not only the direction of the pressure but also the existence of a negative pressure.

References

Goel, M. D., & Matsagar, V. (2014). Blast resistant design of structures. *Practice Periodical on Structural Design and Construction*, *19*(2), 04014007-1-04014007-9.

Kelly, P. (2015). *Solid mechanics, part I*. Retrieved from http://homepages.engineering.auckland.ac.nz/~pkel015/SolidMechanicsBooks/Part_I/

Senturia, S. D. (2001). *Mechanical design*. Norwell, MA: Kluwer Academic Publishers.

US Department of Health & Human Services. (2018, March 15), *Nuclear explosions: Weapons, improvised nuclear devices*. Retrieved from https://www.remm.nlm.gov/nuclearexplosion.htm

Von Mises stress. (n.d.). Retrieved from http://www.continuummechanics.org/vonmisesstress.html

Biographies

JASON KLUGA is an MS student at Northern Illinois University. He works in the area of numerical simulation of sensors and electronic devices. Jason Kluga may be reached at jkluga1@niu.ed or Jason.Kluga@utas.utc.com

IBRAHIM M. ABDEL-MOTALEB, Ph.D., PE, is a professor of electrical engineering and the director of the microelectronics laboratory at Northern Illinois University. He holds BS degrees in Electrical Engineering and Physics, both from Cairo University. He received his MS degree in physics from the University of Manitoba, Canada, and his PhD in electrical engineering from the University of British Columbia, Canada. His areas of expertise include fabrication, characterization, modeling of electronic devices and integrated circuits, electronic material growth and characterization, MEMS design and fabrication, and biomedical engineering instrumentation. Dr. Ibrahim may be reached at ibrahim@niu.edu

FLEXURAL DESIGN OF CONCRETE BEAMS WITH HIGH-STRENGTH REINFORCEMENT

Shane M. Palmquist, Western Kentucky University; Andrew D. Bell, Western Kentucky University;
Katy A. Bridges, Western Kentucky University

Abstract

In this study, the authors examined the ACI 318 Code methodology for flexural strength design of reinforced concrete beams with high-strength steel reinforcement conforming to ASTM A1035/A1035M-16. Tensile steel strains corresponding to strain limits for tension-controlled and transitional members were studied for beams with high-and normal-strength steel reinforcement. For normal-strength steel reinforcement typically corresponding to Grade 60 (410) and Grade 75 (520), the minimum tension-controlled steel strain is 0.005. ACI flexural members, however, may be designed with tensile strain as a low as 0.004. To provide the same level of structural safety for concrete beams with high-strength reinforcement, the strain limits per ACI 318 Code need to be increased, as compared to beams with normal-strength rebar. Having different ACI strain limits for high- and normal-strength steel reinforcement for members in flexure is necessary. However, this complicates the ACI resistance factor versus tensile-steel strain relationship. To simplify the resulting relationship, a modification will be proposed, which results in one simply expression that accounts for various strengths of grades of tensile-steel reinforcement. The resulting ACI modification provides a clear and consistent means of ensuring that all flexural members are designed to be under-reinforced by increasing the limiting tensile strain, based on the grade of the steel reinforcement.

The proposed modification to the strain limits for flexural members with high- and normal-strength reinforcement follows the procedures of ACI 318 and is discussed here in detail along with an examination of the results performed by others. An ultimate strain in the tensile reinforcement is proposed, which eliminates the need to determine the minimum steel ratio and is more consistent with the strain-limit approach for flexure in ACI 318. A numerical design example showing the application of the proposed modification is also presented.

Introduction

According to IBC-2018, the maximum allowable design strength of nonprestressed tendon steel reinforcement is 80 ksi (550 MPa) (IBC, 2018). This maximum was established in ACI 318-71 by Committee 318, since this steel strength is nearly equal to the product of the ultimate strain in the concrete, 0.003, and the modulus of elasticity of steel, 29,000 ksi (200 GPa) (ACI Committee 318, 1971). For nearly 50 years, this limitation has been in practice. At the time of implementation, this requirement worked well, since high-strength steel reinforcement was not available. In Europe, flexural rebar with a grade of 72.5 ksi (500 MPa) is commonly used, and the maximum permissible strength is 94.3 ksi (650 MPa).

In recent years, steel reinforcement with enhanced properties had been developed which may lead to the possibility of designers using steel reinforcement with greater strengths, as compared to traditional reinforcement (Faza, Kwok, & Salah, 2008; CRSI, 2017; Risser & Humphreys, 2008). High-strength steel reinforcement meeting the requirements of ASTM A1035/A1035M-16 has been developed (MMFX Technologies, 2012; MMFX Technologies, 2015; ASTM A1035/A1035M, 2016). Stress-strain characteristics including pre-peak and post-peak behavior are fundamentally different than the behavior of Grade 60 (410) steel reinforcement. Steels with enhanced-strength properties are stronger. However, they tend to lack a well-defined yield point. Up to a strain of about 0.0015, the stress-strain relationship for reinforcing steels is predominantly linear. This applies to both normal- and high-strength reinforcement. However, from a strain of about 0.0015 to 0.003, this relationship for high-strength steels gradually becomes nonlinear, as compared to normal-strength steels such as Grade 60 (410) and Grade 75 (520), which exhibit a more immediate plastic behavior. Normal-strength reinforcing steels tend to exhibit an initial stress-strain relationship that is linear elastic and is immediately followed by plastic-like behavior. High-strength steels tend to exhibit a stress-strain relationship that is initially linear elastic but, as strains increase, which becomes gradually nonlinear, eventually reaching a more plastic-like behavior.

Figure 1 presents typical stress-strain relationships for several different high-strength reinforcing steels, along with the stress-strain relationships for normal-strength reinforcing steels such as Grade 60 (410) steel and Grade 75 (520). Also presented in Figure 1 is the stress-strain relationship for traditional prestressing steel and the stress-strain relationship for high-strength steel, which is predominantly characterized by an initial linear-elastic behavior followed by a gradual nonlinear behavior that eventually reaches a more plastic-like behavior. The absence of a distinct yield plateau is typical of high-strength steel. Similar to normal-strength reinforcing steels, high-strength reinforcing steels are capable of achieving ultimate strains of up to 0.050 and higher before failure (Mast, Dawood, Rizkalla, & Zia, 2008). In general, as the strength of steel reinforcement increases, ductility decreases. High-strength steels have a reduced capacity to permanently deform before fracture and ultimately failure, as compared to normal-strength steel reinforcement. High-strength steels are capable of deforming considerably prior to failure and are considered to be ductile in comparison to normal concrete, which is a quasi-brittle material with limited ability to strain prior to the onset of cracking and eventual failure.

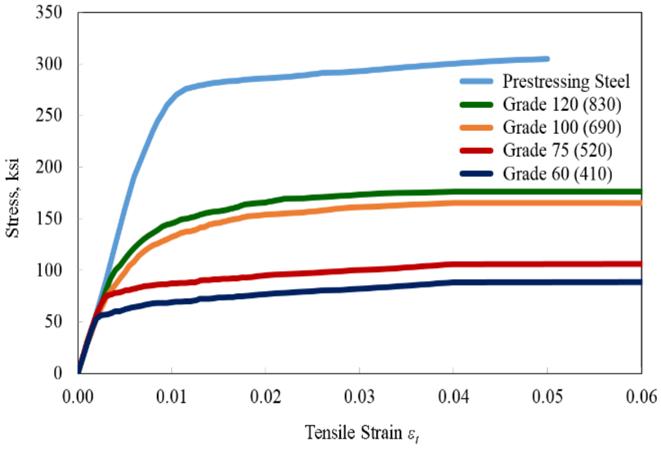

Figure 1. Material stress-strain behavior of reinforcing steels.

The ACI 318-14 Code limits the maximum yield strength of steel reinforcement to 80 ksi (550 MPa) (ACI Committee 318, 2014). A simplified elastic-plastic relationship and method was proposed for design purposes by Mast when designing flexural members with tensile steel reinforcement with a maximum yield strength up to 100 ksi (690 MPa) (Mast et al., 2008; Mast, 2007). Figure 2 shows that the simplified model consisted of an initial linear-elastic portion with a modulus of elasticity of 29,000 ksi (200 GPa) followed by a perfectly plastic plateau with a yield strength of 100 ksi (690 MPa). In the near future, Committee 318 will need to consider the use of high-strength reinforcing steels in the design of concrete structures. To increase the 80 ksi (550 MPa) yield strength limitation on reinforcing steel rebar used in flexural members in concrete structures as required by the current ACI Code, a modification of the proposed method by Mast is presented where flexural members with grade-reinforcing steels of up to 120 ksi (830 MPa) are considered (Mast et al., 2008; Mast, 2007). Figure 2 shows the proposed modification and the ACI limitation.

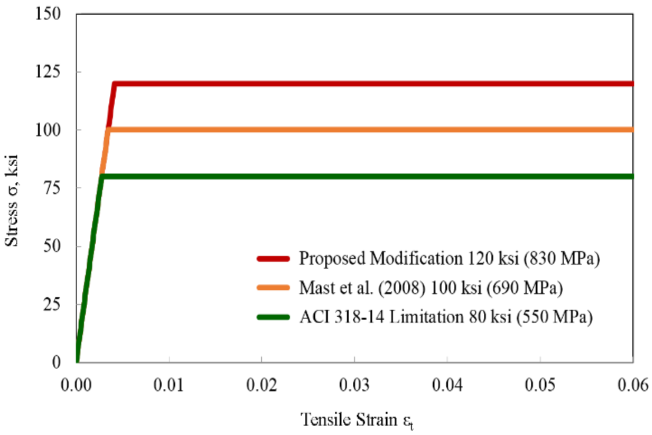

Figure 2. Elastic-plastic design relationship.

Throughout this paper, the authors present all numbers, equations, and tables using English units with soft metric conversions. The authors also propose increasing the yield strength limit for high-strength steel reinforcing bars in flexural members for tension only up to 120 ksi (830 MPa). A comparative numerical beam example showing the use of grade 60 (410), 75 (520), 100 (690), and 120 (830) tensile reinforcement is presented. Other reinforcing steels in flexural members, such as those used for compression and shear strength, need to follow current recommendations for strength as required by ACI 318. For reinforcing bars used in compression, the limit of 80 ksi (550 MPa) is reasonable, since the stress in the compression steel is controlled by the ultimate compressive strain in the concrete, which is specified by ACI 318 as 0.003 for the flexural design of reinforced concrete members. For the flexural beams studied here, concrete strengths up to 10,000 psi (70 MPa) were considered. Additional physical testing of actual concrete beams with high-strength reinforcement is needed for verification purposes.

Tensile Steel Ratio

In 1963, the ACI 318 Code required all flexural members to limit the tensile steel reinforcement ratio, ρ, to a maximum of 75 percent of the balanced steel ratio, ρ_b (ACI Committee 318, 1963). This requirement remained in the ACI Code for over 30 years. The current requirement for the upper-bound limit on the amount of tensile strain reinforcement was selected based on approximately 75 percent of the balanced tensile steel ratio. Currently, the actual upper-bound limit for the tensile steel ratio is 71.4 percent of the balance steel ratio, which corresponds to a minimum strain in the tensile steel of 0.004 (ACI Committee 318, 2014). According to the ACI 318 Code, the lower-bound limit on the amount of tensile steel reinforcement is provided by the lower limit on the steel ratio. The minimum reinforcement ratio of 200/f_y was based on flexural members having a minimum steel area of 0.5 percent of the strength cross-section, assuming Grade 40 (280) steel reinforcement, where f_y is the yield strength of the reinforcement in units of psi. In 1995, the ACI 318 Code modified this requirement for concrete compressive strengths greater than approximately 5000 psi (35 MPa) (ACI Committee 318, 1995). The current ACI requirement for the minimum steel ratio is presented in Equation 1:

$$\rho_{min} = \min\left(\frac{3\sqrt{f_c'}}{f_y}\ \frac{200}{f_y}\right) \tag{1}$$

where, f_c', the compressive strength of the concrete, and f_y both have units of psi.

Above concrete strengths of 4444 psi (30 MPa), the first quantity governs; below that strength, the second quantity governs. Based on the Whitney stress block for flexure, the tensile steel ratio for flexural members can be calculated Equation 2:

$$\rho = \frac{A_s}{bd} \tag{2}$$

where, A_s is the area of the tensile steel reinforcement, and *b* and *d* correspond to the beam width and beam depth from the compression face to the tensile steel, respectively.

Based on the equilibrium, where the tension force in the tensile steel reinforcement must be equal to the compression force of the Whitney stress block for a singularly reinforced concrete beam, the tensile steel ratio for flexural members can be determined from Equation 3:

$$\rho = 0.85\,\beta_1\left(\frac{f_c'}{f_y}\right)\left(\frac{\varepsilon_u}{\varepsilon_u + \varepsilon_t}\right) \tag{3}$$

where, β_1 is the ratio of the depth of the Whitney stress block to the distance from the compression face to the neutral axis; ε_u is the ultimate strain at the compression face of the beam section; and, ε_t is the strain in the tensile steel reinforcement.

From Equation 3, as the strain in the steel tensile reinforcement, ε_t, increases beyond the strain at yield, ε_y, the steel ratio, ρ, decreases below ρ_b. Figure 3 shows this inverse relationship, where the ratio ρ/ρ_b is plotted versus tensile steel strain for different grades of reinforcement strength.

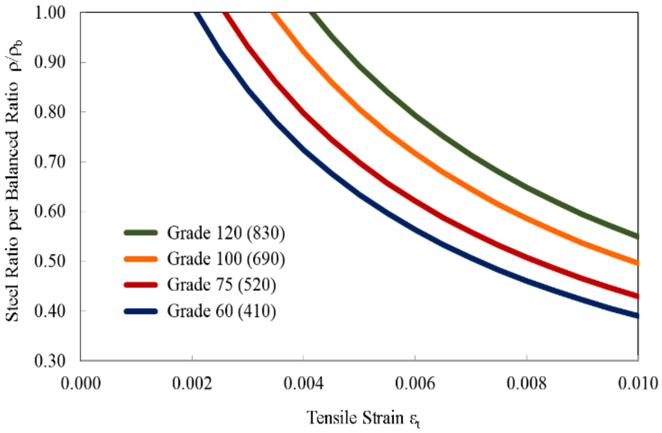

Figure 3. Steel ratio per balanced ratio versus tensile steel strain.

Tensile Steel Strain

Ultimate strength design, now referred to as strength design, as a methodology was first introduced in the ACI Code in 1963. Based on the balanced steel ratio, ρ_b, for flexural members, ACI beams were required to be under-reinforced, meaning that when the strain in the concrete at the compression face reached 0.003, the strain in the tension steel, ε_t, had to be significantly above the strain at yield, ε_y. At a concrete strain of 0.003, this is the ultimate strain in the concrete, ε_u, according to the ACI Code. This condition requires the tensile steel reinforcement to fail first and yield, prior to the concrete at the compression face from crushing. As a result, failure would be gradual where permanent deformation in the tensile rebar would occur and accumulate, prior to the failure of the concrete.

In 1995, the ACI 318 Code introduced into Appendix B an alternative requirement that limited the maximum steel ratio, ρ_{max}, to a minimum tensile strain in the reinforcement at the nominal-moment strength for flexure (ACI Committee 318, 1995). Prior to this, the maximum steel ratio was limited to a maximum of 75 percent of the balance steel ratio. A tension-controlled member was defined such that the tensile strain in the tension steel at nominal strength was equal to a minimum of 0.005 or greater. This corresponded to a resistance factor, ϕ, of 0.90. For flexural members, the tensile strain in the reinforcement was permitted to be as low as 0.004. However, as the tensile steel strain decreased from 0.005 to 0.004, the resistance factor for rectangular beam sections decreased linearly from 0.90 to 0.82, respectively. Flexural members with tensile strains equal to 0.004 to, but not including, 0.005 were referred to as transition-zone members, not tension-controlled members. Figure 4 presents the ACI strain limits for reinforced concrete members.

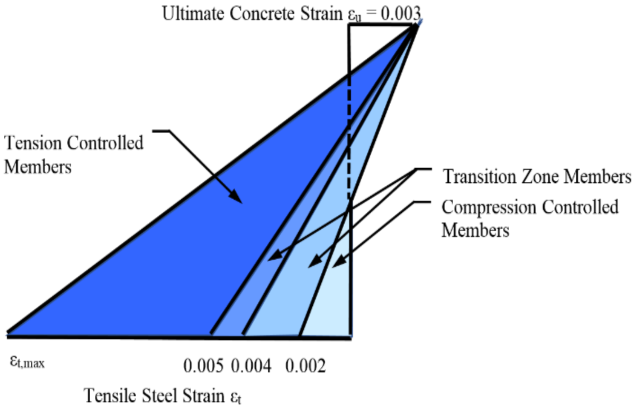

Figure 4. ACI tensile strain limits for reinforced concrete members.

Research supporting the change in the ACI 318 Code from the steel ratio requirement to a tensile steel strain requirement was based on studies using Grade 60 (410 MPa) rebar. However, this approach was extended and permitted for flexural members with Grade 75 (520) steel reinforcement, despite the difference in the strains at yield. For Grade 60 (410) steel reinforcement, the strain at yield is 0.00207. For Grade 75 (520) steel reinforcement, the strain at yield is 0.00259. The change in the strain at yield corresponds to a 25 percent increase in strain. In 2002, the ACI 318 Code made this alternative mandatory by moving Appendix B to the body of the ACI Code (ACI Committee 318, 2002). Thus, rather than designing flexural members on the basis of the maximum steel ratio, ρ_{max}, this was replaced by limits placed on the tensile steel strain, ε_t, in the tension reinforcement.

While this approach is practical and feasible for Grade 60 (410) steel reinforcement (and was deemed acceptable for Grade 75 (520) steel reinforcement), changes in strain limits are needed to ensure the same level of structural safety, if reinforcing steels with higher grades beyond 80 ksi (550 MPa) are to be used in practice for the flexural design of reinforced concrete members. Researchers have already proposed modifying the strain limits for tension reinforcement in flexural members (Mast et al., 2008; Shahrooz, Reis, Wells, Miller, Harries, & Russell, 2010). Mast et al. proposed modifying the existing strain limits for using Grade 100 (690) steel reinforcement meeting the requirements of ASTM A1035/A1035M in flexural members (2008). For Grade 100 (690) steel rebar, the strain at yield is 0.00345. This represents an increase in the strain at yield of 40 percent, in comparison to Grade 60 (410) steel reinforcement. Not increasing the strain limits would decrease the structural safety of the flexural member, potentially leading to more failures. When using tensile steel reinforcement that is Grade 100 (690), Mast el al. proposed increasing the strain limit for compression controlled members from 0.002 to 0.004 and for tension controlled members from 0.005 to 0.009 (2008). Thus, the 0.004 minimum strain limit for a flexure member would need to be increased to approximately 0.0065 for consistency. Similar results were reported by Shahrooz et al. for future updates to the AASHTO LRFD Bridge Design Specification (2010). For compression-controlled members, a recommendation was made to increase the strain limit from 0.002 to 0.004, which was the same as proposed by Mast et al. For tension-controlled members, a recommendation was made to increase the strain limit from 0.005 to 0.008.

Since the ACI Code now requires a minimum strain in the tensile reinforcement for flexural members, instead of calculating a limiting steel ratio, a maximum strain in the tensile reinforcement should also be adopted, rather than calculating a minimum steel ratio, which corresponds to a maximum strain in the tensile steel. By setting the minimum ACI steel ratio, Equation 1, equal to the steel ratio, Equation 2, the strain in the tensile steel, ε_t, becomes the maximum strain in the tensile steel, $\varepsilon_{t,max}$. Solving for $\varepsilon_{t,max}$, results in Equations 4 and 5. For f_c' less than or equal to 4444 psi (30 MPa), use Equation 4:

$$\varepsilon_{t,max} = \frac{0.85}{200}\beta_1 f_c' \varepsilon_u \tag{4}$$

For f_c' greater than 4444 psi (30 MPa), use Equation 5:

$$\varepsilon_{t,max} = \frac{0.85}{3}\beta_1 \sqrt{f_c'}\varepsilon_u - \varepsilon_u \tag{5}$$

where, f_c' is the concrete compressive strength in units of psi; β_1 is a function of the compressive strength of the concrete; and, ε_u is the ultimate strain in the concrete at the compression face, which is equal to 0.003, according to ACI 318-14.

Equations 4 and 5 determine the ACI maximum strain in the tensile steel reinforcement (see Figure 5). The ACI maximum strain in the tensile steel has three distinct segments resulting from the change in the value of β_1 as concrete compressive strength increases. The value for β_1 is a function of the compressive strength of the concrete. For f_c' less than or equal to ,000 psi (28 MPa), β_1 equals 0.85. For f_c' greater than or equal to 8000 psi (55 MPa), β_1 equals 0.65. For f_c' between and including 4000 psi (28 MPa) and 8000 psi (55 MPa), β_1 varies linearly. A simple relationship for the maximum strain in the tensile steel reinforcement may be conservatively determined using Equation 6:

$$\varepsilon_{t,max} = 0.00052\sqrt{f_c'} \tag{6}$$

This is the proposed maximum strain in the tensile steel and is also presented in Figure 5.

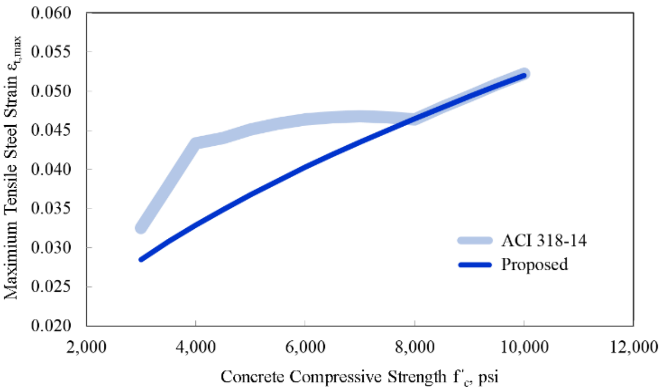

Figure 5. Maximum tensile steel strain versus concrete compressive strength.

Will future designers have to consider two different sets of strain limits based on the use of normal- or high-strength steel reinforcement for flexure? What about higher-strength rebar with Grade 120 (830) or more? Perhaps a simpler, more consistent method may be to modify the ACI relationship for resistance factor, ϕ, versus tensile steel strain, ε_t, and calculate a maximum tensile steel strain, $\varepsilon_{t,max}$.

Resistance Factor

Since 1963, the ACI 318 Code has defined the factored nominal moment strength as the product of the resistance factor and the nominal moment. In 2002, ACI 318 specified the resistance factor, ϕ, as a dependent function on tensile strain, ε_t, in steel reinforcement with a grade of 80 ksi (550 MPa) or less (ACI Committee 318, 2002). From the current ACI 318 Code, Figure 6 shows the graph of resistance factor versus tensile strain in steel reinforcement (ACI Committee 318, 2014).

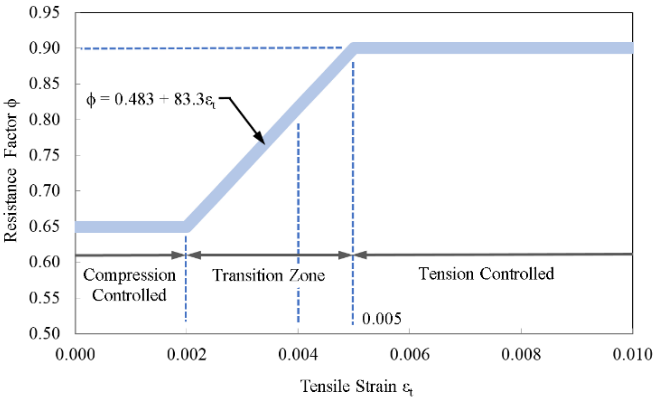

Figure 6. ACI resistance factor versus tensile steel strain.

Using the recommendations proposed by Mast et al. (2008) and Shahrooz et al. (2010) for high-strength steel reinforcement with grade 100 (690) rebar, and superimposing this on Figure 6, the resulting graph is shown in Figure 7. But Figure 7 is congested and unnecessarily complicated. One of the primary goals of using high-strength reinforcement, compared to nominal-strength reinforcement, is to reduce rebar congestion. Figure 7 may be significantly simplified to a single relationship by plotting resistance factor versus tensile steel strain, where the x-axis is also a function of the grade of the rebar, f_y, in units of ksi. Figure 8 is the resulting graph, calibrated for reinforcing steel for grades up to and including 120 ksi (830 MPa).

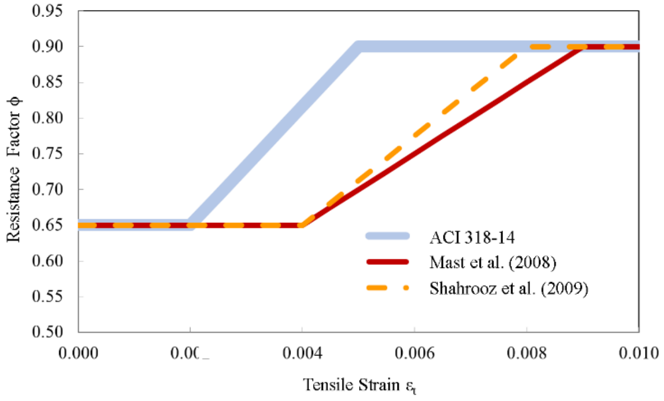

Figure 7. Resistance factor versus tensile steel strain for differing grades of rebar.

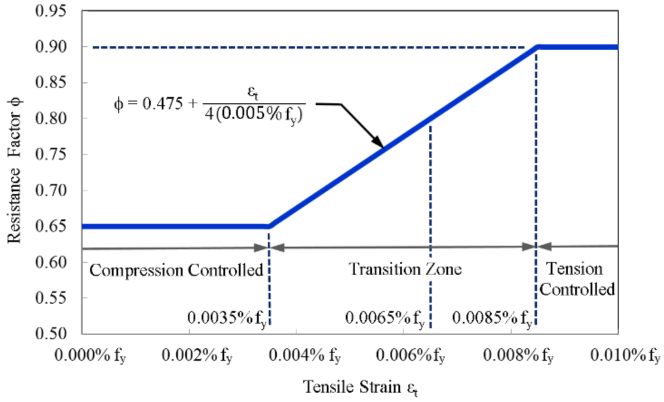

Figure 8. Proposed resistance factor versus tensile steel strain for up to grade 120 (830).

Table 1 presents the tensile strain limit results of Figure 8 for differing grades of steel reinforcement. For comparison purposes, the tensile strain limits in ACI 318-14 are also presented in Table 1. Using this proposed approach for grades of tensile steel reinforcement up to and including Grade 120 (830), and including the proposed maximum tensile strain, $\varepsilon_{t,max}$, from Equation 6, Figure 3 can be modified as shown in Figure 9.

Table 1. Tensile steel strain member limits.

ACI / Rebar Grade	Tensile Strain Limit		
	Compression Controlled	Transition Zone for Flexure	Tension Controlled
ACI 318-14	0.0020	0.0040	0.0050
Grade 60 (410)	0.0021	0.0039	0.0051
Grade 75 (520)	0.0026	0.0049	0.0064
Grade 100 (690)	0.0035	0.0065	0.0085
Grade 120 (830)	0.0042	0.0078	0.0102

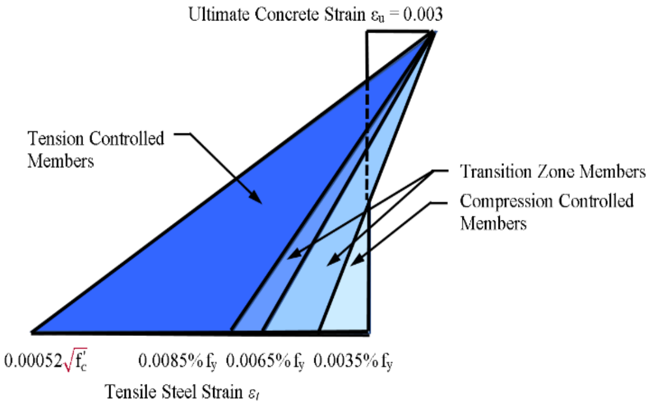

Figure 9. Proposed tensile strain limits for reinforced concrete members.

Comparative Numerical Design Example

Figure 10 shows how a singularly supported, reinforced concrete beam with a span length of 25 feet (8m) was designed for flexure. The beam was loaded with a uniformly distributed live load of 2.0 k/ft. (30 kN/m) and a uniformly distributed dead load of 1.2 k/ft. (18 kN/m), not including weight of the beam itself. Gross beam dimensions were held constant—the height of the beam was 26 in (0.65m); the beam width was 14 in (0.35m); and, the depth from the compression face to the neutral axis was 24 in (0.60m). The beam was designed using four grades of tensile steel reinforcement. For design, the grades of tensile steel reinforcement included 60 (410), 75 (520), 100 (690), and 120 (830). Factoring the loads, the ultimate moment was determined to be 398 k-ft. (540 kN/m). The compressive strength of the concrete was 6000 psi (40 MPa), and the modulus of elasticity of the steel reinforcement was 29,000 ksi (200 GPa). Table 2 presents the resulting properties of the beam with varying grades of tensile steel reinforcement.

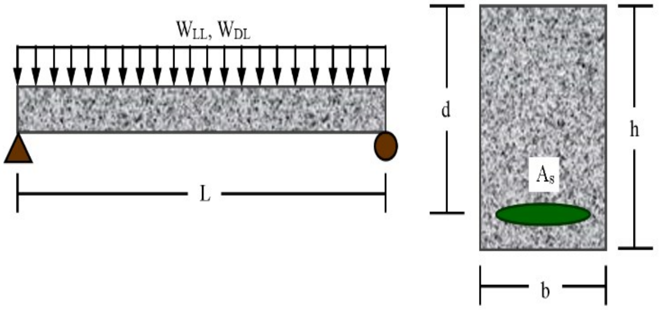

Figure 10. Design example of a flexural member with high-strength reinforcement.

Table 2: Beam design properties for differing grades of rebar reinforcement.

Beam Property	Grade of Tensile Steel Reinforcement, ksi (MPa)			
	60 (410)	75 (520)	100 (690)	120 (830)
ρ_{min}	0.0039	0.0031	0.0023	0.0019
ρ	0.0140	0.0107	0.0079	0.0066
ρ_{max}	0.0239	0.0191	0.0143	0.0120
ρ_b	0.0377	0.0274	0.0178	0.0134
A_s, in^2 (mm^2)	4.71 (3040)	3.61 (2330)	2.65 (1710)	2.21 (1430)
Tensile rebars	6 #8 (#25)	6 #7 (#22)	6 #6 (#19)	5 #6 (#19)
ε_t	0.0106	0.0112	0.0115	0.0115
$\varepsilon_{min,}$ $\phi = 0.90$	0.0051	0.0064	0.0085	0.0102
ϕM_n, k-ft. (kNm)	467 (630)	449 (610)	440 (600)	440 (600)

Based on ACI 318-14, the maximum tensile strain in the steel, per Equation 5, was 0.0464. Using the proposed equation, Equation 6, the maximum tensile strain in the steel was 0.0403. Compared to the beam with Grade 60 (410) steel reinforcement, a decrease of 43.7 percent in the required steel area was found for the beam with Grade 100 (690) rebar. In comparison to using Grade 120 (830) rebar, the decrease was 53.1 percent. Using rebar with high strength resulted in a beam design that was far less congested than using traditional normal-strength steel reinforcement.

Conclusions

In recent years, steel reinforcement has been developed with strengths greater than 80 ksi (550 MPa), which is the strength limit for reinforced concrete structures, according to ACI 318-14. In this paper, a proposed modification to the modification by Mast et al. was presented, where flexural members with tensile steel reinforcement of Grade 120 (830) were examined. A simple maximum tensile steel strain-limit relationship was also proposed, based on the minimum tensile steel ratio per ACI 318-14. Finally, a modification to the ACI Code for the resistance factor versus tensile steel strain relationship was proposed, which allows for rebar strength grades up to 120 ksi (830 MPa).

Results of a numerically reinforced concrete beam example designed with differing grades of rebar indicated that using higher-strength rebar, above the ACI limitation, resulted in less flexural steel congestion within the cross-section of the beam. According to this numerical example, when compared to using Grade 60 (410) rebar, reductions of 23%, 44%, and 53% in steel area were determined when using Grade 75 (520), 100 (690), and 120 (830) rebar, respectively. When compared to using Grade 75 (520) rebar, reductions of 27% and 39% in steel area was determined when using Grade 100 (690) and 120 (830) rebar, respectively. This is a significant reduction in flexural steel area, which can lead to improved concrete placement around the reinforcement in the field. Additional analysis and physical testing verification is needed to allow for the use of high-strength tensile steel reinforcement in flexural members of concrete structures. From an analytical design perspective, the use of high-strength reinforcement appears promising.

Acknowledgements

The authors would like to thank the Ritter Family of Bowling Green, Kentucky, for their generous gift to the civil engineering program at Western Kentucky University, which led to the Ritter Family endowment. This endowment made this research possible. The authors would also like to acknowledge the student workers at the Engineering Manufacturing Commercialization Center at Western Kentucky University who assisted with this project.

References

ACI Committee 318. (1963). *Building code requirements for reinforced concrete (ACI 318-63)*. Farmington Hills, MI: American Concrete Institute.

ACI Committee 318. (1971). *Building code requirements for reinforced concrete (ACI 318-71)*. Farmington Hills, MI: American Concrete Institute.

ACI Committee 318. (1995). *Building code requirements for reinforced concrete (ACI 318-95)*. Farmington Hills, MI: American Concrete Institute.

ACI Committee 318. (2002). *Building code requirements for reinforced concrete (ACI 318-02)*. Farmington Hills, MI: American Concrete Institute.

ACI Committee 318. (2014). *Building code requirements for reinforced concrete (ACI 318-14)*. Farmington Hills, MI: American Concrete Institute.

ASTM A1035/A1035M. (2016). *Standard specification for deformed and plain, low-carbon, chromium, steel bars for concrete reinforcement*. West Conshohocken, PA: ASTM.

CRSI. (2017, November). *Frequently asked questions (FAQ) about low-carbon, chromium ASTM A1035 Types CS, CM and CL steel reinforcing bar*. Concrete Reinforcing Steel Institute, Technical Note, ETN-M-11. http://resources.crsi.org/index.cfm/_api/render/file/?method=inline&fileID=119C15CA-A667-FBFE-FC13E2CE25B8DD93.

Faza, S., Kwok, J., & Salah, O. (2008). Application of high-strength and corrosion-resistant ASTM A1035 steel reinforcing bar in concrete high-rise construction. *Proceedings of the CTBUH 8th World Congress*. Chicago: Council on Tall Buildings and Urban Habitat.

IBC. (2018). *International building code*. Country Club Hills, IL: International Code Council.

Mast, R. F. (2007, January). *Memorandum: Simplified strength design of flexural members using MMFX steel*.

Mast, R. F., Dawood, M., Rizkalla, S. H., & Zia, P. (2008). Flexural strength design of concrete beams reinforced with high-strength steel bars. *ACI Structural Journal*, *105*(4), 570-577.

MMFX Technologies Corp. (2012, June). Mechanical properties MMFX$_2$ (ASTM A1035/A1035M). *Engineering Bulletin*, No. 1. Retrieved from https://www.mmfx.com/wp-content/uploads/2012/06/1-Mechanical_Properties8.pdf

MMFX Technologies Corp. (2015, June). ASTM A1035/A1035M specification. *Engineering Bulletin*, No. 7. Retrieved from http://www.mmfx.com/wp-content/uploads/2015/07/7-ASTM_A1035_Specification.pdf

Risser, B., & Humphreys, S. (2008, January 10). High-strength reinforcing steel: Next generation of niche? *Concrete Construction*. Retrieved from http://www.concreteconstruction.net/how-to/

materials/high-strength-reinforcing-steel-next-generation-or-niche_o

Shahrooz, B. M., Reis, J. M., Wells, E. L., Miller, R. A., Harries, K. A., & Russell, H. G. (2010), Flexural behavior and design with high-strength bars and those without well-defined yield point. *Proceedings of the Transportation Research Board 89th Annual Meeting*. Washington, DC: TRB.

Biographies

SHANE M. PALMQUIST is an associate professor of structural engineering in the School of Engineering and Applied Sciences at Western Kentucky University and is the Ritter Professor in civil engineering. Dr. Palmquist is the director of the Engineering Manufacturing and Commercialization Center at WKU, and is a licensed professional engineer in Kentucky. Prior to becoming a faculty member, Dr. Palmquist was a bridge engineer for Lichtenstein Consulting Engineers in Natick, Massachusetts. He earned his BS degree in civil engineering from the University of New Hampshire in 1995; MS in structural engineering from the University of Rhode Island in 1996; and PhD in structures/ materials engineering from Tufts University in 2003. His research interests include cable-supported structures and high-performance materials used in construction. Dr. Palmquist may be reached at Shane.Palmquist@wku.edu

ANDREW D. BELL is a senior completing his Bachelor of Science in Civil Engineering with a minor in mathematics from the School of Engineering and Applied Sciences at Western Kentucky University. Mr. Bell may be reached at Andrew.Bell051@topper.wku.edu

KATY A. BRIDGES is a senior completing her Bachelor of Science in Civil Engineering from the School of Engineering and Applied Sciences at Western Kentucky University. Ms. Bridges may be reached at Katy.Bridges799@topper.wku.edu

GLOBAL NAVIGATION SATELLITE SYSTEM SIGNAL MONITORING USING A HIGH-GAIN PARABOLIC DISH SYSTEM

Curtis Cohenour, Ohio University

Abstract

In this study, the author developed a high-gain dish antenna system for monitoring GPS and other global navigation satellite system (GNSS) signals. The system included a parabolic dish antenna, a rotator, and a graphical user interface (GUI). The dish was lightweight with low wind loading, and was installed without a substantial support structure. The GUI controlled operation of the antenna, including calibration and tracking. The GUI was customizable and implemented in MATLAB. A calibration routine eliminated the need for precise angular installation of the mechanical components. A five-parameter calibration model minimized elevation and azimuth errors in tracking the satellites. The calibration provided a transformation from the rotator reference frame to the true geodetic reference frame. The calibration was automatically performed by acquiring and tracking satellites. The dish swept each tracked satellite in azimuth and elevation to determine the exact satellite location in the rotator frame.

The satellite ephemeris identified the geodetic location of the satellite. Computation of calibration parameters were computed using least squares, which minimized the error between the transformed rotator coordinates and the true satellite position. The system was able to record radio frequency (RF) data or receiver data. RF data allowed the user to directly observe the GPS codes. The high gain and low noise provided receiver data with an extremely low carrier phase noise. In addition, multipath was near zero for the dish antenna. Receiver data could identify signal deformation, satellite antenna gain, and phase patterns. The results, presented here, include an analysis of the tracking error and the impact of the error on the measurements. The experimental results show that the antenna system was able to be quickly deployed and accurately aligned. Tracking errors of up to two degrees did not impact phase measurements, and GPS multipath errors were minimal.

Introduction

The global positioning system (GPS) is a space-based system used for land and air navigation. A lesser-known but important use of GPS is timing for banking transactions and cellular communications. The GPS signal is spread spectrum and 30 dB below the noise floor. The receiver operates by de-spreading the RF signal. Using a high-gain antenna increases the signal-to-noise ratio such that the spread spectrum "chips" can be observed. Investigating the details of the GPS signal requires low noise. The goal of this study was to develop a lightweight, semi-portable high-gain antenna. Because the antenna was semi-portable, alignment by surveying was impractical. The antenna chosen was an aluminum frame covered with galvanized steel mesh (see Figure 1), as it was lightweight and had low wind loading. The rotator was commercially available. The positioning system was implemented as a MATLAB graphical user interface (GUI) and specifically designed to facilitate alignment with the satellite spatial reference frame.

Figure 1. A high-gain parabolic dish system for tracking GNSS satellites.

The literature describes other high-gain systems for tracking global navigation satellite system (GNSS) satellite vehicles (SVs) (Wong, Phelts, Walter, & Enge, 2009; Gao, Chen, Lo, De Lorenzo, Walter, & Enge, 2008; Usman, Saleem, & Armitage, 2013; van Graas, Cohenour, Norris, Vinande, Gunawardena, & Carroll, 2015). In Wong et al. (2009), a 46m dish was used to collect RF data. The data characterize signal deformation of GPS and wide-area augmentation system (WAAS) satellites. A 1.8m dish (Gao et al., 2008) was used to investigate the interoperability of GPS and Compass-M1. A high-gain (13dBi) helical antenna was developed by Usman et al. (2013).

A solid 1.8m dish (van Graas et al., 2015) was used to investigate GPS signals. The rotator on the solid dish had a limited range in both azimuth and elevation. Mounting the dish on a trailer provided mobility. For example, positioning the dish under a forest canopy allowed the investigation of multipath through foliage, while a D-TA RF recorder collected data. In addition, van Grass et al. described experiments using the subject of this paper. The system used in this current study, and presented here, has the advantages of being lightweight with low wind loading, inexpensive, and high performance. The dish system consists of the dish and rotator, the RF system, and the software system.

Figure 1 shows the dish installed at the Ohio University Airport located in Albany, OH. An "H" stand anchored to the ground with stakes and ratchet straps supported the antenna. The Ohio University experimental local area augmentation system (LAAS) facility housed the equipment. The LAAS shelter contained the rotator control, RF components, data collection, and control. Operation was currently done onsite, but high-speed internet was available for remote operation in the future. A mobile system like this or the 1.8m dish in the study by van Grass et al. (2015) requires a means of calibration to align the antenna in earth-centered earth-fixed (ECEF) coordinates. Portable devices such as a level and a compass can align the antenna to within a few degrees but not to the precision required for satellite tracking. Coordinate transformation and a method of calibration using GPS satellites as truth is required to quickly align the antenna in ECEF coordinates. A GPS receiver was used to collect data for this study. The data from the GPS receiver consisted of code minus carrier (CMC) and carrier phase (CP) data. The data could define satellite antenna gain and group delay patterns.

Rotator System

The dish was part of an FPD1M9KIT mesh dish kit. The dish was 1.9m in diameter with a 6 mm mesh reflecting surface, produced and sold by RF-Hamdesign in the Netherlands. The rotator was a Big RAS/HR Alpha-Spid from Alpha Radio in Edmonton, Alberta, Canada. The controller was an MD-01 from Alpha, with a PS-01 power supply. The controller had front panel buttons for moving the rotator and programing. Communication of motion commands and rotator positions were accomplished by an RS-232 serial link. The dish was parabolic with an F/D ratio of 0.45. Figure 1 shows how three struts supported the feed horn. The Antcom G8 LHCP antenna was attached to a plate at the end of the support struts. The plate spacing was originally designed for a dB Systems cross-vee dipole. The Antcom antenna was mounted on standoffs to provide the proper spacing between the dish and the antenna phase centers.

The SPID BIG-RAS/HR rotator was able to rotate 720° in azimuth, and 180° in elevation. The current software used 360° degrees of azimuth and an elevation from 0° to 90°. This artificial azimuth restriction required the recording of some SV passes in two segments. Improved cable management would allow for an expanded range of azimuth motion, as passes recorded with this modification would be in one segment. Alignment and calibration are critical for accurate tracking of an SV. Alignment is the process of adjusting the rotator so that it is plumb and oriented in azimuth. Calibration is the process of tracking SVs and computing the necessary parameters to convert the measured azimuth and elevation of the rotator to ECEF coordinates. Alignment consists of two steps. First, zero azimuth is established by turning the rotator on the central support of the "H" stand. The rotator azimuth is then set using a compass and compensating for magnetic declination. In this case, the rotator zero was true geodetic north. An accuracy of ±10 is possible. Next, the rotator is leveled using a machinist level in the north-south and east-west planes. The accuracy of this method was ±2°.

RF System

Figure 2 shows the RF system. Also shown in Figure 1 is the Antcom Corporation Passive L1/L2 GPS (left-hand circularly polarized (LHCP) antenna P/N: G7L1L2-L-P-XS-1, which was used as a feed horn. This was a special order item with LHCP for use with a parabolic reflector. The Antcom G8 was a passive antenna, so a JCA Technology JCA12-4189T amplifier with a gain of 45dB was mounted at the feed horn. Twelve-volt power for the JCA amplifier was provided via the feed line using a bias-tee located in the equipment shelter. RF power was supplied to a GWInstek GSP-730 spectrum analyzer via a mini-circuits ZAPD-2 power splitter (S1). Another splitter (S2) was used to provide RF to two NovAtel receivers, the monitor, and the data collect. Each of these receivers was fitted with a direct current (DC) block to eliminate receiver antenna power from the RF circuit.

The monitor receiver was used for calibration and monitoring. The receiver was a PWRPAK-4E-L1L2W version GPSCARD "L1L2W" "SPR02340052" "Euro4-1.02-222" "2.140" "1.002" "2004/Jan/20" "11:00:47." The signal-to-noise ratio at the output of splitter S2 was much higher than it would be using a non-directional antenna. The carrier-to-noise ratio (CNR) of the receiver was limited to 52 dB-Hz. To overcome this issue, a variable RF attenuator was used to bring the CNR into the linear range of the NovAtel receiver. The receiver was programmed to output the American Standard Code for Information Interchange (ASCII) range log at 1Hz, "Log RangeA OnTime 1." The serial output was captured using the terminal program PuTTY and written to a text file. The output file was read into MATLAB, and the ASCII range message was used for calibration and monitoring.

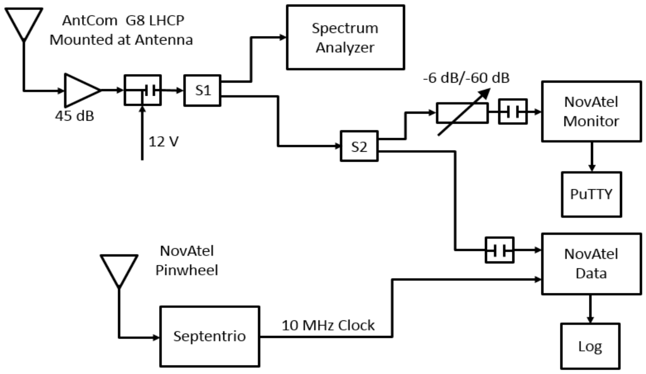

Figure 2. RF system.

The data receiver had a custom software modification to provide GPS L1 accumulated Doppler range (ADR) at 100 Hz. The receiver was a PWRPAK-4E-L1L2W100 version GPSCARD “L1L2W100” “TPR00480113” “Euro4-1.00-222” “2.140S3” “1.002” “2003/Dec/11” “15:37:06.” The binary log “Log Range OnTime .05” generated range data including pseudo range (PR) on L1 (PR1), PR on L2 (PR2), ADR on L1 (ADR1), and ADR on L2 (ADR2). The command “log GpsL1Adrb OnTime 0.01” generated the custom 100 Hz L1 ADR log. The output of the GpsL1Adrb log was processed using a NovAtel supplied utility *ProcessGPSL1ADR.exe*. This utility combined the GpsL1Adrb and the range logs into a custom 100Hz ADR1 measurement. The monitor and data receivers only tracked one valid satellite and could not generate a position and time solution. With no clock solution, the receiver operated in freewheeling clock mode with clock errors in the range of 100 ms. This was not an issue for the monitor receiver, but the large constantly varying clock error interfered with the results of the data receiver. To resolve this issue a Septentrio NV PolaRxS^{PRO} receiver version vAB0201.AB0204.AA0101.100 was used as a clock source. The Septentrio receiver was connected to a NovAtel GPS-600 pinwheel antenna and generated a valid position and time solution. The Septentrio had a 10 MHz clock output and was connected to the clock input of the NovAtel data receiver. The commands “ExternalClock Rubidium 10 MHz” and “ClockAdjust Disable” set up the NovAtel clock input and disabled the clock adjust. The resulting NovAtel clock was then fixed with a constant error in the range of 100 ms. Some slowly varying clock error from the Septentrio time solution remained in the clock signal but was later removed in data processing. This error was on the order of three meters or 10 ns.

Software System

The functionality of the software system used for monitoring the GPS signal, control of the dish, calibration, tracking, and other operations were tied to the dish controller and the monitor receiver. The data from the data receiver will be discussed later. The software system could be operated in real time, while connected to the rotator or in simulated mode. Simulated mode was used to test the software and could be operated faster than real time. The dish control was implemented in a MATLAB GUI composed of several interactive windows. Figure 3 (left) shows the main control window. This window includes buttons on the left for the primary functions of the control software with status lights on the right. The functions include starting and stopping the GUI, Sweep, Calibrate, Track, Scan, Scan and Sweep, Setup, and Stop. There is also a button for antenna pattern, but this function was not been implemented.

There were functions included for: Start GUI; Stop GUI; start control; and, stop control. A red/green indicator to the right of the Start GUI button indicated that the GUI was running. The Stop GUI button also stopped the motion of the rotator. The Sweep function swept the antenna ±6° in azimuth and ±6° in elevation. The Calibrate button ran the calibration routine with the intent of generating the parameters necessary to convert the raw azimuth and elevation from the rotator to true azimuth and elevation. The Track button started the tracking of an SV. The Scan button scanned the constellation, stopping for 10 seconds at each SV. The Scan and Sweep function scanned the constellation, but performed a sweep for each SV. This function was used to collect calibration data. The Setup button provided a means to set a variety of adjustable parameters. The Stop button stopped the motion of the rotator.

Figure 3 (right) shows an interactive Sky Plot GUI. The user may click on any location greater than the adjustable 5° elevation mask angle to move the rotator. The antenna location is shown as the red oval near SV pseudo random noise (PRN) 16. The antenna locator was a 6° circle in free space and appears as an oval in Figure 3 (right), because the hemispherical sky distorts the planar projection. Clicking on an open area of the sky plot will cause the antenna to move to the selected position and clear the tracked SV. Clicking on or near an SV, indicated by a black dot and a number, will set the tracker to the SV and move the antenna to the desired SV. The direction and speed of each SV was indicated by a red arrow. Red dotted lines indicated the elevation mask and the location of the rotator zero azimuth. In the current version of the software, the rotator cannot cross the rotator zero azimuth. The rotator zero azimuth was indicated by the red dotted radial line at -10.9°.

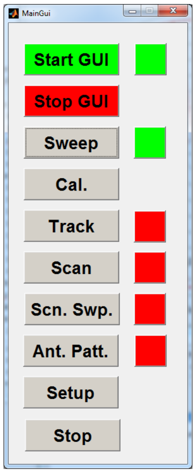

(a) Main GUI control window.

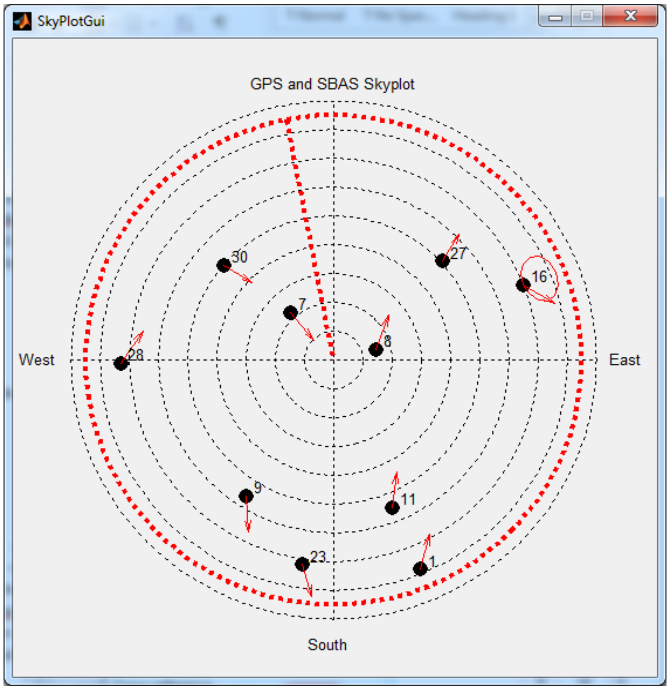

(b) GUI sky plot.

Figure 3. GUI windows.

The satellite positions and velocities are determined using the two-line elements (TLEs). The TLEs can be downloaded from http://www.celestrak.com/NORAD/elements under Navigation Satellites/GPS Operational (CelesTrak, 2016). The GPS second of the week (SOW) is derived from the system time with the coordinated universal time offset. The function was called with the GPS SOW and returned the location and velocity of all the SVs above the mask in earth-centered earth-fixed coordinates. The position was converted to azimuth and elevation based on the user location (supplied by the user). The future position was computed adding 1000s to the SOW and calling the TLE function a second time. The future position was converted to azimuth and elevation. The SV positions were plotted and labeled. A red arrow was drawn from the SV position and its future positon to indicate the direction and velocity of the SV in azimuth and elevation.

Figure 4 shows how the azimuth/elevation/CNR GUI display was tied to the monitor receiver. There are plots of the azimuth vs. CNR and elevation vs. CNR. The L1 and L2 CNR and the tracked SV PRN are shown on the right. The button Set Az0 and the value of Az0 are located between the azimuth and elevation plots. The azimuth and elevation plots show the results of the sweep function. The read circle indicates the current measurement. The horizontal axis is the calibrated rotator azimuth less the SV azimuth. When the rotator sweeps, the CNR drops approximately with the square of the angular error between the antenna and the SV. Clicking on the azimuth graph stops all other rotator functions and moves the antenna to the indicated azimuth. For example, in Figure 4, clicking at +8° on the azimuth plot would move the antenna to +8°. If the SV were at 60°, then the rotator would move to a true azimuth of 68°. In this case, the Az0 is 349.1°, so the rotator azimuth would go to 78.9° because there is a difference of 10.9 degrees between the rotator zero and true north.

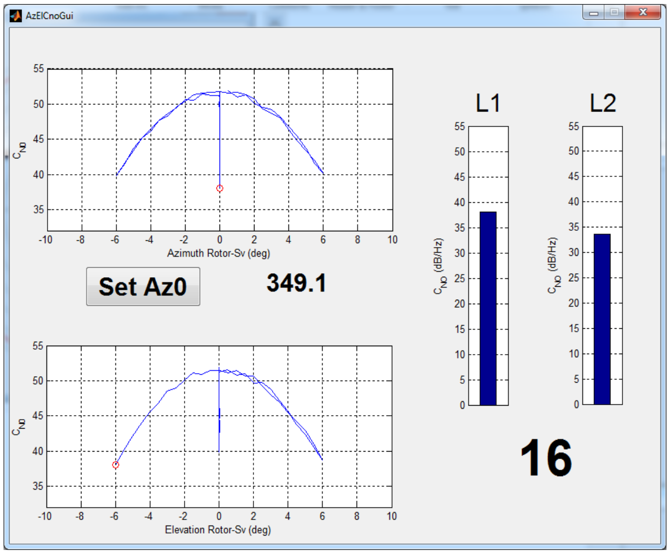

Figure 4. The interactive azimuth/elevation/CNR (AzElCNR) GUI window.

In addition to monitoring the azimuth/elevation/CNR, the GUI was used to set the rotator Az0. As noted above, if the rotator is carefully leveled, the only unresolved error will be Az0. The SV CNR peak was found by adjusting the azimuth and elevation using the Azimuth /Elevation/CNR GUI (see again Figure 4). Once the peak was found, clicking the Set Az0 button sets Az0. With the Az0 set, the Scan and Track function could be used to collect calibration data. Additional GUIs (not shown) include manual control, setup, and debug information.

Calibration

Calibration defines the transformation from the rotator azimuth and elevation to true azimuth and elevation. The SVs were in the true coordinate system, while the rotator coordinate system was unknown. The calibration was performed by leveling the rotator and measuring the Az0 of the rotator. The rotator zero could be set to true north or any other convenient position. A rough calibration was performed by finding an SV and clicking the Set Az0 button, as described above. The system was then placed in Scan and Sweep mode. This tracks the SVs one at a time and sweeps both azimuth and elevation. Data were automatically collected. Once all of the SVs had been scanned, the calibration was performed by pressing the Calibrate button (see again Figure 3). Since some of the SV sweeps may not have been centered, it was best to consider this a preliminary calibration. Once the preliminary calibration was completed, the GUI was restarted to clear the data collection. The scan and sweep could be run again for several passes and the calibration repeated. This time, the sweeps would generally be centered and provide accurate SV locations for the calibration. With practice, the total setup and calibration time is about two hours.

Figure 5 shows the azimuth and elevation for the calibration performed May 31, 2013. The blue lines indicate the rotator sweeps, while the red circles indicate the true SV position. The objective was to find model parameters that created the best fit.

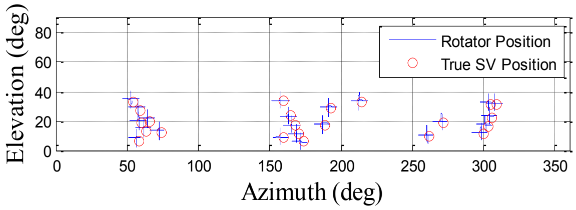

Figure 5. Azimuth and elevation for calibration data collected on May 31, 2016 with multiple sweeps for each SV, and the true SV location. The antenna travel between sweeps is not plotted.

Figure 6 (left) shows how, for each SV observation, the first step was to determine the location of the peak in the CNR curve. The blue dots show the elevation data collected. The red curve is a parabola fitted to the data. The peak was found for the rotator data and indicated by the large blue dot. The true SV position is plotted as a red dot. The data are plotted as the SV elevation less the rotator elevation. This compensates for the moving SV.

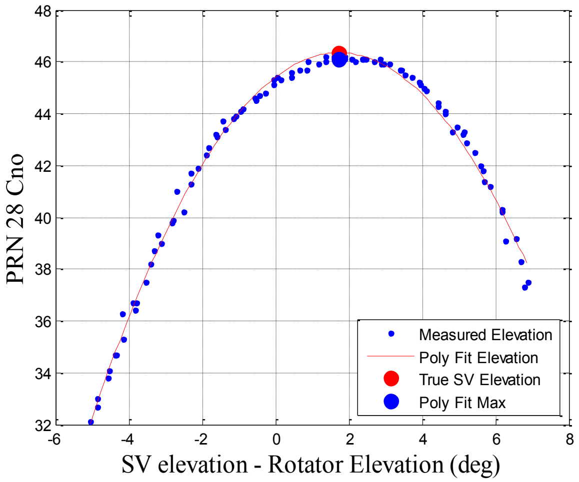

(a) Peak CNR versus elevation curve.

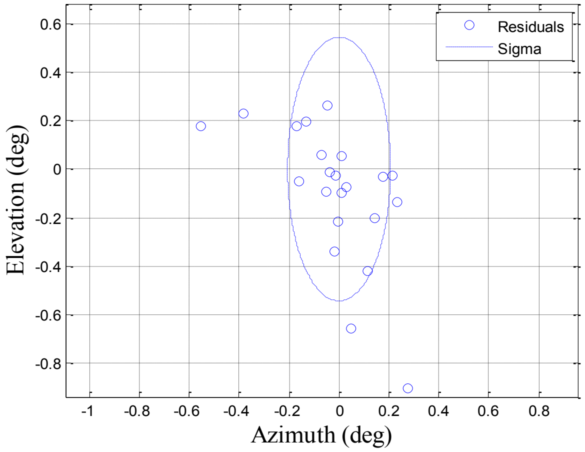

(b) Peak CNR versus residual errors.

Figure 6. Identifying the peak in the CNR versus elevation curve and residual errors.

The process was repeated for each observation, which included both elevation and azimuth. The results, in this example, were a set of 23 azimuth/elevation pairs in the rotator frame. In addition, there were 23 true azimuth/elevation pairs from the TLEs. Ordinary least squares (OLS) (Golub & van Loan, 1996) was used to find the best model parameters that fit the rotator data to the true SV position data. Figure 6 (right) shows the results for the five parameter models: the circles show the errors for each observation;

one outlier is not shown. The dotted oval is the standard deviation of the residuals including the outlier. The azimuth standard deviation was 0.2º, while the elevation standard deviation was 0.5º. The five-parameter model was mathematically correct and used direction cosine matrices to rotate the dish line of sight (LOS) to the true reference system. The antenna LOS may be offset from the moving end of the rotator. The rotator rotation was known. The alignment of the fixed end of the rotator in the true coordinate system was unknown. In the five-parameter model, these values were computed and used to correctly point the antenna.

Table 1 lists the reference frames used in the five-parameter model. The antenna LOS was $V^A = [1\ 0\ 0]^T$, where the superscript "T" indicates the transpose. V^A is in the antenna reference frame, the A-frame. There was likely some misalignment between the A-frame and the moving end of the rotator, which was defined as the B-frame. The rotator had azimuth and elevation angles that defined the relationship of the moving end of the rotator with respect to the stationary end of the rotator. The B-frame was the moving end of the rotator and the R-frame was the stationary end of the rotator. The satellites were by definition in the navigation frame. There will be misalignment between the stationary end of the rotator (R-frame) and the navigation frame or N-frame. Table 1 provides a summary of the reference frames. Converting the antenna LOS from the A-frame to the N-frame required a series of coordinate frame rotations. The rotation matrix was defined in the navigation literature (Titterton & Weston, 2004) for the conversion from the aircraft body to the navigation coordinate system. This is given by Equation 1:

Table 1. Reference frames for the five-parameter calibration.

Reference System	Symbol
Antenna	A
Rotator Body (Moving End)	B
Rotator (Stationary End)	R
Navigation	N

$$C_N^B = f_R(\Theta) \qquad (1)$$

where, Θ is a column vector of the three rotational angles—roll, pitch, and yaw;

$$f_R(\Theta) = \begin{bmatrix} \phi \\ \theta \\ \psi \end{bmatrix} = \begin{bmatrix} roll \\ pitch \\ \psi\ yaw \end{bmatrix}$$

is defined in Titterton & Weston (2004); and, C_N^B is a 3×3 transformation matrix.

Table 2 summarizes the rotational parameters. The antenna LOS is a unit vector in the X^A direction. The rotation wrt to the moving end of the rotator is given by Θ^B. The two components of Θ^B are calibrated parameters. The rotation of LOS vector in the B-frame to the R-frame is given by Θ^R . Θ^R contains the elevation and azimuth angles of the rotator. The misalignment of the rotator with respect to the navigation frame is contained in Θ^N. Examination of the source column in Table 2 shows five calibrated parameters: θ^B, ψ^B, ϕ^N, θ^N, ψ^N. The azimuth and elevation of the rotator, parameters θ^R, ψ^R, are known.

Table 2. Rotational parameters for the five-parameter calibration model.

Rotation	Source	Symbol	Description
$\Theta^B = \begin{bmatrix} 0 \\ \theta^B \\ \psi^B \end{bmatrix}$	Calibration	θ^B	Elevation of Antenna LOS with the moving end of the rotator
	Calibration	ψ^B	Azimuth (Left / Right) with the moving end of the rotator
$\Theta^R = \begin{bmatrix} 0 \\ \theta^R \\ \psi^R \end{bmatrix}$	Rotator	θ^R	Rotator Elevation
	Rotator	ψ^R	Rotator Azimuth
$\Theta^N = \begin{bmatrix} \phi^N \\ \theta^N \\ \psi^N \end{bmatrix}$	Calibration	ϕ^N	Roll of the fixed end of the rotator with the True Reference Frame
	Calibration	θ^N	Roll of the fixed end of the rotator with the True Reference Frame
	Calibration	ψ^N	Roll of the fixed end of the rotator with the True Reference Frame

Equation 2 converts the antenna LOS vector in the A-frame to a vector in the N-frame, as defined in Table 1 using the parameters from Table 2.

$$V^N = C_R^N C_B^R C_A^B V^A \tag{2}$$

where,

$$V^A = \begin{bmatrix} 1 \\ 0 \\ 0 \end{bmatrix}$$

$$C_A^B = f_R \begin{pmatrix} 0 \\ \theta^B \\ \psi^B \end{pmatrix}$$

$$C_B^R = f_R \begin{pmatrix} 0 \\ \theta^R \\ \psi^R \end{pmatrix}$$

$$C_R^N = f_R \begin{pmatrix} \phi^N \\ \theta^N \\ \psi^N \end{pmatrix}$$

Data Processing

In this paper, the authors present three primary goals for data processing: to examine the multipath errors, to measure the phase noise, and to investigate how dish misalignment impacts the measurements. Range data were collected at 20 Hz, and ADR1 data were collected at 100 Hz. An external clock was used to limit clock errors in the data collection receiver. Data processing for all files proceeded as follows: first, the binary range data were parsed, extracting 20 Hz for the PR1, PR2, ADR1, ADR2, PRN, and GPS SOW. Next, data from the 100 Hz GpsL1Adr log were extracted and consisted of ADR1, SOW, and PRN. The data were trimmed to remove transients during acquisition and loss of signal. There were two time bases involved, 20 Hz and 100 Hz, and two ADR1 measurements.

Figure 7 (right) shows the ionosphere delay free (IF) CMC (Kaplan, 1996) was computed for the 20 Hz data. The SV passed through 0° rotator azimuth, requiring the rotator to reposition. Figure 7 (right) also shows a small gap of 5.2 minutes in the data at hour 21.7. The carrier phase ambiguity changed when the SV was reacquired. The change in carrier phase ambiguity was removed from the data in Figure 7. Figure 7 (left) shows that there was an approximate 0.6m dip in the CMC due to tropospheric delay, which varied with SV elevation.

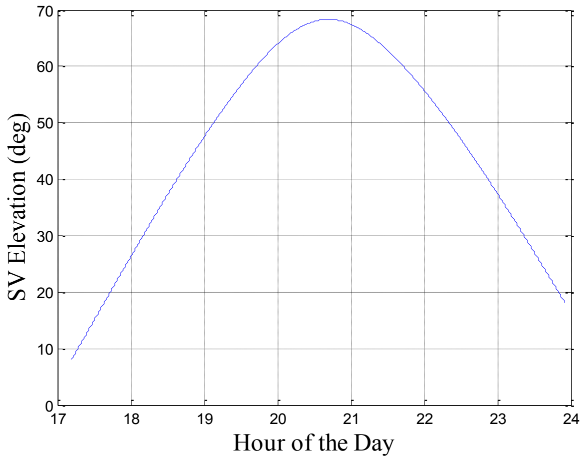

(a) SV elevation.

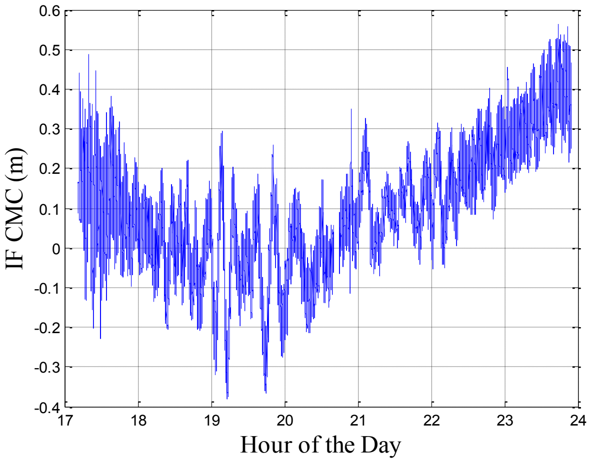

(b) 20Hz IF CMC for SV17.

Figure 7. SV elevation and 20Hz IF CMC for SV17, using data collected on June 24, 2016.

Figure 8 plots range data for SV17 on June 24, 2016. Note that there was a large offset between the two curves. This was due to the large clock offset in the data receiver. The range offset was 2,925,000m or 9.8 ms. The data receiver had a stabilized clock input, but there was no mechanism for the receiver to compute a time solution. Figure 9 shows how this was corrected by removing a 10th-order polynomial from the data. The true location of the SV was extracted from the National Geospatial-Intelligence Agency (NGA) Antenna Phase Center files in SP3 format (Hilla, 2010; National Geospatial, FTP, 2016). The SP3 data contained the satellite position and the satellite clock at 15-minute intervals. The clock values were synchronized with GPS time. Overall accuracy of the NGA orbit data was given with respect to International GNSS Service (IGS) orbit data and was 7.1 cm 3D RMS for orbit data ((National Geospatial, GPS, 2016). The true SV position and clock were interpolated onto the time scales using the MATLAB interp1 function and the “spline” option. The true range was computed by subtracting the origin in ECEF from the true SV position and taking the norm. The true range was offset by the SP3 clock adjust such that it matched the pseudorange.

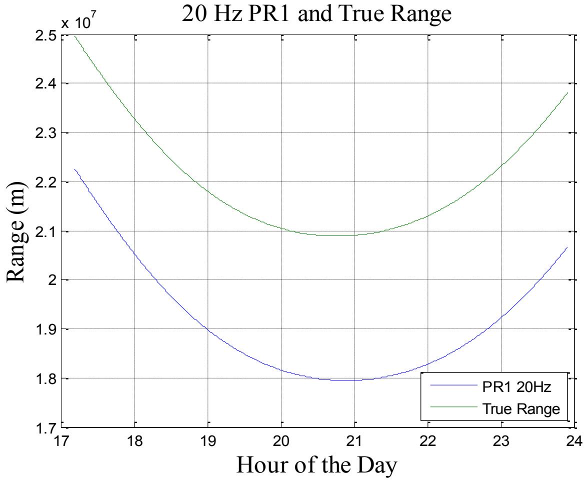

Figure 8. True range and PR1 data for SV17 on June 24, 2016.

Removing a 10th-order polynomial from the 100 Hz ADR1 yielded a corrected ADR1 (ADR1C). Figure 9 (right) shows a plot of the 100 Hz ADR1C data. The remaining errors were attributable to the clock solution error in the Septentrio receiver. The phase noise was calculated using Equation 3 by taking the time difference of the 100 Hz ADR1C from Figure 9 (right).

$$\Delta ADR1C = ADR1C_{t_{k+1}} - ADR1C_{t_k} \qquad (3)$$

where, t_{k+1} and t_k are consecutive samples of ADR1C.

Figure 10 (left) shows the results, with the probability density function (PDF) shown in Figure 10 (right). One final question remained: did the dish pointing accuracy impact the results? Pointing errors are caused by calibration errors, positioning errors, and TLE errors. To answer this question, a dither signal was introduced to purposely offset the antenna, and the results examined. Using the five-parameter model, the standard deviation of the residuals was 0.162° for azimuth and 0.176° for elevation. Azimuth and elevation errors of 0.5° could be expected. The positioning dead band was 0.1°, based on data collected while tracking an SV. The TLE errors were similar to almanac errors (Kelso, 2007) and on the order of 10 km. The range to the SV was 20 to 25 million meters; dividing by 10 km and using the small angle approximation for the sine, the error was 0.03°. The time was verified using the debug display and accurate to within one second. The SV moved about 4000 m/sec, which resulted in a time sync error of 0.01°. Thus, the TLE error was essentially zero, compared to the other errors. The total tracking error was less than 1º.

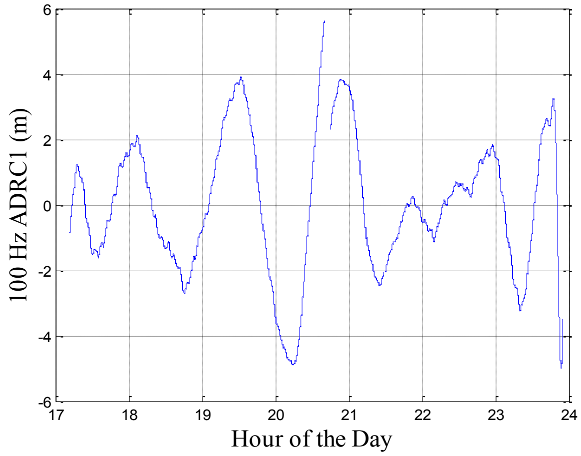

(a) 100Hz ADR1C with a four-pole Butterworth high-pass filter.

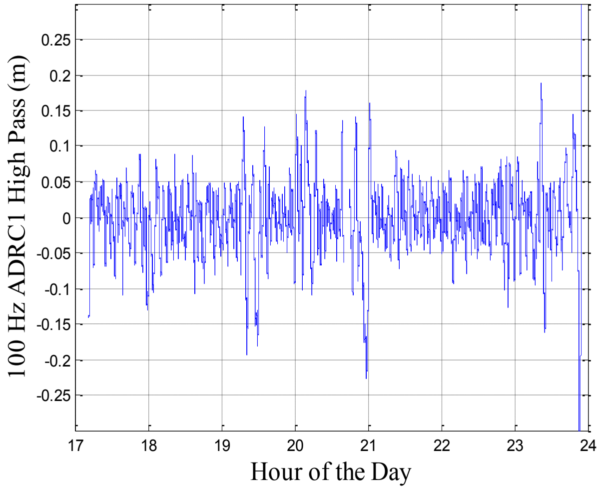

(b) After removal of polynomial curve fit for SV17.

Figure 9. Data from June 24, 2016.

To determine the impact of antenna misalignment, a temporary modification was made to the rotator GUI to insert dither into the dish pointing system. As the SV was tracked, a dither signal of ±2° max was placed on the azimuth and elevation of the dish, as shown in Figure 11. Here, the dither signal was scaled for presentation. Each step of the dither signal was 5s long. The dither was keyed to GPS time to facilitate time registration with the data during processing.

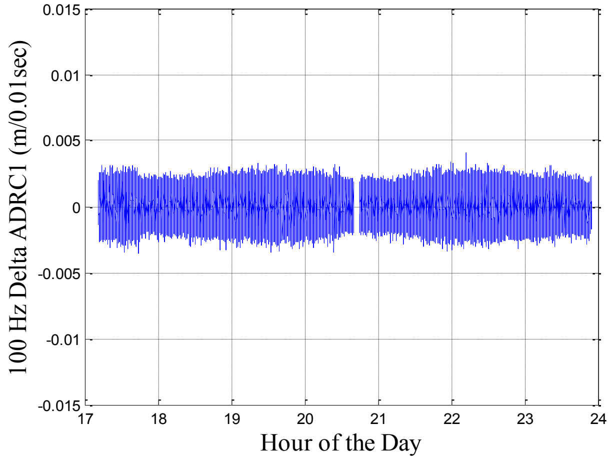

(a) Delta ADR1C phase noise.

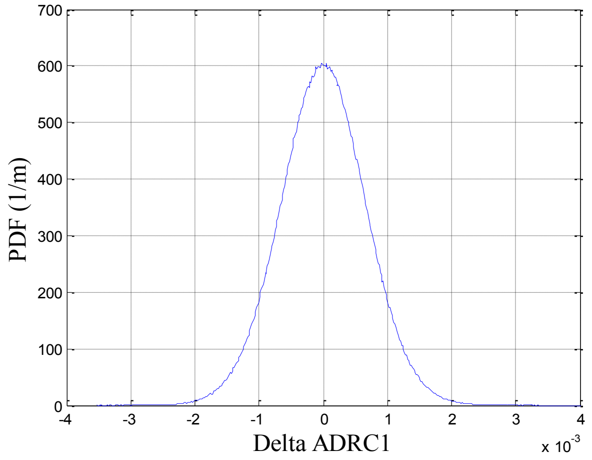

(b) PDF for SV17.

Figure 10. Data from June 24, 2016.

OLS (Gao et al., 2008) was used to fit the dither to the data using Equation 4:

$$\tilde{\varnothing}_1^c = \varnothing_1^c - \alpha_1 D_{Az} - \alpha_2 D_{El} \qquad (4)$$

where, $\varnothing_1^c$ is the 100 Hz corrected ADR, ADR1C; D_{Az} is the azimuth dither degrees; D_{El} is the elevation dither in degrees; α_1 and α_2 are unknowns in the OLS solution and have units of m/deg; and, $\tilde{\varnothing}_1^c$ is the modeled $\varnothing_1^c$ with dither impacts removed. The values of α_1 and α_2 are found by minimizing $\tilde{\varnothing}_1^c$. That is, $\tilde{\varnothing}_1^c = 0$. Table 3 gives the results of the misalignment (or dither) test. With α_1 and α_2 set to zero, the $\tilde{\varnothing}_1^c$ was the same as ADR1C, and the standard deviation was 0.027 526 189m. With α_1 and α_2 set to the values in Table 3, minimizing the dither corrected ADR1C, $\tilde{\varnothing}_1^c$; the standard deviation was 0.027 516 169m. The difference was 0.020µm. The conclusion is that dish misalignment of ±2° has no impact on ADR1C.

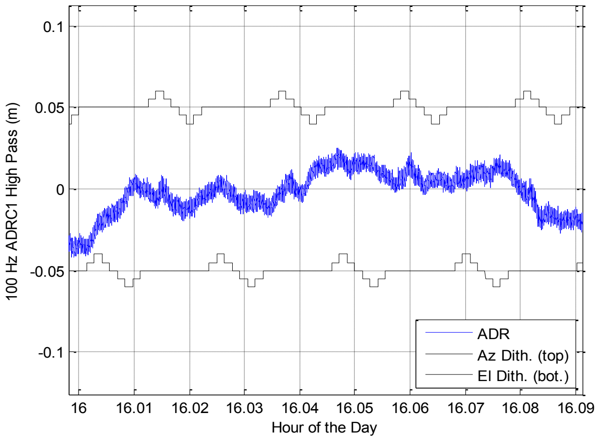

Figure 11. Data collected to determine the impact of antenna misalignment. Dither signals are ±2° maximum. The dither was keyed to GPS SOW to eliminate issues in time registration of the dither and the data. The magnitude of the dither signal is not to scale.

Table 3. OLS solution results for the misalignment (dither) test.

Case	Az. Multiplier m/deg α_1	El. Multiplier m/deg α_2	Standard Deviation
No Comp.	0	0	0.027 526 189
OLS values	0.000 641	0.000 400	0.027 516 169

Conclusions

The performance of the lightweight dish and associated RF and control components were evaluated. Performance in multipath, phase noise, pointing accuracy, and calibration were investigated. Multipath performance for the system was ±30 cm for IF CMC and ±20 cm for L1 ADR. Phase noise was ±3 mm for L1 at 100 Hz. An improved calibration model was developed and tested. The model accurately accounted for errors in the antenna LOS with respect to the rotator and alignment of the rotator in the navigation coordinates. Results of the calibration were an azimuth residual standard deviation 0.2º, while the elevation residual standard deviation was 0.5º. The pointing accuracy of the dish was ±1°. An evaluation of the dish performance showed that there was no L1 ADR error for dish pointing errors of up to ±2°.

Data for several SVs were collected. All of the SVs were Block Type IIR or IIR-M running on rubidium clocks. The phase noise was ±0.4 cm for all SVs except PRNS 28 and 21. PRN 28 was ±0.6 cm. PRN 21 was known to have phase noise spikes. The underlying phase noise was ±0.4cm, while the spikes were ±1.5 cm. The research presented here was completed in August, 2015. Since that time, the system has been used to study phase anomalies in the GPS Satellite Vehicle Number 63, which broadcast as pseudo random noise code 1 (see Ramesh, Ugazio, & van Graas, 2007). The solid dish (see van Graas et al., 2015) using the same software with an alternate rotator will be used for pulsar measurements. Finally, the software is being applied to an alternate antenna system to perform low-frequency WWVB measurements on CubeSats (n.d.). The system presented here is easily deployable and can be used with an RF data recorder or a GPS receiver. Because a mobile or semi-mobile system is difficult to mechanically align in ECEF coordinates, a calibration means is provided. The calibration method is quick and accurate. The system provides low-noise GPS data for analysis of signal deformation, satellite antenna gain and phase measurement, and multipath investigations.

References

CelesTrak. (2018). Retrieved from http://www.celestrak.com/NORAD/elements/

CubeSat. (n.d.). *Origin of the new space revolution*. Retrieved from http://www.cubesat.org/

Gao, G., Chen, A., Lo, S., De Lorenzo, D., Walter, T., & Enge, P. (2008). Compass-M1 broadcast codes and their application to acquisition and tracking. *Proceedings of Institute of Navigation National Technical Meeting*. Manassas, VA: Institute of Navigation.

Golub, G., & van Loan, C. (1996). *Matrix computations*. (3rd ed.). Baltimore: The John Hopkins University.

Hilla, S. (2010). *The extended standard product 3 orbit format (SP3-c)*. Silver Springs, MD: National Geodetic Survey.

Kaplan, E. D. (1996). *Understanding GPS: Principles and applications*. Boston: Artech House Publishers.

Kelso, T. S. (2007). Validation of SGP4 and IS-GPS-200D against GPS precision ephemeris. *Proceedings of the 17th AAS/AIAA Space Flight Mechanics Conference*. Springfield, VA: AAS.

National Geospatial Intelligence Agency. (2016). *NGA/IGS GPS orbit (ephemeris) comparison page*. Retrieved from http://earth-info.nga.mil/GandG/sathtml/ngaigscompare.html

National Geospatial Intelligence Agency. (2016). *NGA FTP directory*. Retrieved from ftp://ftp.nga.mil/pub2/gps/apcpe/2016apc/

Navigation Center. (n.d.). *GPS constellation status for 08/02/2016*. Retrieved from http://www.navcen.uscg.gov/?Do=constellationstatus

Ramesh, R., Ugazio, S., & van Graas, F. (2017). Characterization of GPS satellite phase anomalies for SVN 63 (PRN 1) using a dish antenna. *Proceedings of the ION 2017 Pacific PNT Meeting*. Manassas, VA: Institute of Navigation.

Titterton, D. H., & Weston, J. L. (2004). *Strapdown inertial navigation technology*. (2nd ed.) Reston, VA: The American Institute of Aeronautics and Astronautics.

Usman, M., Saleem T., & Armitage, A. D. (2013). Design, assembly and testing of a high gain LHCP helical antenna for reception of reflected GPS signals. *Progress In Electromagnetics Research, 44*, 161-174.

van Graas, F., Cohenour, C., Norris, N., Vinande, E., Gunawardena, S., & Carroll, M. (2015). GNSS signal characterization and monitoring using high gain antennas. *Proceedings of the 28th International Technical Meeting of The Satellite Division of the Institute of Navigation*. Manassas, VA: Institute of Navigation.

Wong, G., Phelts, E., Walter, T., & Enge, P. (2009). Characterization of signal deformations for GPS and WAAS satellites. *Proceedings of the 22nd International Technical Meeting of the Satellite Division of the Institute of Navigation*. Manassas, VA: Institute of Navigation.

Biography

CURTIS COHENOUR is an assistant professor in the Engineering Technology and Management Department at Ohio University. He received his BS degree from West Virginia Institute of Technology in 1980, and MS and PhD degrees from Ohio University in 1988 and 2009, respectively. He is a registered professional engineer in West Virginia and Ohio and has worked as an electrical engineer in the areas of control systems, automation, and power and joined Ohio University in 2002 as a research engineer working for the Ohio University Avionics Engineering Center. He has worked on projects covering a wide variety of avionics and navigation systems, such as the instrument landing system, microwave landing system, distance measuring equipment, LAAS, WAAS, and GPS. His recent work has included research with the Air Force Research Laboratory in Dayton, Ohio, aimed at understanding and correcting image geo-registration errors from a number of airborne platforms. Dr. Cohenour may be reached at cohenour@ohio.edu

DESIGN AND CYCLIC ELASTOPLASTIC ANALYSIS OF GRADED THIN-WALLED STEEL TUBULAR COLUMNS WITH ENHANCED STRENGTH AND DUCTILITY

Qusay Al-Kaseasbeh, University of North Dakota; Iraj H.P. Mamaghani, University of North Dakota

Abstract

Thin-walled steel-stiffened box columns are widely used as cantilever bridge piers, due to their structural efficiency, attractive appearance, high earthquake resistance, and potential for concrete infilling. However, local buckling, global buckling, or a combination of both is usually the main reason for significant strength reduction in these columns, which eventually leads to their collapse. In this study, the authors investigated the behavior of thin-walled steel-stiffened box columns with uniform (B) and graded thicknesses (GB) under constant axial and cyclic lateral loading. A GB column with size and volume of material equivalent to the uniform B column was analyzed under constant axial and cyclic lateral loading.

The analysis was carried out using a finite element model (FEM), which considers both material and geometric nonlinearities. The accuracy of the employed FEM was validated based on experimental results available in the literature. The GB column showed superior strength and ductility performance (i.e., an improvement of 24% in the ultimate strength was achieved using the GB column, as compared to its counterpart B column). Buckling behavior of the B column was captured relatively well by the FEM employed. Local buckling behavior was delayed and less severe in the case of the GB column, as compared to its counterpart B column. Moreover, the dissipated energy of the GB column was higher and exhibited higher ductility than that of the B column. Finally, the cyclic behavior of the B column was greatly improved with the longitudinal stiffeners.

Introduction

In severe seismic regions, civil engineering structures are exposed to increased earthquake risk. Their integrity is always threatened by extreme uncertainties of severe earthquakes (Miller, 1998; Mahin, 1998; Nakashima, Inoue, & Tada,1998; Al-Kaseasbeh, Lin, Wang, Azarmi, & Qi, 2018; Al-Kaseasbeh, 2015). Thin-walled steel-stiffened box columns are widely used in modern buildings, offshore platforms, elevated storage tanks, transmission towers, and in wind turbines. Additionally, they can be used as cantilever bridge piers in seismic regions, due to their structural efficiency, aesthetic attractive appearance, high earthquake resistance, and potential for concrete infilling (Ucak & Tsopelas, 2014). Compared to their counterparts of reinforced concrete, thin-walled steel-stiffened box columns are more efficient, due to their light weight, high strength, ductility, and ease and speed of construction, especially when limited construction space is available (Yang, Zhao, Sun, & Zhao, 2017; Mamaghani, 1996). Thin-walled steel-stiffened box columns are susceptible to a significant loss of strength and ductility under severe earthquakes (e.g., the 1995 Kobe earthquake, the 2008 Sichuan earthquake, and the 2011 East Japan earthquake) (Ucak & Tsopelas, 2014). Thin-walled steel-stiffened box columns experience excessive local buckling and then collapse, due to severe earthquakes (Bruneau, 1998). As a result, conventional uniform thin-walled steel-stiffened box columns have been extensively investigated in the past few decades.

Many experimental and numerical analyses have been conducted to improve the strength and ductile behavior of the thin-walled steel-stiffened box columns under axial and cyclic lateral loading (Yang et al., 2017; Ucak & Tsopelas, 2014). A numerical study was also conducted to investigate factors that affect strength and ductility capacities of unstiffened box sections (Usami & Ge, 1998). The ultimate strength of thin-walled steel-stiffened box columns depends on the width-to-thickness ratio parameter, R_f, and the slenderness ratio parameter, λ, (Kwon, Kim, & Hancock, 2007). In general, local buckling is affected by R_f of the column, while λ controls the global buckling of the column (Bruneau, 1998; Fukumoto, 2004; Usami, & Ge, 1998). Experimental and analytical investigations on the effectiveness of retrofitting the stiffened box cross sections were carried out by a number of researchers (Kwon, Kim, & Hancock, 2007; Goto, Wang, & Obata, 1998; Mamaghani, 2008). The study concluded that all retrofit schemes, including diaphragms, longitudinal stiffeners, corner reinforcement, inner cruciform plates, corner plates, and concrete infill, improve column strength and ductility (Susantha, Aoki, Kumano, & Yamamoto, 2005). Setting diaphragms in short distances along a column's height delays the occurrence of local buckling (Ge, Gao, & Usami, 2000). New thin-walled corrugated and cellular steel columns demonstrate superior performance in strength, ductility, and post-buckling behavior under constant axial and cyclic lateral loading (Ucak & Tsopelas, 2014). Columns with tapered plates improved the ultimate strength and ductility of steel bridge piers (Mamaghani & Packer, 2002; Mamaghani, 2005).

In this current study, a tested uniform thin-walled steel-stiffened box column (B) was numerically studied under constant axial and cyclic lateral loading. The comparison between the obtained results from the FE analysis and the experiment confirmed the validity of the FE analysis. Then, a GB column with size and volume of material equivalent to a B column was proposed to improve the strength, ductility, and post-buckling behavior of B columns. The results indicated that an improvement of 24% in the ultimate strength could be achieved using the GB columns. The GB column delays the occurrence of local buckling. Moreover, it was concluded that local buckling is less severe in the case of the GB column, as compared to its counterpart B column. The dissipated energy of the graded-thickness steel tubular columns was higher and also exhibited higher ductility. The main reason for the improved behavior of the GB columns was their ability to eliminate the severity of local buckling near the column base, where buckling usually occurs.

Finite Element Analysis

There is no doubt that full-scale testing results in better insight into understanding a structure's behavior; however, physical experimentation is expensive, and time consuming. For this study, then, finite element analysis was conducted on the thin-walled steel-stiffened box columns cyclic behavior using ABAQUS software (Hibbit, Karlsson, & Sorensen, 2014). The FEM takes into account both material and geometric nonlinearities. The key design parameters considered in this practical design of thin-walled steel box columns were R_f and λ (Mamaghani & Packer, 2002). R_f is concerned with the local buckling behavior of thin-walled steel box columns, while λ controls the global buckling (Fukumoto, 2004; Usami & Ge, 1998). These parameters are defined by Equations 1 and 2, respectively:

$$R_f = \frac{b}{t}\frac{1}{n\pi}\sqrt{3\left(1-\nu^2\right)\frac{\sigma_y}{E}} \qquad (1)$$

$$\lambda = \frac{2h}{r}\frac{1}{\pi}\sqrt{\frac{\sigma_y}{E}} \qquad (2)$$

where, h is column height; r is the radius of gyration; σ_y is yield stress; E is Young's modulus; v is Poisson's ratio; b is cross-sectional width; n is the number of subpanels of each plate; and, t is plate thickness.

Under constant axial and cyclic lateral loading, local buckling usually occurs near the column's base (Nishikawa et al., 1998). Figure 1 shows, for purposes of this study, that beam element B31 was employed for the upper part of the column (h-$2b$), and a four-node shell element S4R with reduced integration was used for the lower part of the column ($2b$). S4R elements are able to accurately model the local buckling effect. All elements needed for this study were available in the ABAQUS library (Hibbit, Karlsson, & Sorensen, 2014). The interface between S4R and B31 elements was modeled using multi-point constraint (MPC). The column was fixed at its base and subjected to a constant axial load (P) and cyclic lateral displacement at the top. For computational efficiency, the bottom half of the lower part (b) was divided into 26 S4R elements, while the remaining height (b) was only divided into 14 S4R elements. The upper part of the column (height of h-$2b$) was divided into 14 elements. The mesh divisions presented above were determined by trial and error. Such mesh sizes give accurate results without increasing the computational time. The initial geometrical imperfection and residual stresses were not accounted for in the FE analysis, as their effect was not measured for the tested column (Nishikawa et al.,1998). Moreover, neither initial geometrical imperfection nor residual stresses had a significant influence on overall cyclic behavior after the first half-cycle (Ge, Gao, & Usami, 2000; Takaku, Fukumoto, & Aoki, 2004; Hibbit, Karlsson, & Sorensen, 2014). Table 1 lists the geometrical properties of the analyzed columns.

Table 1. Geometrical and material properties of the B column.

Properties	B Column *	GB Column
Steel Material	SM490	SM490
h (mm)	3403	3403
b (mm)	900	900
$t_1/t_2/t_3$ *(mm)*	9	11.25/ 9/ 7.75
b_s/t_s *(mm)*	80/6	80/6
(ns +1) x *l*	4x225	4x225
λ	0.26	0.26
R_f	0.56	0.56
H_y *(KN)*	1039	1039
δ_y *(mm)*	13.8	13.8
$P/\sigma_y A_s$	0.122	0.122
σ_y *(MPa)*	378.6	378.6
σ_u *(MPa)*	630	630
E (GPa)	206	206
v	0.3	0.3

*Reported in (Nishikawa et al., 1998)

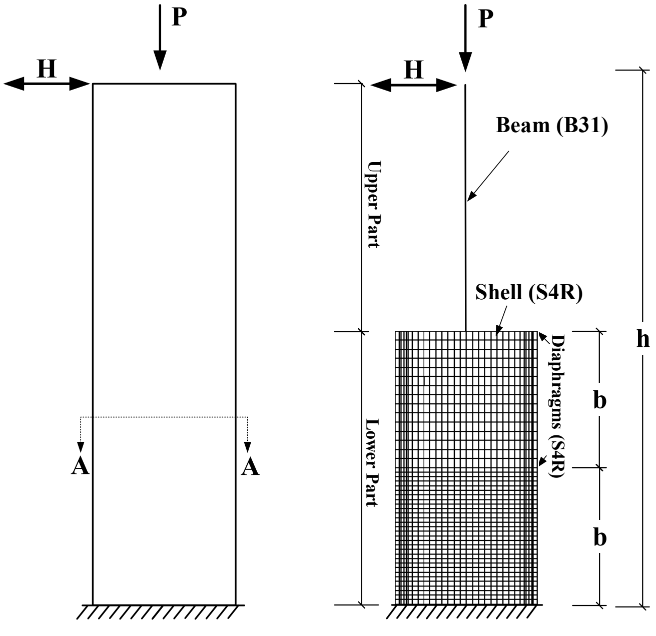

(a) Column. (b) FE meshing.

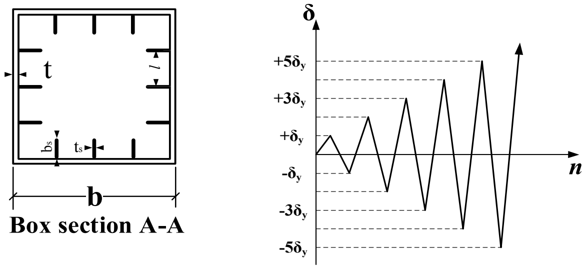

(c) Cross Section. (d) Loading program.

Figure 1. B column model.

Cyclic Loading Program

Figure 1(d) illustrates how displacement-controlled unidirectional cyclic loading was adopted as a lateral loading program. At the top of the column, a combination of quasi-static cyclic lateral loading and a constant axial load (*P*) was applied throughout the loading history. The displacement amplitude of the cyclic displacement was increased as a multiple of the yield displacement, δ_y, which is defined by Equation 3:

$$\delta_y = \frac{H_y h^3}{3 E_s I_s} \qquad (3)$$

where, $H_y = (\sigma_y - P/A)\, Z/h$ is lateral yield load, and A, h, EI, and Z are the cross-sectional area, height, bending stiffness, and section modulus, respectively, of the B column (Goto, Kumar, & Kawanishi, 2010).

Table 1 lists the lateral yield load and yield displacement of the tested column. All of the analyzed columns were assumed to be made of carbon steel SS400 (JIS, 2012), equivalent to ASTM A36 (ASTM, 2014).

Thin-Walled Steel-stiffened Box Columns with Graded Thickness

Uniform B columns suffer premature buckling behavior (local buckling, global buckling, or a combination of both), near the column base, under constant axial and cyclic lateral loading (see Figure 1). This buckling behavior makes these columns unable to utilize their full strength and ductility. To overcome these shortcomings, graded-thickness stiffened box columns (GB) were used as alternatives for the counterpart conventional uniform B columns. Column height and width were kept the same for both B and GB columns. The GB column was divided into three segments of constant cross sections. The first and second segments had a height equal to the width (b) of the box section from the base. The third segment had a height of h-2b. Figure 2 shows that a thicker cross section (t_1=1.25t) was used along the first segment, and the original thickness (t_2= t) was kept for the second segment. Finally, the remaining material volume was distributed on the third segment with t_3=0.86t. These configurations of graded-thickness sections were chosen based on which achieved the better behavior. Table 1 shows material and geometrical properties of the B and GB columns. As seen in Table 1, the same material and geometrical properties (except for the plate thickness) were used for both B and GB columns.

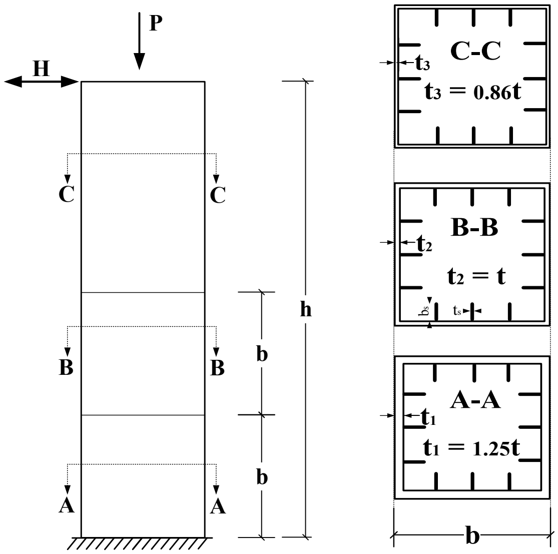

(a) Column. (b) Graded-thickness sections.

Figure 2. GB column model.

Comparison of Numerical and Experimental Results: Hysteresis Curves of B Columns

The numerical results of the thin-walled steel-stiffened box columns' cyclic behavior were compared to the experimental results obtained by the Public Works Research Institute (PWRI) of Japan (Nishikawa et al., 1998). Figure 3(a) shows the normalized lateral load versus lateral displacement hysteresis curves of the B column obtained from the FE analysis and experiment. Also in this figure, H_y and δ_y denote the lateral yield load and yield displacement, respectively. The comparison of the hysteresis curves of the B column showed reasonable agreement with the experimental results. This indicates that FE analysis, using kinematic hardening material behavior, can provide reasonable accuracy in describing material behavior with regard to local buckling of thin-walled steel-stiffened box columns. At the end of the FE analysis, the buckling shape of the B column [see Figure 4(b)] was compared to the experimental buckling shape [see Figure 4(a)] (Nishikawa et al., 1998). In the experiment, the flange suffered from inward local buckling, while the web buckled outward above the base of the column. The buckling shape was predicted relatively well by the adopted FEM. However, the outward buckling of the web in the analysis was not as prominent as in the experiment.

Effect of Longitudinal Stiffeners on B Column Behavior

Figure 5 compares the effect of the longitudinal stiffeners on the lateral load and lateral displacement of the analyzed B columns with and without longitudinal stiffeners. The results indicate that cyclic behavior of the B column is greatly enhanced with the longitudinal stiffeners. For example, the normalized lateral versus lateral displacement of the B column with longitudinal stiffeners was $H_{max}/H_y = 1.41$, while the $H_{max}/H_y = 0.65$ for the B column without the longitudinal stiffeners. Figure 4 shows that local buckling was more severe for the B column without longitudinal stiffeners [see Figure 4(d)] as compared to the B column with longitudinal stiffeners [see Figure 4(b)]. Obviously, longitudinal stiffeners prevent severe local buckling of the B column.

Hysteresis Curves of B and GB Columns

From Figure 3(a), a comparison of the FE analysis and the experimental results indicate that the FEM is able to predict the nonlinear structural behavior with reasonable accuracy. Using the validated FEM, a comparison study was performed between the behavior of the B and GB columns under the same loading conditions. Figure 3(b) compares the hysteretic behavior of B and GB columns obtained from the FE analysis. The normalized ultimate strength (H_{max}/H_y) and normalized maximum displacement (δ_m/δ_y) of the GB column were greater than the B column by 24% and 32%, respectively. In the case of the B column, the buckling started when the displacement was between $2\delta_y$ and $3\delta_y$. A drop of 36% of the ultimate strength (i.e., $H_{max}/H_y = 1.33$ observed at $\delta = +2.28\delta_y$) occurred at $\delta = +4\delta_y$. As the displacement increased, the column strength decreased at a fast rate to 14% of its maximum strength by the end of the analysis. By contrast, the GB column showed its H_{max}/H_y at $\delta = +3\delta_y$, which indicated that the local buckling occurred between $3\delta_y$ and $4\delta_y$. Only a 9% drop of the H_{max}/H_y takes place at $\delta = +4\delta_y$, while the residual strength of the GB column was 25% of its H_{max}/H_y at $\delta = +8\delta_y$.

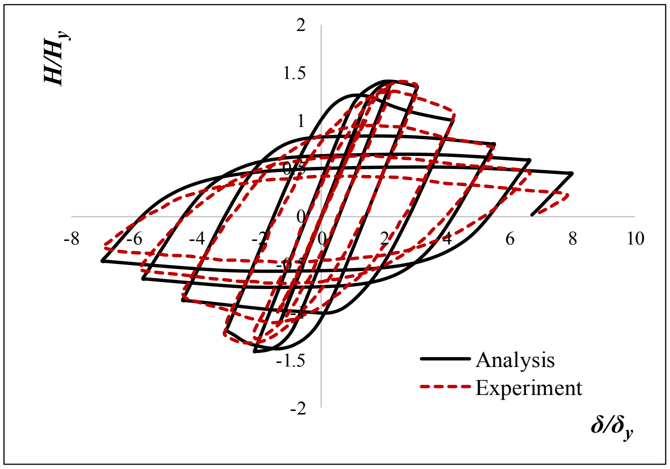

(a) Experiment versus analysis.

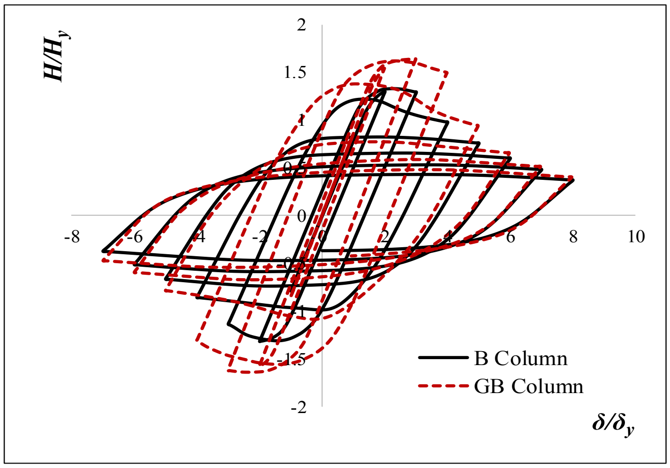

(b) B column versus GB column.

Figure 3. Comparison of lateral load versus lateral displacement hysteresis curves.

This comparison showed the superiority of the GB column and delay of local buckling occurrence in the GB column compared to the B column. The final buckling shape of the GB column [see Figure 4(c)] was compared to the B column [see Figure 4(b)] at the end of the analysis. The comparison showed that buckling was less severe in the case of the GB column, when compared to its counterpart B column. The main reason for the improved behavior of the GB columns was their ability to eliminate severe local buckling near the base of the column where the buckling usually occurs.

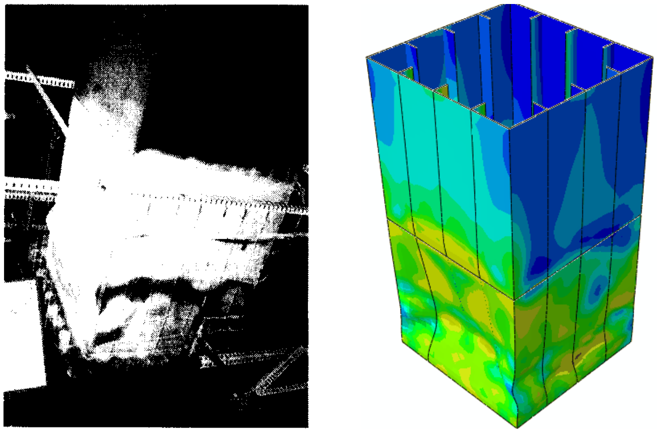

(a) *Experiment. (b) B column with stiffeners.

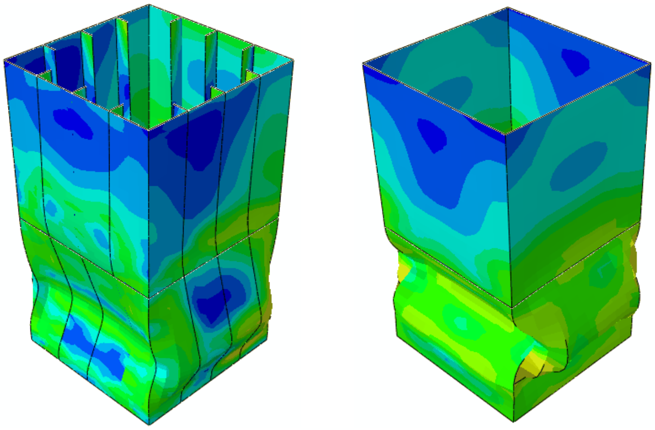

(c) BG column. (d) B column without stiffeners.

Figure 4. Buckling shapes of columns.
(*reported in Nishikawa et al., 1998)

Energy Absorption Capacity

Dissipated energy was an objective indicator of the inelastic cyclic behavior of the structures. Accordingly, the energy absorption capacity of the column was evaluated under cyclic behavior. Normalized energy absorption, E, is defined this way (Mamaghani, Shen, Mizuno, & Usami, 1995). In Equation 4, E_i is energy absorption in the i-th half-cycle and n is the number of half-cycles (one half-cycle is defined from any zero-lateral load to the subsequent zero-lateral load). Figure 6(a) shows a comparison of the normalized cumulative energy absorption versus the number of half-cycles obtained from the analysis and experiment of the B column. The normalized energy absorption curves versus the number of half-cycles obtained from the analysis fit very close with the experimental results. Figure 3(b) shows that the strength of the GB columns decreases in a controlled rate from cycle to cycle compared to the B column, which was expected to dissipate more energy than the B column under cyclic lateral loading. As an alternative method, the area under lateral load versus lateral displacement curves was calculated. Figure 6(b) shows that the dissipated energy of the GB column was higher than the B column, which was expected to experience higher ductility in the case of the GB column.

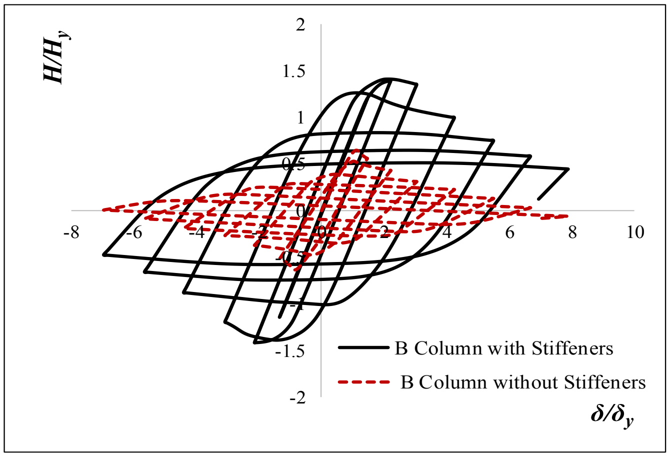

Figure 5. Effect of longitudinal stiffeners.

$$E = \frac{2}{H_y \delta_y} \sum_{i=1}^{n} E_i \tag{4}$$

Conclusions

In this study, the authors carried out an FE analysis to evaluate the cyclic behavior of a conventional B column with a uniform cross section. In addition, a GB column with size and volume of material equivalent to a B column was introduced to improve the strength, ductility, and post-buckling behavior. First, the validity of the employed FEM was verified using the B column experimental results reported in the literature. The reasonable agreement between the FE analysis and experimental results confirms that the employed FEM can be used to capture structural behavior with taking into account the local buckling behavior of thin-walled steel-stiffened box columns. The GB column of graded section showed superior strength and ductility performance (i.e., an improvement of 24% in the ultimate strength was achieved using the GB columns). Buckling behavior of the B columns was captured relatively well by the FEM. The GB column delays the occurrence of local buckling and local buckling was less severe in the case of the GB column when compared to its counterpart B column. Moreover, the dissipated energy of the GB columns was higher and exhibited higher ductility. Finally, the cyclic behavior of the B column was greatly improved with longitudinal stiffeners.

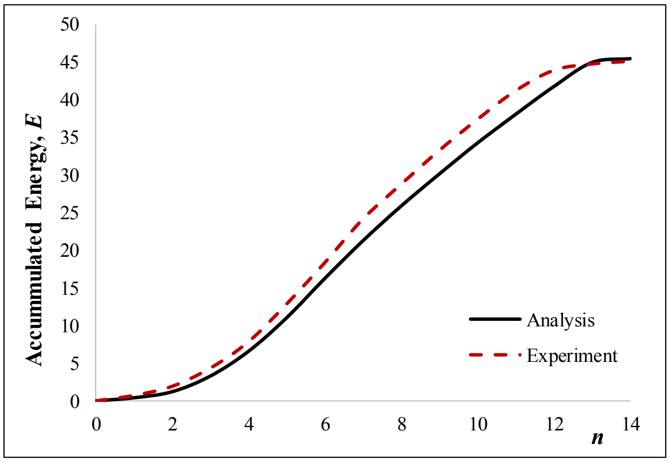

(a) Experiment versus analysis.

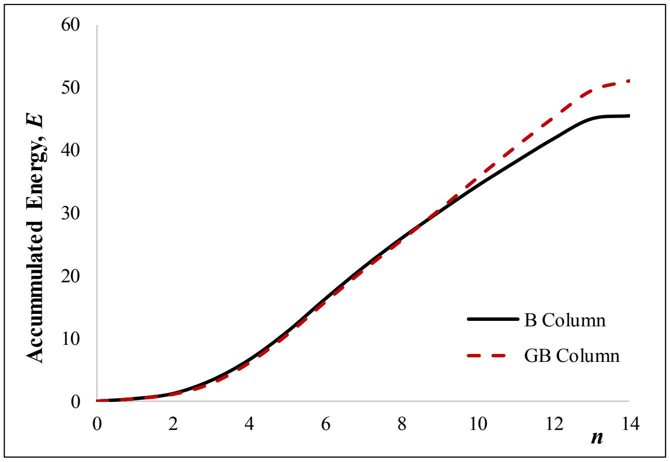

(b) B column versus GB column.

Figure 6. Energy absorption capacity.

References

Al-Kaseasbeh, Q. (2015). *Electrochemical investigation of corrosion resistance of weldments in steel bridges*. Fargo, ND: North Dakota State University.

Al-Kaseasbeh, Q., Lin, Z., Wang, Y., Azarmi, F., & Qi, X. (2018). Electrochemical characterization of steel bridge welds under simulated durability test. *Journal of Bridge Engineering*, *23*(10). doi: 10.1061/(asce)be.1943-5592.0001246

ASTM. (2014). ASTM A36/A36M-14 standard specification for carbon structural steel. West Conshohocken, PA: ASTM International.

Bruneau, M. (1998). Performance of steel bridges during the 1995 Hyogoken–Nanbu (Kobe, Japan) earthquake—A North American perspective. *Engineering Structures*, *20*(12), 1063-1078.

Fukumoto, Y. (2004). Cyclic performance of stiffened square box columns with thickness tapered plates. *Proceedings of the 2004 Annual Stability Conference*. Bethlehem, PA: SSRC.

Ge, H., Gao, S., & Usami, T. (2000). Stiffened steel box columns. Part 1: Cyclic behaviour. *Earthquake Engineering and Structural Dynamics*, *29*(11), 1691-1706.

Goto, Y., Wang, Q., & Obata, M. (1998). FEM Analysis for hysteretic behavior of thin-walled columns. *Journal of Structural Engineering*, *124*(11), 1290-1301.

Goto, Y., Kumar, G., & Kawanishi, N. (2010). Nonlinear finite-element analysis for hysteretic behavior of thin-walled circular steel columns with in-filled concrete. *Journal of Structural Engineering*, *136* (11), 1413-1422.

Hibbit, D., Karlsson, B., & Sorensen, P. (2014). *ABAQUS 2014 documentation*. Providence, RI: Dassault Systèmes.

JIS. (2012). *JIS handbook: Ferrous materials & metallurgy*. Tokyo, Japan: Japanese Standards Association.

Kwon, Y. B., Kim, N. G., & Hancock, G. J. (2007). Compression tests of welded section columns undergoing buckling interaction. *Journal of Constructional Steel Research*, *63*(12), 1590-1602.

Mahin, S. A. (1998). Lessons from damage to steel buildings during the Northridge earthquake. *Engineering Structures*, *20*(4-6), 261-270.

Mamaghani, I. H. P. (1996). *Cyclic elastoplastic behavior of steel structures: Theory and experiment*. Nagoya, Japan: Nagoya University.

Mamaghani, I. H. P. (2005). Assessment of earthquake resistance capacity and retrofit of steel tubular bridge piers. *Structural Engineers Association of California*, 357-370.

Mamaghani, I. H. P. (2008). Seismic design and ductility evaluation of thin-walled steel bridge piers of box sections. *Transportation Research Record: Journal of the Transportation Research Board*, *2050*(1), 137-142.

Mamaghani, I. H. P., & Packer, J. A. (2002). Inelastic behaviour of partially concrete-filled steel hollow sections. In *4th Structural Specialty Conference* (pp. 1–10). Montréal, Québec, Canada: Canadian Society for Civil Engineering.

Mamaghani, I. H. P., Usami, T., & Mizuno, E. (1996). Inelastic large deflection analysis of structural steel members under cyclic loading. *Engineering Structures*, *18*(9), 659-668.

Mamaghani, I. H. P., Shen, C., Mizuno, E., & Usami, T. (1995). Cyclic behavior of structural steels. I: Experiments. *Journal of Engineering Mechanics*, *121*(11), 1158-1164.

Miller, D. K. (1998). Lessons learned from the Northridge earthquake. *Engineering Structures*, *20*(4-6), 249-260.

Nakashima, M., Inoue, K., & Tada, M. (1998). Classification of damage to steel buildings observed in the 1995 Hyogoken-Nanbu earthquake. *Engineering Structures*, *20*(6), 271-281.

Nishikawa, K., Yamamoto, S., Natori, T., Terao, K., Yasunami, H., & Terada, M. (1998). Retrofitting for seismic upgrading of steel bridge columns. *Engineering Structures*, *20*(4-6), 540-551.

Susantha, K. A. S., Aoki, T., Kumano, T., & Yamamoto, K. (2005). Applicability of low-yield-strength steel for ductility improvement of steel bridge piers. *Engineering Structures*, *27*(7), 1064-1073.

Takaku, T., Fukumoto, Y., & Aoki, T. (2004). Seismic design of bridge piers with stiffened box sections using LP plates. *Proceedings of the 13th World Conference on Earthquake Engineering*. Tokyo, Japan: International Association for Earthquake Engineering.

Ucak, A., & Tsopelas, P. (2014). Load path effects in circular steel columns under bidirectional lateral cyclic loading. *Journal of Structural Engineering*, *141*(5), 1-11.

Usami, T., & Ge, H. (1998). *Cyclic behavior of thin-walled steel structures—numerical analysis*. *Thin-walled structures* (vol. 32). Cambridge, MA: Elsevier.

Yang, C., Zhao, H., Sun, Y., & Zhao, S. (2017). Compressive stress-strain model of cold-formed circular hollow section stub columns considering local buckling. *Thin-Walled Structures*, *120*, 495-505.

Biographies

QUSAY AL-KASEASBEH is a PhD candidate in the civil engineering program at the University of North Dakota. He earned his BSc in Civil Engineering from Mutah University, Jordan, in 2013 and MSc in Civil Engineering from North Dakota State University in 2016. His main research interests include cyclic plasticity modeling of structural steel, advanced numerical analysis, stability and ductility evaluation of thin-walled steel structures, and seismic design of steel structures. Mr. Al-Kaseasbeh may be reached at qusay.alkaseasbeh@ndus.edu

IRAJ H.P. MAMAGHANI is an associate professor of civil engineering at the University of North Dakota. He works in the area of civil engineering, with emphasis on structural mechanics and structural engineering. His areas of research interest include cyclic elastoplastic material modeling, structural stability, seismic design, advanced finite element analysis, and ductility evaluation of steel structures. Dr. Mamaghani may be reached at iraj.mamaghani@engr.und.edu

A SIMPLIFIED ALGORITHM FOR AUTOMATED ROTATION CORRECTION OF SCANNED DISTORTION GRID TARGETS

Martin P. Jones, Missouri State University; Kevin M. Hubbard, Missouri State University; Nebil Buyurgan, Missouri State University

Abstract

Common flatbed scanners have been utilized by researchers for the dimensional measurement of a wide variety of objects. Although not the most accurate measurement tool, flatbed scanners are convenient and can be calibrated to achieve the required accuracy for many applications. In this paper, the authors describe a general method for calibrating flatbed scanners using a 151 x 151 dot distortion grid target with details about its key algorithm of rotation correction. This algorithm also enables the generation of a theoretical grid of points that can be compared to the dots' centroids obtained by scanning. By calculating the distance between the theoretical grid and scanned centroids, a novel 8-bit grayscale distortion map of the scanned image was obtained. The map showed periodic distortion across the scanning bed.

Introduction

It has been over 60 years since the first digital image of a photograph was generated from a scanner invented by researchers at the National Institute of Standards and Technology (NIST). That image spawned many other imaging technologies, such as satellite imaging, packaging bar codes, medical imaging, and desktop publishing (NIST, 2007). Flatbed scanners are commonly used for desktop publishing but have also been used by other researchers for the dimensional measurement of a wide variety of objects (Jones, Callahan, & Bruce, 2011; Kee, & Ratnam, 2009; Korin, Larrainzar, & Ipina, 2008; Miriello & Crisci, 2006; Ng, 2008; Paliwal, Borhan, & Jayas, 2004; Van Dalen, 2004; Wang, Zeng, Wang, Li, Xu, & Yao, 2016; Zalocha & Kasperkiewicz, 2005).

In this paper, the authors describe the basis of a simplified method to calibrate common flatbed scanners that can enable the convenient dimensional measurement of such objects. While the common flatbed scanner might not be the most accurate scanner for dimensional measurement, its cost and availability make it an attractive tool for an engineer or scientist needing a quick but sufficiently accurate measurement of an object. A scanner calibration method to assess accuracy should be low-cost and straightforward to interpret. While the authors used a relatively high-cost (~$1500) distortion target etched on glass for this project, similar lower-cost (<$300) targets could be used instead for practical applications. Adequate distortion targets can be printed onto plastic sheets at minimal costs, if a high-quality printer is available (Elaksher & Ali, 2018). As will be described, a novel grayscale distortion map was created to assist in the straightforward interpretation of calibration data.

Calibration of the dimensional precision and accuracy of flatbed scanners can be performed using distortion grid targets and scale rulers (Jones, Callahan, & Bruce, 2012; Kangasraasio & Hemming, 2009; Poliakow, Poliakov, Fedotova, L. A., & Tsvetkov, 2007; Zheng, Ou, & Yang, 2014). Both the targets and rulers have calibration marks fabricated from etched chromium on glass plates. A common distortion grid target consists of an array of equally spaced chromium dots. If the scanned dots' positions appear to vary from their expected positions, then local stretching or contraction (distortion) of the image can be quantified and measurement error assigned. The first step in determining image distortion is to verify that the centroid of every imaged dot can be mapped to its corresponding physical dot on the glass plate. Such verification becomes problematic when the distortion grid target is unavoidably tilted at some unknown angle relative to the axis of the scanning bed. This tilt problem is similar to a more complicated tilt problem encountered by researchers while performing genetic analyses using microarray grids (Giannakeas, Kalatzis, Tsipouras, & Fotiadis, 2016; Morris, Wang, & Liu, 2007; Shao, Yang, Zhang, Zhou, & Luo, 2013). In this paper, the authors describe a simplified algorithm for distortion grid rotation correction of tilt that is related to a correction algorithm developed by the authors. The simplification was enabled by the symmetry of the selected distortion grid target compared to geometrical complexities of microarray grids.

Calibration Method

The calibration distortion target consisted of a 151 x 151 chromium-etched dot array on a glass plate (Edmund Optics stock #62-207). Each dot was 0.500 ± 0.002 mm in diameter and spaced 1.000 ± 0.001 mm from other dots. The overall accuracy was ± 0.002 mm. Scanning was performed using an HP Scanjet N6310 desktop scanner. Figure 1 shows the upper left corner of the target scanned at 300 dots-per-inch (dpi) and with an 8-bit grayscale resolution.

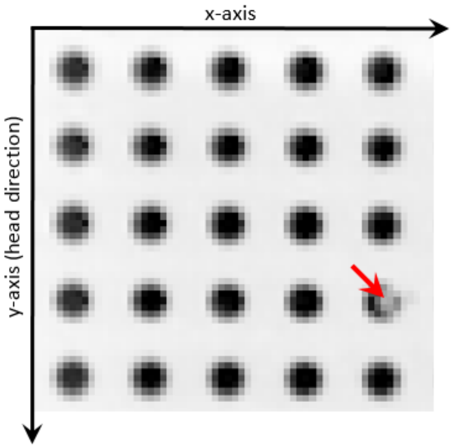

Figure 1. Scan of a grid target.

Figure 1 further illustrates some key aspects of a typical scan. Although the array is tilted clockwise only about 0.38° with respect to the x-axis, even such a small angle of tilt results in the incorrect mapping of the scanned dots. Incorrect mapping can also result from dots that have noncircular images and/or images that are too small to be detected. The red arrow points to a scanned dot that has such a noncircular shape. This non-circularity is probably due to various electronic and mechanical noise sources, since the dot image becomes circular when rescanned without repositioning the target. While it is possible to minimize such noise using filtering techniques (Weyori & Boateng, 2013), this calibration method does not require it. Figure 2 illustrates the overall calibration method that includes the "Rotation Correction" algorithm.

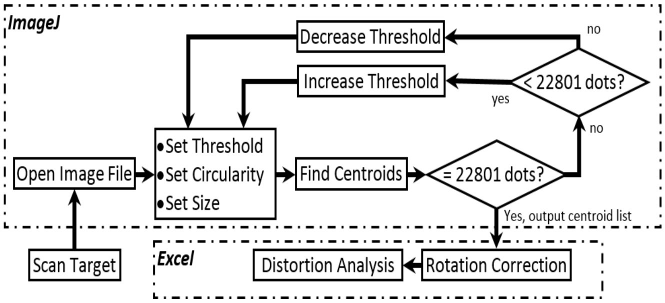

Figure 2. Flowchart of the calibration method.

Starting in the lower left corner of the figure, the target can be scanned at various pixel resolutions from 300 to 2400 dpi using software supplied by the scanner manufacturer. Higher resolutions require longer scan times. The calibration scan resolution selected should be the same as the scan resolution that will be used to measure an object. Next, the scanned image file is imported into ImageJ software, which is available as a free download from the National Institutes of Health (NIH, 2018). Within this software, the user selects the image processing properties of "Threshold," "Circularity," and "Size." The threshold level chosen determines at what 8-bit grayscale value a pixel is part of a dot. The grayscale used assigns 0 as black (no reflection) and 256 as white (complete reflection). The calibration method used by the authors in this study assumed a default threshold value of 180. This means that any pixel with a grayscale value of 180 or less was considered part of the actual dot and assigned a grayscale value of 0. The threshold can also be lowered or increased by the user as needed. The software method of centroid calculation used a simple average of the x and y coordinates of all pixels that met the threshold criteria of being part of a dot.

The circularity property was chosen to allow noncircular imaged dots to be counted as an imaged dot. Circularity values are defined within ImageJ software to range from 0.00 (infinitely elongated) to 1.00 (perfect circle). A range of 0.50 to 1.00 circularity was chosen by the authors for the current method. The size property is the range chosen to discriminate between an actual dot and local grayscale variations, due to electronic noise, dust, etc. The size range sets the limits on the expected area of an imaged dot based on the pixel size of the scan resolution. Ideally, the image area of a 0.5 mm diameter dot scanned at 300 dpi should be about 27 pixels. The size range of 13 to 52 pixels was chosen for this study.

Once the image properties have been chosen, the centroid coordinates of each of the imaged 22,801 dots (151 x 151) are searched for using the "Analyze Particles" command within the ImageJ software. If all 22,801 centroids are found, then a list of their coordinates is sent to *Excel* to correct for any tilt of the target relative to the scan axis. If the particle analysis identifies less than 22,801 centroids, then the grayscale threshold is increased incrementally until all centroids are identified. Increasing the threshold will increase the apparent size of an imaged dot. For example, the dot indicated by the arrow in Figure 1 might have an unacceptable size and circularity at a threshold of 180, but be acceptable at a threshold of 190. This is because more of the whiter pixels would be counted as part of the dot. If the particle analysis identifies more than 22,801 centroids, then the threshold is decreased incrementally until only the actual dot centroids are identified. Regardless of what threshold is ultimately successful, it is recommended to use that threshold when measuring objects post calibration. Otherwise, as noted earlier, the size and shape of the imaged object might be less accurate and unacceptable.

Tilt Problem

Once all of the centroids' coordinates have been obtained, they must be mapped so that each coordinate pair (x, y) can be identified with its corresponding physical dot on the target. The list order should be in the form of an ordered array so that it can be mathematically addressable for distortion analysis. For example, an ordered array could start with the upper left dot of the target, then go to the next dot down, and so on (150 times) until the lower left dot of the grid target is reached. This would represent the left column of dots in the grid. This order would then repeat for the next column until the lower right dot of the grid is reached. However, the centroids' coordinates generated by ImageJ are often listed in random order. The randomness of the list is a function of the tilt angle, which is intrinsically random, for reasons that will be explained next. For example, Figure 3 shows that the first seven centroids' coordinates of the first column of dots might be listed in the correct order going from upper left (UL) to lower left (LL), but the eighth centroid's coordinates listed might correspond to the eighth dot of the second column instead of the expected first column (i.e., column skipping).

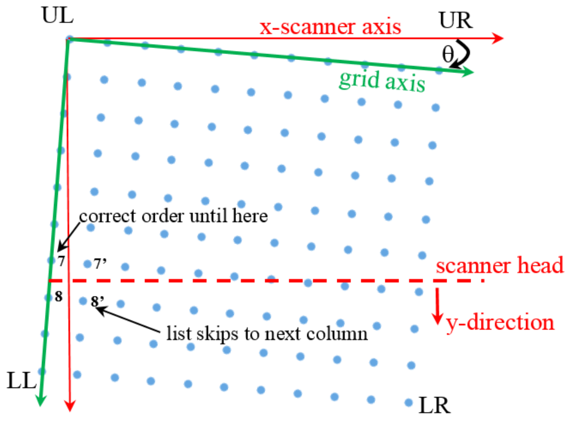

Figure 3. Example of a grid-tilt problem.

The list skip is dependent on the position of the next dot relative to the x-direction. Figure 3 further shows that the distance of point 8' in the x-direction is less than that of point 8. The reverse is true for points 7 and 7'. Therefore, the list is sorted in the order that gives the next dot closest in the x-direction. As the tilt angle (θ) decreases, the point at which the list skips to the second column occurs further down the first column. If θ = 0, then there is no list skip to the second column. Using basic trigonometry and the spacing of the dots on the target, the largest tilt that can be allowed for skipping not to occur is about 0.191°. Thus, skipping randomizes the list of centroid coordinates and must be corrected. Therefore, high-precision mechanical alignment or, as developed in this study, a mathematically ordered array will be needed. In Figure 3, θ was chosen to be about 5°, which is much greater than the angle of tilt that is typically present. This large angle was used to clearly show how the list order of the centroids' coordinates could skip rows.

In practice and with moderate care, θ is typically within ± 0.5º. Some of this tilt is due to the sliding of the glass target on the scanner's glass platen when the scanner's cover is lowered onto the target during a scan. In the current study, alignment fixtures were devised to minimize the amount of target sliding and minimize the distortion of both target and platen that can be induced by fixture pressures. However, as with any mechanical system, there will be some misalignment (tilt) of the scanning axis with respect to the platen axis during manufacture. Also, there will be some scanning error in locating the true centroids. Therefore, a reverse tilt (rotation) correction algorithm was developed to enable proper sorting and identification of the list of the dot centroids' coordinates.

Rotation Correction Algorithm

The purpose of the rotation algorithm is to sort the centroids into an ordered array. Figure 2 shows that the list of centroid coordinate pairs was transferred from ImageJ to Excel in order to be sorted in the process box labeled "Rotation Correction" and to enable mathematical analysis of the distortion present in a scanned image. The sorting of the coordinate pairs was accomplished by rotating all of the pairs mathematically so that the grid axis and the scanner axis were correctly aligned (i.e., θ ≈ 0°). The following eight steps provide an overview of the rotation correction algorithm.

1. Locate the grid's center:

   The coordinates of the grid's center, defined as C, are located by computing the average x coordinate, $\bar{x}$, and the average y coordinate, $\bar{y}$, of all centroids using Equations 1 and 2:

$$\bar{x} = \frac{\sum_{i=1}^{n} x_i}{n} \tag{1}$$

$$\bar{y} = \frac{\sum_{i=1}^{n} y_i}{n} \tag{2}$$

where, n = 22,801 (number of grid dots).

2. Calculate the distance of dots from center:

The distance from each dot's centroid to the grid's center can be calculated using the well-known distance formula. However, this would unnecessarily apply a square root, resulting in longer computation times. For the purposes of the algorithm, the distance squared, d_i^2, of every dot's centroid from the grid's center can be used in place of distance. The distance squared is given by Equation 3:

$$d_i^2 = \left(\bar{x} - x_i\right)^2 + \left(\bar{y} - y_i\right)^2 \tag{3}$$

3. Sort the distance:

Sort d_i^2 from maximum value to minimum value. The four maximum values correspond to the four corner dots of the grid and then define those as d_m^2, where m = 1, 2, 3, and 4. Define the corresponding coordinate pairs as x_m, y_m.

4. Identify the corner dots:

Figure 3 shows the designation of the four corner dots as upper left (UL), upper right (UR), lower left (LL), and lower right (LR). The following logic was used to identify which coordinate pairs x_m, y_m corresponded to each corner dot.

If $\bar{x} - x_m > 0$ and $\bar{y} - y_m > 0$, then UL dot
If $\bar{x} - x_m < 0$ and $\bar{y} - y_m > 0$, then UR dot
If $\bar{x} - x_m > 0$ and $\bar{y} - y_m < 0$, then LL dot
If $\bar{x} - x_m < 0$ and $\bar{y} - y_m < 0$, then LR dot

The coordinates of the corner dots was defined as:

x_{UL}, y_{UL} for UL dot
x_{UR}, y_{UR} for UR dot
x_{LL}, y_{LL} for LL dot
x_{LR}, y_{LR} for LR dot

5. Calculate θ:

The angle of tilt, θ, can be approximately calculated using the coordinates of the corner dots and the coordinates of the grid center. Figure 4 depicts a tilted grid relative to the scanner axes and ten measures of θ (i.e., θ_1 thru θ_{10}).

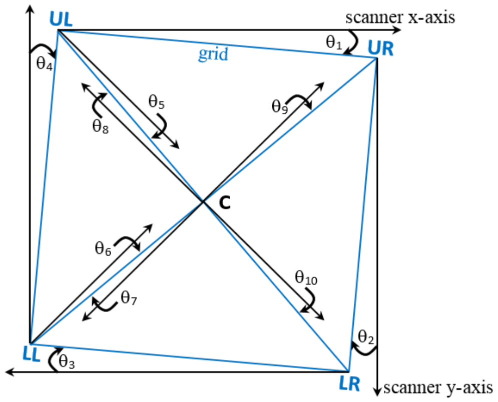

Figure 4. Ten measures of the tilt angle (θ).

Note that Figure 4 uses the left-handed Cartesian coordinate system that is common in 2D computer graphics. Ten measures of θ were used to calculate the average measured tilt angle, $\bar{\theta}$. This average tilt angle was used to minimize the error in determining θ. Due to image distortion and resolution limitations of the scanner, there will likely be some error in the location of the four corners and center of the grid. While it is possible to use more measures of θ than depicted in Figure 4, these ten measures of θ were found to provide the necessary accuracy to successfully perform the algorithm over a wide range of θ (clockwise and counter-clockwise) and scanner resolutions. Equation 4-13 provide the calculations for the ten measures of θ:

$$\theta_1 = \left| \tan^{-1}\left[\frac{y_{UL} - y_{UR}}{x_{UL} - x_{UR}}\right] \right| \tag{4}$$

$$\theta_2 = 90^\circ - \left| \tan^{-1}\left[\frac{y_{UR} - y_{LR}}{x_{UR} - x_{LR}}\right] \right| \tag{5}$$

$$\theta_3 = \left| \tan^{-1}\left[\frac{y_{LL} - y_{LR}}{x_{LL} - x_{LR}}\right] \right| \tag{6}$$

$$\theta_4 = 90^\circ - \left| \tan^{-1}\left[\frac{y_{UL} - y_{LL}}{x_{UL} - x_{LL}}\right] \right| \tag{7}$$

$$\theta_5 = \left| 45^\circ - \tan^{-1}\left[\frac{y_{UL} - y_{LR}}{x_{UL} - x_{LR}}\right] \right| \tag{8}$$

$$\theta_6 = \left| 45^\circ + \tan^{-1}\left[\frac{y_{UR} - y_{LL}}{x_{UR} - x_{LL}}\right] \right| \tag{9}$$

$$\theta_7 = \left| 45^\circ + \tan^{-1}\left[\frac{\bar{y} - y_{LL}}{\bar{x} - x_{LL}}\right] \right| \tag{10}$$

$$\theta_8 = \left| 45^\circ - \tan^{-1}\left[\frac{\bar{y} - y_{UL}}{\bar{x} - x_{UL}}\right] \right| \tag{11}$$

$$\theta_9 = \left| 45^\circ + \tan^{-1}\left[\frac{\bar{y} - y_{UR}}{\bar{x} - x_{UR}}\right] \right| \tag{12}$$

$$\theta_{10} = \left| 45^\circ - \tan^{-1}\left[\frac{\bar{y} - y_{LR}}{\bar{x} - x_{LR}}\right] \right| \tag{13}$$

6. Determine the direction of tilt:

The previous measurement of $\overline{\theta}$ gives the approximate magnitude of the tilt, θ, between the scanner axes and the grid. Its direction must still be determined so that all of the centroids' coordinates can be mathematically rotated in the opposite direction in order to align with the scanner axes (i.e., θ ≈ 0°). Figures 3 and 4 depict a clockwise (CW) value of θ. Therefore, a counterclockwise (CCW) rotation of $\overline{\theta}$ would be needed for alignment. Similarly, a counterclockwise θ would need a clockwise rotation of $\overline{\theta}$ for alignment. The logic for determining the direction of θ is given as follows:

$$\text{If } \frac{y_{UL} - y_{UR}}{x_{UL} - x_{UR}} > 0, \text{ then } \theta \text{ is CW}$$

$$\text{If } \frac{y_{UL} - y_{UR}}{x_{UL} - x_{UR}} < 0, \text{ then } \theta \text{ is CCW}$$

7. Rotational correction of tilt:

To mathematically rotate all centroids so that the grid axis and the scanner axis are correctly aligned (i.e., θ ≈ 0°), the rotation matrix equations, given as Equations 14 and 15 were used for the CW tilt directions:

$$x_i' = x_i \cos\overline{\theta} + y_i \sin\overline{\theta} \tag{14}$$

$$y_i' = -x_i \sin\overline{\theta} + y_i \cos\overline{\theta} \tag{15}$$

where, x_i', y_i' and x_i, y_i are the rotated and original centroid coordinates of each dot (i = 1 to 22,801), respectively.

Note that the rotated coordinates maintain their original index number, *i,* so that each centroid can later be mapped to its original coordinates. This mapping is essential to the overall purpose of distortion analysis of scanners. Research has shown that the amount of distortion of a scanned object can vary depending on its location on the scanner's glass platen (Elaksher & Ali, 2018; Jones, Callahan, & Bruce, 2012). The user will want to select an area of low distortion based on the original coordinates to achieve the highest accuracy of the measurement of the object. Similarly, Equations 16 and 17 may be used to correct for CCW tilt:

$$x_i' = x_i \cos\overline{\theta} - y_i \sin\overline{\theta} \tag{16}$$

$$y_i' = x_i \sin\overline{\theta} + y_i \cos\overline{\theta} \tag{17}$$

8. Sort and reorder:

Each x_i', y_i' coordinate pair, along with its corresponding original index number, *i*, is then sorted in ascending order according to the x_i' coordinate value. Next, the first 151 x_i'-sorted coordinate pairs, along with their corresponding original index numbers, are sorted in ascending order according to the y_i' coordinate value. Therefore, the first column of centroids of the rotated grid is identified. This sorting method is then repeated 150 more times so that all centroids of the rotated grid are sorted in a mathematically addressable order. Each centroid is then reassigned to its original coordinates (x_i, y_i) by association with its corresponding original index number.

Results and Discussion

The rotation correction algorithm was applied to scans having several angles of tilt between +45° and -45°. The scanning resolution was also varied from 300 dpi to 2400 dpi. In all cases, the algorithm correctly sorted the 22,801 target grid centroids into ordered arrays. The ordered arrays retained their original centroids' coordinates relative to the scanner bed, thus enabling a novel approach to distortion analysis. An example of the novel distortion analysis is now given by comparing the positions of centroids obtained from the scanned distortion grid target with the theoretical positions of the centroids of a distortion-free grid image. An ordered array of theoretical centroids can be mathematically generated, based on the nominal dot spacing of the target grid and the selected scanning resolution. The details of this procedure are beyond the scope of this paper and will be described more appropriately in future work. However, the basic approach is to generate a theoretical grid of centroids and then rotate and translate them until they have the best fit with the centroids obtained from scanning the target. Simultaneously, the centroids obtained from scanning must be scaled independently along the x and y axes, as observed in previous research (Elaksher & Ali, 2018; Wyatt & Nave, 2017). The best-fit criterion is set to minimize the average distance between theoretical centroids and the corresponding centroids obtained from scanning. The minimization is accomplished using the "Solver" function within *Excel* by iteratively changing the tilt angle and center coordinates of the theoretical grid, while iteratively changing the x and y direction scale factors of the centroids' coordinates obtained from scanning. Figure 5 shows an 8-bit grayscale representation of the variation of the 22,801 distances between theoretical centroids and the corresponding centroids obtained by scanning at 300 dpi resolution starting at the top of the glass bed.

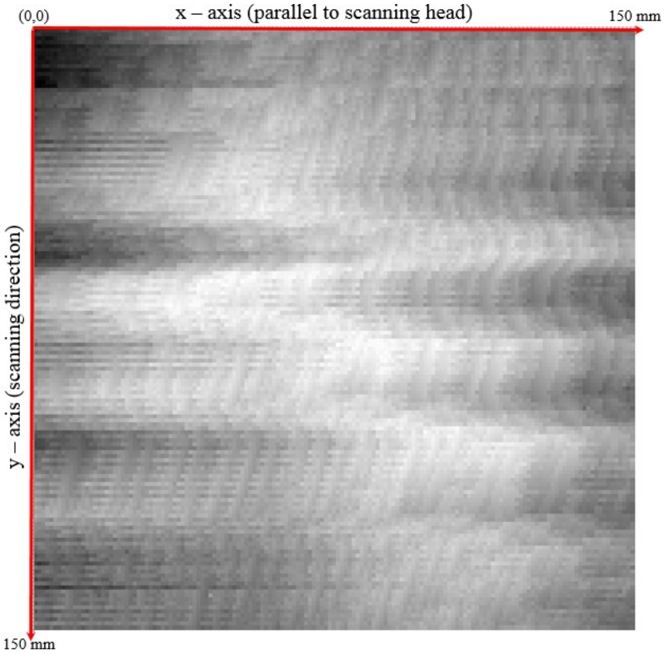

Figure 5. Grayscale map of distances between theoretical centroids and centroids obtained by scanning.

The average distance between the theoretical centroids and the centroids obtained from scanning was about 0.08 mm. Since the centroids should ideally be 1 mm apart, the average error was, then, about 8%. The greatest amount of error in distance was about 22.8% and the least amount of error was about 0.007%. The 8-bit grayscale in Figure 5 assigns the greatest error as completely black and least error as completely white. The high average error was expected for two main reasons. First, at a scan resolution of 300 dpi, an 8% error in the 1 mm dot distance is equivalent to an error of less than one pixel. Therefore, the average error in distance between the theoretical and scanned centroids is within the scanning resolution used. While higher resolutions were used (up to 2400 dpi), the 300 dpi scan data is presented in this paper to demonstrate the ability of the rotation correction algorithm to successfully sort the centroids obtained at low resolutions.

The second reason for the high average error was likely related to the periodic variation in the mechanical movement of the scanner head induced by gear rotation (Jones, Callahan, & Bruce, 2012; Wyatt & Nave, 2017). This periodic variation can be seen in the waviness of the grayscale of Figure 5. While previous research has shown similar waviness in scanning error (distortion) using line plots, this is the first published representation of distortion in flatbed scanned images using a two-dimensional grayscale plot. As is the case for most measurement error, one might expect the scanning error to be normally distributed about the nominal value. However, the waviness shown in the grayscale of Figure 5 suggests a pattern in the error and, therefore, it would not have a normal distribution. Figure 6 shows the distribution of the error of the 22,801 distances between theoretical centroids and corresponding centroids obtained by scanning at 300 dpi resolution.

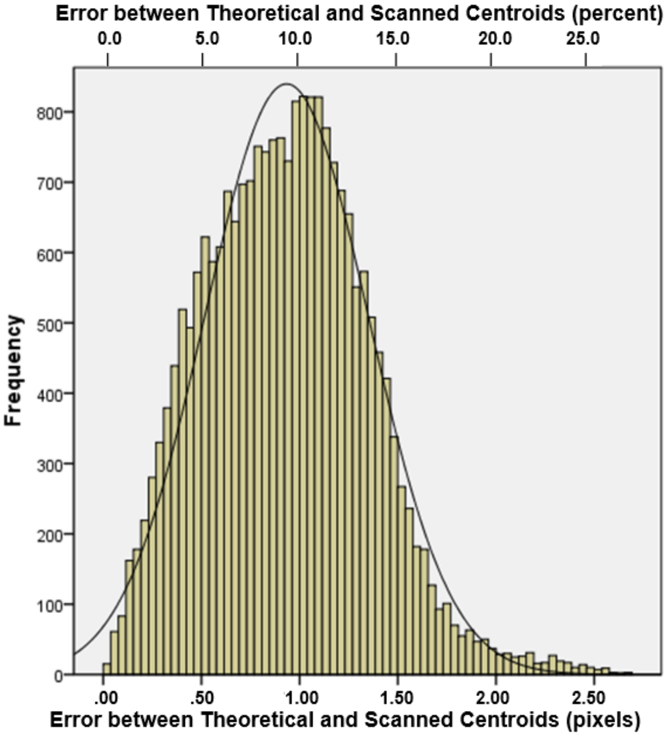

Figure 6. Distribution of distance error between theoretical centroids and centroids obtained by scanning.

The histogram of Figure 6 was generated using IBM SPSS Statistics software, which also was used to overlay a best-fit normal distribution onto the histogram in order to show the obvious deviation from normality of the centroid measurement error. This is supported by applying the software's Kolmogorov-Smirnov test for normality, which rejected the null hypothesis. Therefore, it was assumed that the mechanical movement of the scanner head was the source of error pattern, which drove the distribution to be non-normal. To investigate the above assumption, the x-coordinates and the y-coordinates of the centroids were analyzed independently. It was predicted that the x-coordinates obtained from scanning would show less error relative to the theoretical x-coordinates than that of the error in the y-coordinates. While there will be some unintended mechanical movement (jitter) along the x-direction (parallel to head) during a scan, it was expected that there would be more mechanical jitter along the y-axis (parallel to head travel), since the intended mechanical movement is much greater.

Therefore, it was predicted that the grayscale waviness in Figure 5 would not be present for x-coordinates. Figure 7 shows an 8-bit grayscale representation of the variation of the 22,801 distances between theoretical x-coordinates and the corresponding x-coordinates of centroids obtained by scanning at 300 dpi resolution.

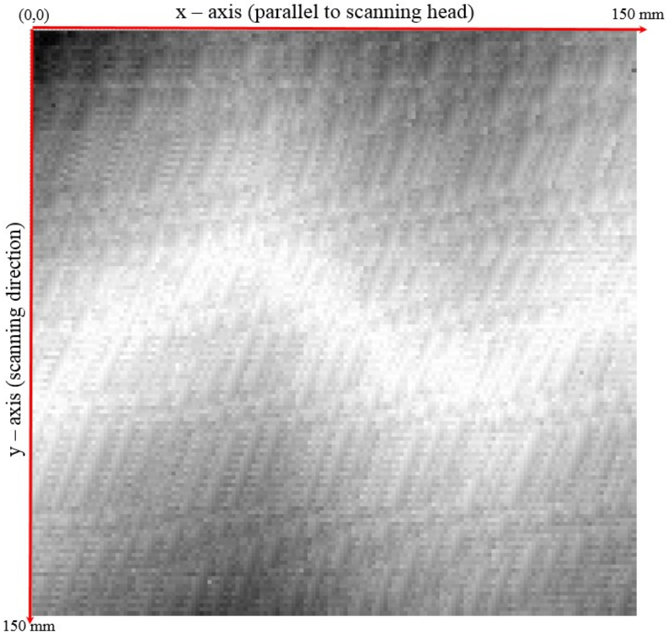

Figure 7. Grayscale map of distances between theoretical x-coordinates of centroids and those obtained by scanning.

Visually, the grayscale map of Figure 7 shows some waviness, but the pattern is much different than the one shown in Figure 5. The waviness in Figure 7 seems to run along the x-axis and has a longer periodicity than the waviness along the y-axis in Figure 5. Quantitatively, the average error represented in Figure 7 is about 4.91%, whereas for Figure 5 it is 7.91%. A smaller error represented in Figure 7 was expected, since it is basically the x-component of the error in Figure 5. It was expected that the y-component of the error represented in Figure 5 would be larger than the x-component, since the y-axis was the intended (gear-driven) direction of motion. Figure 8 shows an 8-bit grayscale representation of the variation of the 22,801 distances between theoretical y-coordinates and the corresponding y-coordinates of centroids obtained by scanning at 300 dpi resolution.

Visually, Figure 8 more closely resembles the pattern in Figure 5 than does Figure 7. The y-component of the error seems to be dominating the error represented in Figure 5. Quantitatively, the average error represented in Figure 7 (x-component) is about 4.91%, whereas for Figure 8 (y-component) it is 5.31%. These two averages are significantly different, as supported by the rejection of the null hypothesis in the Wilcoxon Signed Rank test (via SPSS) of the x-component and y-component error. Therefore, the y-component (Figure 8) of error mostly contributes to the average error in distance between the theoretical centroids and those obtained during scanning.

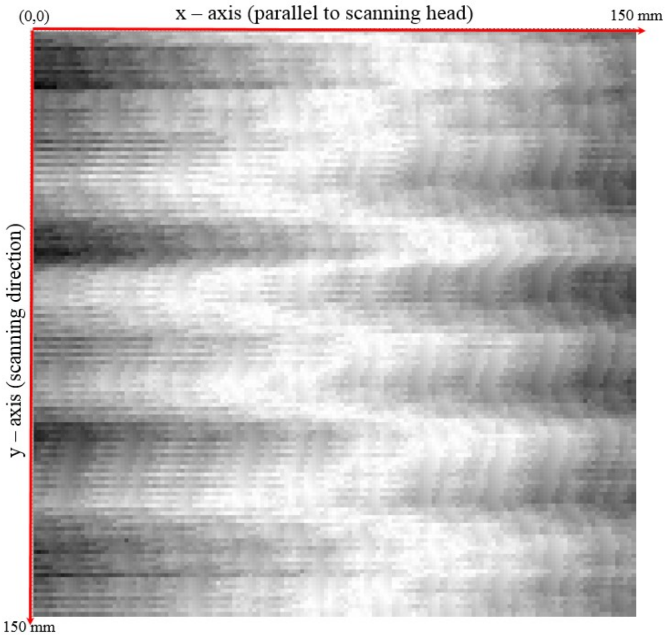

Figure 8. Grayscale map of distances between theoretical y-coordinates of centroids and those obtained by scanning.

The purpose of this paper was to give details of the rotation correction algorithm, how it works in the scanner calibration method, and to give an example of distortion analysis based on the novel grayscale map made possible by the high precision of the rotation correction algorithm. The grayscale distortion map will be a useful tool in future research directed at understanding and minimizing distortion in scanned images. Minimization of distortion could be achieved by scaling the scanned image point-by-point based on the grayscale distortion map. However, the repeatability of these maps must be assessed first. Some examples of questions that have not yet been investigated: Will the distortion pattern change at higher scanning resolutions, in different locations of the scanning bed, and with different brands/models of scanners?

Conclusions

The rotation correction algorithm was demonstrated to be successful over a wide range of target tilt angles and scanner resolutions. This enabled a distortion analysis to be performed at a short 1 mm grid spacing with an average measurement error of less than 1 pixel. It also enabled a novel grayscale map of scanner image distortion to be generated that revealed a periodic error in locating the grid points of the target. This map will be a useful tool for engineers in selecting and quantifying areas of low distortion in order to improve the accuracy of dimensional measurements using flatbed scanners. The periodic error was greater parallel to the scanning direction compared to perpendicular to it. The source of periodic error was attributed to mechanical jitter of the scanning head as it travels, although research is needed to confirm this. It is possible that the periodic error was affected by using a method of centroid calculation based on the simple average of the coordinates of all pixels that met the threshold criteria. Another method, available in the software, uses a weighted average (based on pixel brightness) of the coordinates of all pixels that met the threshold criteria. Perhaps that method would reduce the average measurement error. Future research should also investigate other methods of centroid calculation, such as those employed by Deshpande (2016).

Further research will also be needed to determine how the periodic error changes at higher scanning resolutions and at different locations on the glass bed. It is proposed that the periodic error could be minimized by locally adjusting the x and y direction scale factors at various points in the grid. The adjustments will be guided by examining the grayscale distortion map, which was made possible by the high-precision rotation correction algorithm. No attempt has been made to minimize the execution time of the algorithm, which takes about ten minutes to complete on a common desktop computer. Execution time might be reduced by using fewer measures of the tilt angle, θ, as given by Equations 4-13, while still achieving the required accuracy needed for successful sorting of the centroids into an ordered array.

Acknowledgements

The authors wish to thank Peter A. Jones for working out details in the algorithm that identify the four corner dots of the target.

References

Deshpande, S. (2016). Evaluation of Semi-Automated Target Extraction Methods for Digital Close-Range Photogrammetry. *International Journal of Engineering Research and Innovation, 8*(2).

Elaksher, A. F., & Ali, T. (2018). Geometric Calibration of Low-Cost Flatbed Scanners for Large Scale Mapping Applications. *Modern Instrumentation, 7*, 11-23.

Giannakeas, N., Kalatzis, F., Tsipouras, M. G., & Fotiadis, D. I. (2016). A Generalized Methodology for the Gridding of Microarray Images with Rectangular or Hexagonal Grid. *Signal, Image and Video Processing, 10*(4), 719-728.

Jones, M. P., Callahan, R. N., & Bruce, R. D., (2011). Flow Length Measurement of Injection Molded Spirals using a Flatbed Scanner. *Journal of Industrial Technology*, *27*(1).

Jones, M.P., Callahan, R.N., & Bruce, R.D., (2012). Dimensional Measurement Variation of Scanned Objects Using Flatbed Scanners. *Journal of Technology, Management and Applied Engineering, 28*(2).

Kangasraasio, J., & Hemming, B. (2009). Calibration of a Flatbed Scanner for Traceable Paper Area Measurement. *Measurement Science and Technology, 20*, 1-4.

Kee, C. W., & Ratnam, M. M. (2009). A Simple Approach to Fine Wire Diameter Measurement using a High-Resolution Flatbed Scanner. *The International Journal of Advanced Manufacturing Technology, 40*(7-8), 940-947

Korin, I., Larrainzar, C., & Ipina, J. P. (2008). Crack Length and Stable Crack Extension Measurements from Images Acquired by Means of a Conventional Flatbed Scanner. *Fatigue and Fracture of Engineering Materials and Structures, 31*(10), 876–884.

Miriello, D., & Crisci, G. M. (2006). Image Analysis and Flatbed Scanners. A Visual Procedure in Order to Study the Macro-Porosity of the Archaeological and Historical Mortars. *Journal of Cultural Heritage, 7*, 186-192.

Morris, D., Wang, Z., & Liu, X. (2007). Microarray Subgrid Detection: A Novel Algorithm. *International Journal of Computer Mathematics, 84*(5), 669-678.

Ng, T. W. (2008). Light-Emitting-Diode Inspection using a Flatbed Scanner. *Optical Engineering: The Journal of the Society of Photo-Optical Instrumentation Engineers, 47*(10), 103602.

NIH, (2018). ImageJ. Retrieved July 17, 2018, from https://imagej.nih.gov/ij/.

NIST, (2007). Fiftieth Anniversary of First Digital Image Marked. Retrieved July 17, 2018 from https://www.nist.gov/news-events/news/2007/05/fiftieth-anniversary-first-digital-image-marked

Paliwal, J., Borhan, M. S., & Jayas, D. S. (2004). Classification of Cereal Grains using a Flatbed Scanner. *Canadian Biosystems Engineering, 46*, 1-4.

Poliakow, E. V., Poliakov, V. V., Fedotova, L. A., & Tsvetkov, M. K. (2007). High-Precision Measuring Scale Rulers for Flatbed Scanners. In M. K. Tsvetkov, L. G. Filipov, M. S. Dimitrijevic, & L. C Popovic (Eds). *Astronomy and space science* (pp 356-368). Sofia: Heron Press Ltd.

Shao, G. F., Yang, F., Zhang, Q., Zhou, Q. F., & Luo, L. K. (2013). Using the Maximum Between-Class Variance for Automatic Gridding of cDNA Microarray Images. *IEEE/ACM Transactions on Computational Biology and Bioinformatics, 10*(1), 181-192.

Van Dalen, G. (2004). Determination of the Size Distribution and Percentage of Broken Kernels of Rice using Flatbed Scanning and Image Analysis. *Food Research International, 37*(1), 51-57.

Wang, Z., Zeng, Q., Wang, L., Li, K., Xu, S., & Yao, Y. (2016). Characterizing Frost Damages of Concrete with Flatbed Scanner. *Construction and Building Materials*, *102*, 872–883.

Weyori, B. A., & Boateng, K. O. (2013). Dynamic Intelligent Mean Filter for Impulse Noise Suppression in 2D Images. *International Journal of Modern Engineering, 13*(2).

Wyatt, M., & Nave, G. (2017). Evaluation of Resolution and Periodic Errors of a Flatbed Scanner Used for Digitizing Spectroscopic Photographic Plates. *Applied Optics, 56*, 3744-3749.

Zalocha, D., & Kasperkiewicz, J. (2005). Estimation of the Structure of Air Entrained Concrete using a Flatbed Scanner. *Cement and Concrete Research, 35*(10), 2041-2046.

Zheng, G., Ou, X., & Yang, C. (2014). 0.5 Gigapixel Microscopy using a Flatbed Scanner. *Biomedical optics express, 5*(1), 1-8.

Biographies

MARTIN P. JONES is an associate professor of technology and construction management at Missouri State University. He earned his BS degree in physics in 1981 from the University of Maryland Baltimore County, and MS and PhD degree in materials science and engineering in 1984 and 1987, respectively, from the Johns Hopkins University. Dr. Jones is currently teaching at Missouri State University. His research interests include scanner technology, nondestructive evaluation, manufacturing processes, and quality assurance. Dr. Jones may be reached at MartinJones@MissouriState.edu

KEVIN M. HUBBARD is an assistant professor of technology and construction management at Missouri State University. He earned his BS degree in aerospace engineering, and MS and PhD degrees in engineering management from the University of Missouri–Rolla in 1991, 1993, and 1996, respectively. Dr. Hubbard is currently teaching at Missouri State University. His research interests include automation and device control, manufacturing systems, device design, and process optimization. Dr. Hubbard may be reached at KHubbard@MissouriState.edu

NEBIL BUYURGAN is a professor of technology and construction management at Missouri State University. He earned his BS degree in industrial engineering in 1998 from Istanbul Technical University, Turkey, and MS and PhD degrees in engineering management in 2000 and 2004, respectively, from the University of Missouri–Rolla. Dr. Buyurgan is currently teaching at Missouri State University. His research interests include optimization of logistics operations in manufacturing, healthcare, military and retail, and supply chain management. Dr. Buyurgan may be reached at NebilBuyurgan@MissouriState.edu

A NOVEL CURRICULUM FOR SOLAR AND WIND ENERGY SYSTEMS IN AN ENGINEERING TECHNOLOGY PROGRAM

Reg Pecen, Sam Houston State University; Faruk Yildiz, Sam Houston State University; Kali M. Johnson, Sam Houston State University; Andres Aguirre, Sam Houston State University; Ulan Dakeev, Texas A&M University—Kingsville

Abstract

Introduction of renewable energy and smart grid applications to an existing conventional electrical power systems curriculum in the Engineering Technology Department at Sam Houston State University has positively impacted students, faculty, and the university community and promoted the adoption of sustainable, reliable, flexible, and better-quality energy technologies. In this paper, the authors present the development of a novel power systems curriculum with an emphasis on renewable energy and smart grid technologies for a new junior-level power and machinery class in the Electronics and Computer Engineering Technology (ECET) BS degree program. Teaching modules covered include: 1) stand-alone home energy production; 2) grid-tied home energy production using an inverter; and, 3) a large-scale energy storage system for the implementation of a basic smart grid. The results of the new curriculum are very promising in terms of increasing student interest and enthusiasm for modern electrical power systems that are integrated into a smart grid through a state-of-the-art data acquisition and instrumentation system. One of the major industrial partners and employers of ECET graduates, Quanta Services Inc., provided strong support for the department and the program and expressed hope that universities would provide companies like theirs with graduates having up-to-date competencies in next-generation electrical transmission, distribution, and procurement areas.

Introduction

Fossil fuel power plants have been major sources of electrical power for the conventional grid; however, aging infrastructure, coupled with a rising demand for reliable and stable electricity, and environmental concerns regarding the industry's carbon footprint have made it crucial for the grid to transform its existing and outdated infrastructure into a next-generation smart grid enhanced with distributed generation (DG). DG is the electricity generated from multiple renewable energy resources, such as wind, solar, hydrogen fuel cell, micro-combined heat power generators, small-scale micro-hydro turbine generators, and diesel power units (Celeita, Justo, Mwasilu, Lee, & Jung, 2013; El-Khattam, & Salama, 2004; Celeita, Hernandez, Ramos, Penafiel, Rangel, & Bernal, 2016; Cardenas, Gemoets, Ablanedo Rosas, & Sarfi, 2014; Uludag, Lui, Ren, & Nahrstedt, 2016).

A smart grid is an intelligent, adaptive-balancing, self-monitoring power grid that accepts any source of fuel and transforms it into a consumer's end use with minimum human intervention and maximum reliability (Cardenas et al., 2014; Uludag et al., 2016; Luo, Shi, & Tu, 2014; Wadghule, 2013). In addition, the smart grid allows for the optimization of renewable energy use and minimizes the cumulative carbon footprint. Synchronization of all operating power plants introduces new challenges, due to their various infrastructure and operating characteristics. DG is an emerging approach to providing electric power in the heart of the power system, but this approach depends on the installation and operation of a portfolio of small-sized, compact, and clean electric power generating units at or near electrical loads (Yong, Ramachandaramurthy, Tan, & Mithulananthan, 2015; Sandeep & Saurabh, 2018). The DG of electricity integrates with renewable energy technologies such as photovoltaic (PV) arrays, wind turbines, micro-hydro turbines, tidal units, biogas systems, and hydrogen fuel cell units (Sandeep & Saurabh, 2018).

The implementation of DG sources on a conventional grid may result in many advantages, such as providing high efficiency and reducing the carbon footprint, reducing transmission and distribution losses, supporting the local grid, and enhancing system stability. However, application of individual DG may also cause as many additional issues as it may solve, and there are research problems to be solved in the grid-tied operation of conventional and DG fields (Sandeep & Saurabh, 2018; Khodayar & Wu, 2015; Jerin, Prabaharan, Kumar, Palanisamy, Umashankar, & Siano, 2018). When the grid includes DG sources, the term "smart grid" becomes an umbrella to refer to new technologies that address today's electrical grid challenges associated with grid reliability and reactive maintenance, smooth integration of renewables, and disturbance detection that may arise from any section of the grid, from an inverter failure from a large PV farm to a tree branch short circuit of the alternating current (AC) transmission line on the grid (Khodayar & Wu, 2015;

Jerin et al., 2018; Fang, Misra, Xue, & Yang, 2012). A combination of smart micro grids is expected to modify the conventional electrical power system, thereby enhancing reliability, accessibility, flexibility and power quality (Sandeep & Saurabh, 2018; Khodayar & Wu, 2015; Jerin et al., 2018; Fang, Misra, Xue, & Yang, 2012).

The increasing importance of renewable energy sources in smart grid technologies also requires additional workforce and engineers, in many cases beginning with undergraduate students. This will require learning what a smart grid is and how it functions, as well as the integration of major renewable energy sources such as solar and wind energy systems to the existing grid (Fang et al., 2012; Justo, Mwasilu, Lee, & Jung, 2013; Jennings, 2009). An example of a program, which would coincide with courses such as solar and wind energy systems, is already being implemented into undergraduate curricula at the University of Alaska Anchorage (Belu & Cioca, 2016). For a student to gain a solid understanding of the smart grid, a multidisciplinary course covering various aspects is essential (Justo et al., 2013; Jennings, 2009; Belu & Cioca, 2016; Dumitru & Gligor, 2014). Another undergraduate junior-level course on smart grids that covers grid fundamentals, system structure, major components, analysis, system operation and management, has been offered successfully (Jennings, 2009; Belu & Cioca, 2016; Dumitru & Gligor, 2014).

It is imperative that future engineers and technical managers have up-to-date knowledge of the electrical grid system that they will be working on. The curriculum covered at three institutions that focus on power electronics and specifically the smart grid, benefits everyone involved in the modern electrical power industry (Jennings, 2009; Belu & Cioca, 2016). In this paper, the authors report results of a summer faculty and student team research and development award that was funded for developing a new curriculum to strengthen the electrical power class as requested by industrial advisory board members from electrical power industries. The curriculum included development of the following teaching modules in smart grid technologies: 1) stand-alone home energy production; 2) grid-tied home energy production using an inverter; and, 3) a large-scale energy storage for the implementation of a basic smart grid using a commercially available state-of-the-art power system data acquisition module.

Smart Grid Project Implementation

A smart grid technology training system developed by Festo Corporation was used in this study (Festo, Home, 2017; Festo, Smart, 2017). Undergraduate research students established a test bench with a PV panel emulator for the implementation of standalone and grid-tied home energy production (HEP); Figure 1 shows the Festo power systems training workbench. Students also established the same system by actual PV modules connected to the grid-tied HEP instrumentation system. This scheme provided understanding of the necessary fundamentals for further inclusion of multiple energy generation sources developed for a small-scale smart grid system during various operating times and demand (Festo, Smart, 2017; Reka & Dragicevic, 2018; Qadrdan, Jenkins, & Wu, 2018). The test bench used in this study was a standalone PV system that included a solar panel emulator, a battery, a DC-to-DC converter, a boost chopper, an LC filter, and a single-phase PWM inverter. Figure 2 shows the low-voltage data acquisition and control (LVDAC) instrumentation module allowed for real time measurement and monitoring of voltage, current, power, power factor, phase shift, and other meter settings. The LVDAC module is an effective tool for precise data acquisition and analysis. Various controls within each function of the LVDAC module and the four-quadrant dynamometer are available, such as a solar power inverter, solar panel emulator, HEP window, phasor analyzer, oscilloscope, etc. The Smart Grid Technologies Training System in Figure 1 includes the following modules:

- A resistive load bank used to simulate loads at the user end of an energy system similar to resistive loads at residential buildings.
- A data acquisition and control interface (DACI) for the monitoring of various types of data in an experiment. It may also be used to control aspects of an experiment when used with the LVDAC software.
- A low-frequency transformer for isolation between the DC and AC sides of a power system, when galvanic isolation is required and the DC-to-DC converter is not used and to achieve the voltage measurements necessary for proper operation.
- IGBT chopper/inverter to boost the DC voltage to the necessary DC bus voltage for inversion to AC. This can also be used as a buck chopper, which reduces voltage to meet the DC bus needs. This module allows electrical power flow in either direction.
- Filtering inductors/capacitors to smooth out the current waveform on the AC side of the system. The capacitors improve power factor and keep constant voltage.
- AC power network interface to provide AC power from the inverter that can be used to operate a load, or as a means to inject power back to the AC power network.
- A four-quadrant dynamometer power supply with many functions available to generate power when simulating PVs and other renewable resources.

- A lead-acid battery pack to serve as a power source as well as a bank for power storage when being implemented in a smart grid.
- A power supply to provide 3-phase power and an AC voltage of 24V to the system units.

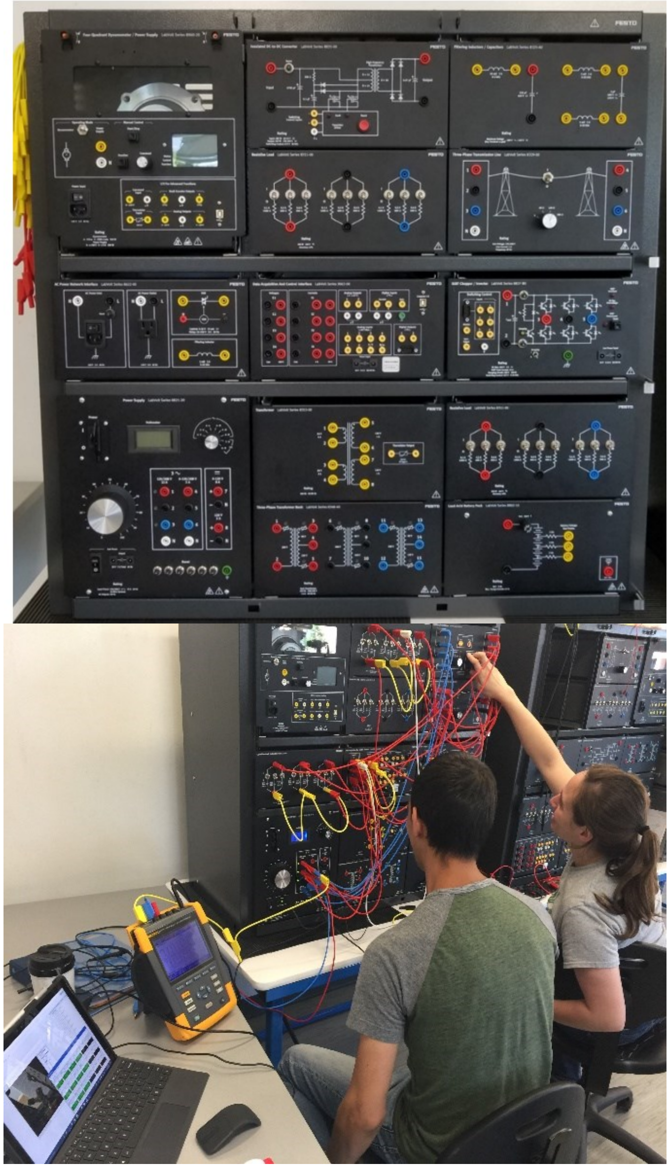

Figure 1. FESTO Smart Grid Technology Training System and students working on the smart grid curriculum. Reprinted with permission.

Project 1: Standalone Home Energy Production (HEP)

The standalone HEP project demonstrated the power flow from the source to the AC load, with the excess power charging the battery. Figure 3 shows how the students initially set up a battery-powered circuit connected to the boost chopper, single-phase PWM inverter, filtering inductors, and a resistive load. This enabled students to calculate the power efficiency of the system (86.6%) using a measured load power of 109.8W and a battery power of 126.8W. The load power was increased to demonstrate its effects on the voltage values from the DC bus, load, battery, and duty cycle. Figure 4 shows how the load voltage decreased and the load current increased as the load power increased. DC bus voltage and battery voltage remained relatively constant. The duty cycle increased from 77% to 79% as load power increased. Power generation was switched from the battery to a solar panel emulator implemented by the Festo four-quadrant dynamometer. The array was set up to have seven PV panels in series and thirty-eight PV panels in parallel. This setup produced a voltage of 67.9V, a current of 4.0A, and a power rating of about 271W.

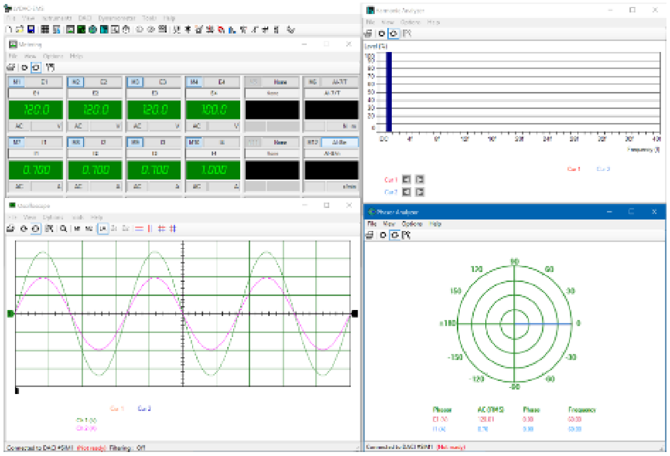

Figure 2. Example of the LVDAC-EMS software interface used in the project. Reprinted with permission.

Figure 5 illustrates how excess power can be utilized to recharge the battery bank while simultaneously operating a load. When the battery is not being recharged, the PV emulator fully supplies power to the load under high solar irradiance. When solar irradiance drops below about 810 W/m^2, the battery is used to supplement power that is needed by the load.

Project 2: Grid-Tied HEP Using a Solar Power Inverter without a DC-to-DC Converter

Figure 6 shows the small-scale generation of electrical power from solar PV panels in which the active and reactive power flow direction was tested under different polarities of each respective current command and their consequential effects on power to and from the grid. Figures 7(a)-(d) outline the power readings when the active and reactive current commands were set with different polarities in the LVDAC

HEP and the single-phase grid-tied inverter function was used. Figures 7(a) and 7(d) show that, when the active current command is positive, active power is injected into the local AC power network. Figures 7(b) and 7(c) show that the active current command is negative when power is withdrawn from the local AC power network into the single-phase grid-tied inverter. Power is converted to DC voltage and charges the battery. When the reactive current command is positive, reactive power is injected into the single-phase grid-tied inverter. When the reactive current command is negative, reactive power is injected into the local AC power network. The next part of this project demonstrated that a low-frequency transformer could be used to isolate the DC side from the AC side, if this were required in a real-world application. The transformer not only provides isolation from the DC and AC sides of the system but allows for a lower DC input voltage that is stepped up on the AC side to meet local AC power network requirements. Figure 8 shows that the solar irradiance of the PV emulator was increased in intervals of 100 W/m^2 from an initial value of 300 W/m^2 to 1000 W/m^2. The DC voltage remained constant in this situation, and the output power continued to increase. This was a result of the transformer being used on the AC side of the system, adjusting the output voltage to that of the AC power network and the MPPT keeping the active current command set to deliver the maximum power to the network.

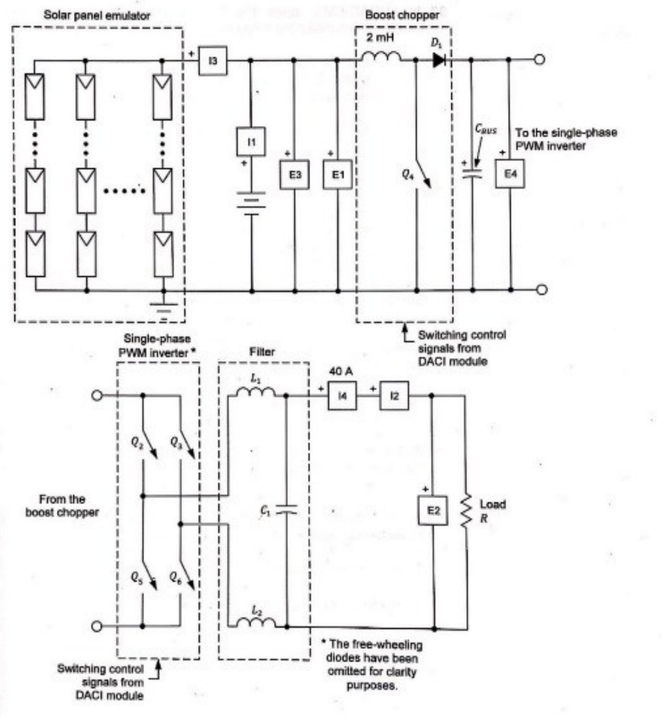

Figure 3. Standalone energy production circuit diagram. Reprinted with permission.

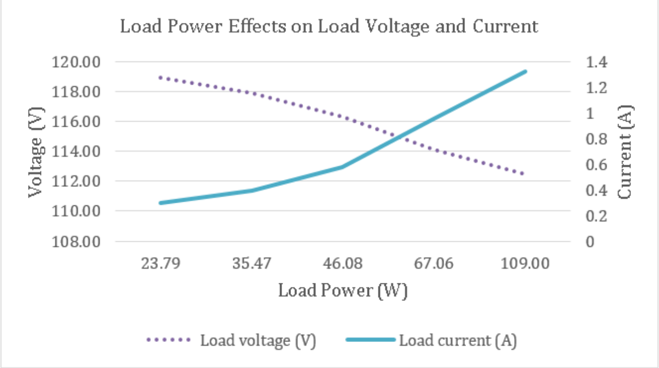

Figure 4. Load current and voltage as load increases.

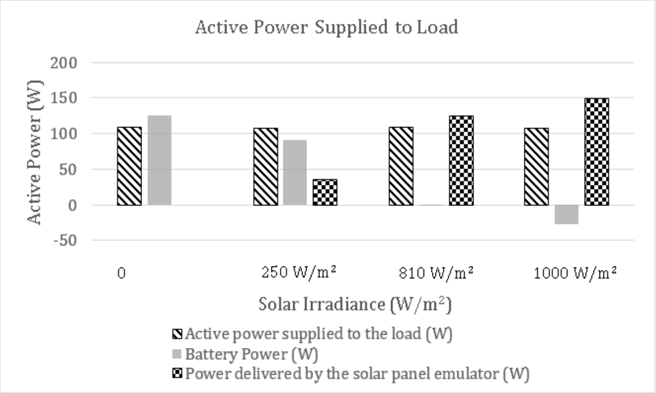

Figure 5. Active power supplied to load with supplemental battery charging.

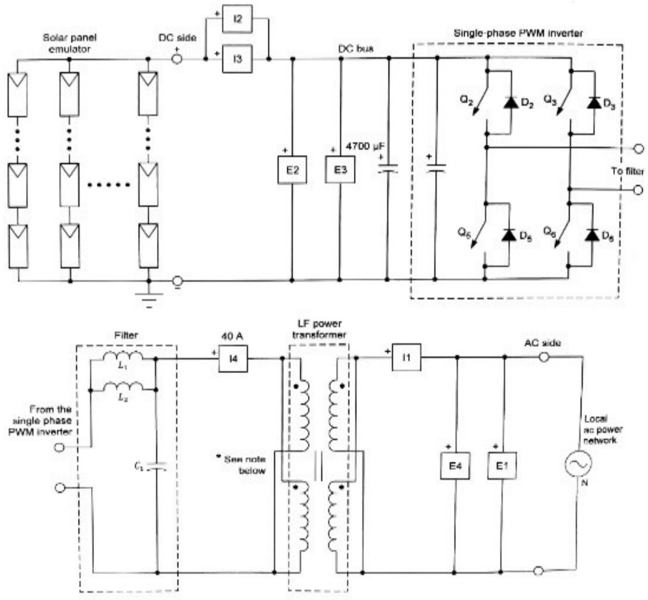

Figure 6. Implementing a grid-tied HEP by PV panels and a low-frequency transformer. Reprinted with permission.

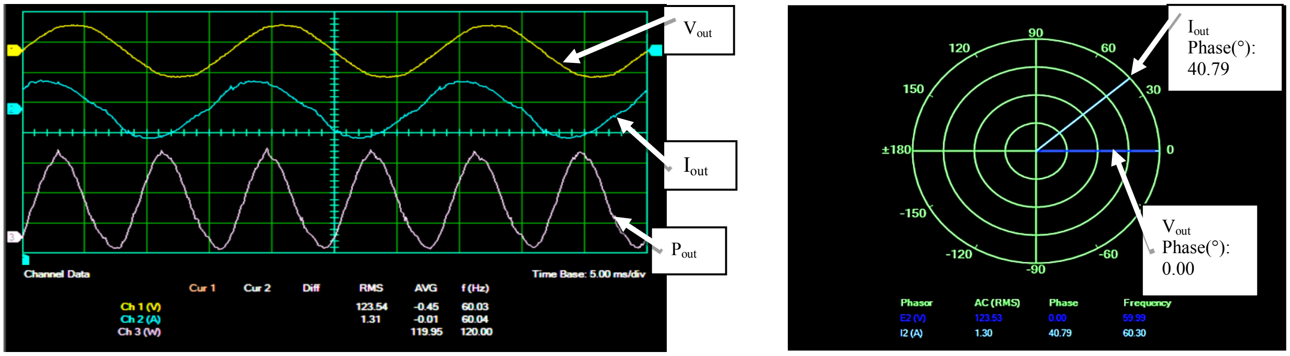

Channel Data Time Base: 5.00 ms/div

	Cur 1	Cur 2	Diff	RMS	AVG	f (Hz)
Ch 1 (V)				123.54	-0.45	60.03
Ch 2 (A)				1.31	-0.01	60.04
Ch 3 (W)					119.95	120.00

Phasor	AC (RMS)	Phase	Frequency
E2 (V)	123.53	0.00	59.99
I2 (A)	1.30	40.79	60.30

(a) Load power with active and reactive command currents of +1A.

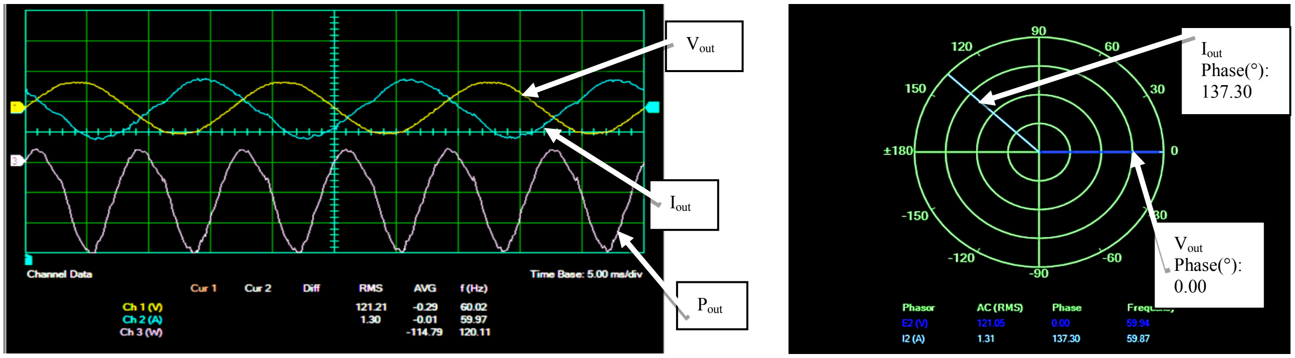

Channel Data Time Base: 5.00 ms/div

	Cur 1	Cur 2	Diff	RMS	AVG	f (Hz)
Ch 1 (V)				121.21	-0.29	60.02
Ch 2 (A)				1.30	-0.01	59.97
Ch 3 (W)					-114.79	120.11

Phasor	AC (RMS)	Phase	Frequency
E2 (V)	121.05	0.00	59.94
I2 (A)	1.31	137.30	59.87

(b) Load power with active and reactive command currents of -1A and +1A.

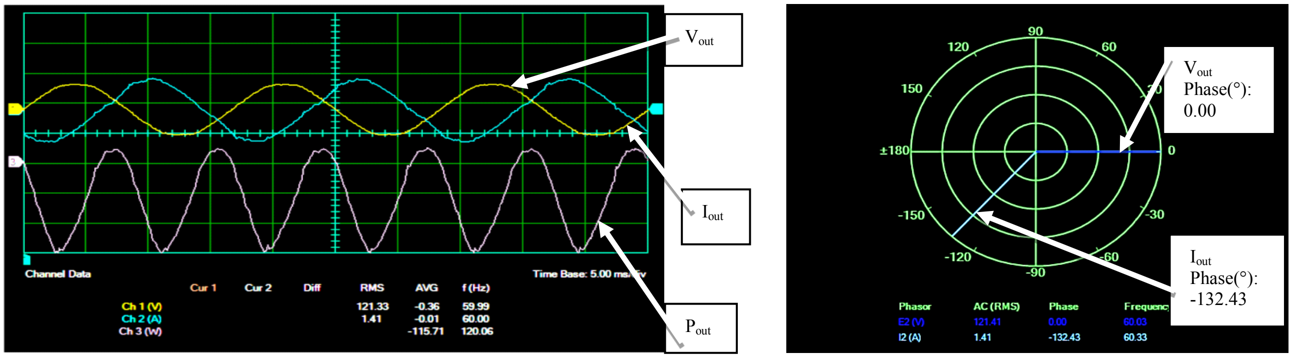

Channel Data Time Base: 5.00 ms/div

	Cur 1	Cur 2	Diff	RMS	AVG	f (Hz)
Ch 1 (V)				121.33	-0.36	59.99
Ch 2 (A)				1.41	-0.01	60.00
Ch 3 (W)					-115.71	120.06

Phasor	AC (RMS)	Phase	Frequenc
E2 (V)	121.41	0.00	60.03
I2 (A)	1.41	-132.43	60.33

(c) Load power with active and reactive command currents of -1A and -1A.

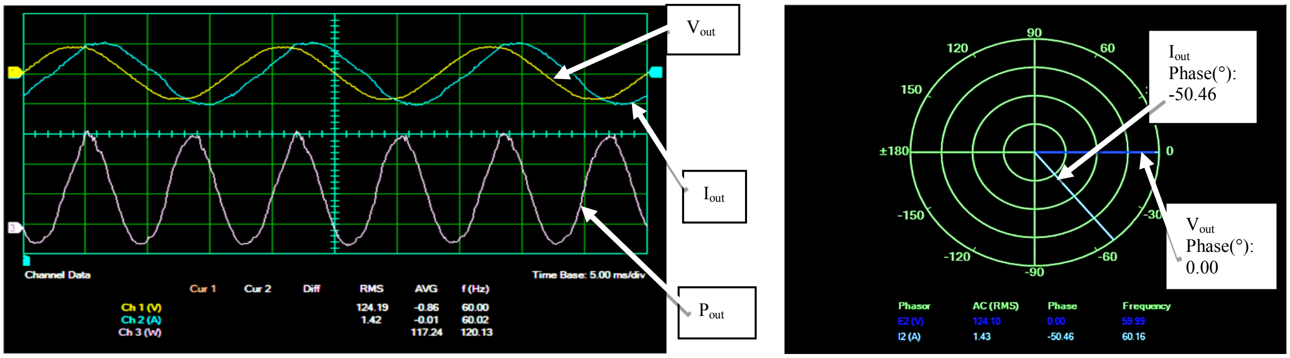

Channel Data Time Base: 5.00 ms/div

	Cur 1	Cur 2	Diff	RMS	AVG	f (Hz)
Ch 1 (V)				124.19	-0.86	60.00
Ch 2 (A)				1.42	-0.01	60.02
Ch 3 (W)					117.24	120.13

Phasor	AC (RMS)	Phase	Frequency
E2 (V)	124.10	0.00	59.99
I2 (A)	1.43	-50.46	60.16

(d) Load power with active and reactive command currents of +1A and -1A.

Figure 8. Input/output power and output current as a function of solar irradiance.

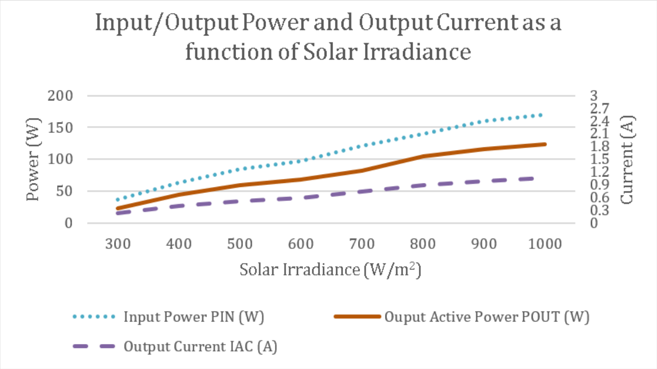

Figure 8. Input/output power and output current as a function of solar irradiance.

Figure 8 further shows that the input power is greater than the output power. This was due to losses through the inverter and filtering inductors. As the irradiance level increased, the input power, output power, and output current all steadily increased as well. Figure 9 (left) shows the variables $V_{in,DC}$, $I_{out,AC}$, and $V_{out,AC}$ at a solar irradiance level of 500 W/m^2, and Figure 9 (right) shows measurements at a solar irradiance level of 1000 W/m^2. While the $V_{out,AC}$ remained constant, the MPPT varied the active current command with the use of the P&O algorithm to determine and operate the PV emulator at the maximum power point. Figure 9 (right) shows that, before balancing out, the amplitude of the $I_{out, AC}$ line visibly increases and decreases while attempting to determine the operating point.

Project 3: Large-Scale Energy Storage to Implement a Smart Grid with Electrical Vehicles (EVs)

Widespread use of grid-tied inverters and batteries allows for additional storage of large amounts of energy that can be fed to the AC grid when a demand exists. One of the best practices of this project is for plug-in vehicles (PEVs) and plug-in hybrid electric vehicles (PHEVs) that will enable large-scale energy storage in a smart grid system (Qadrdan, Jenkins, & Wu, 2018; Zahedi, 2018). In this experiment, the authors studied a set of daytime and nighttime cycles, measuring the power demand and home energy consumption from the grid, both with and without the use of energy storage. The circuit diagram in Figure 10 shows how daytime and nighttime cycles were simulated with the use of resistive loads. Daytime demands are higher than nighttime; therefore, to demonstrate this fact, all of the parallel-connected resistive loads were switched on to achieve a low-resistance load of 57 ohms. After five minutes for the daytime cycle, a nighttime demand was simulated by increasing the resistance to 240 ohms. This case can be updated further when charging PEVs and PHEVs at night. Table 1 shows that, without energy storage, the nighttime demand for power was about four times less than that of the daytime demand.

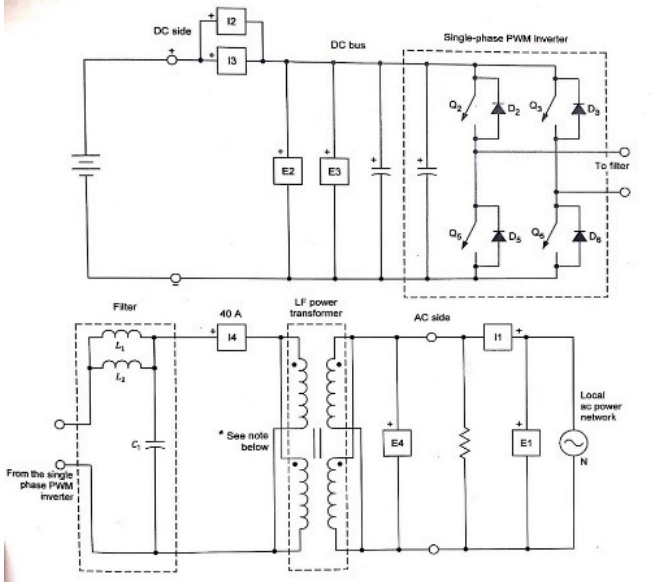

Figure 10. Large-scale energy storage circuit diagram. Reprinted with permission.

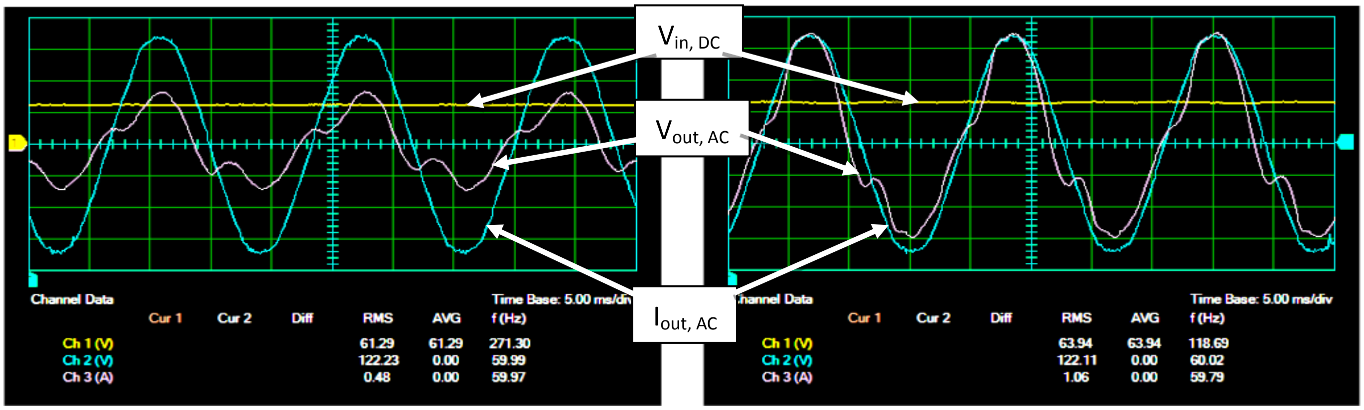

```
Channel Data                                           Time Base: 5.00 ms/di
        Cur 1    Cur 2    Diff    RMS      AVG      f (Hz)
Ch 1 (V)                          61.29    61.29    271.30
Ch 2 (V)                          122.23   0.00     59.99
Ch 3 (A)                          0.48     0.00     59.97
```

```
hannel Data                                            Time Base: 5.00 ms/div
        Cur 1    Cur 2    Diff    RMS      AVG      f (Hz)
Ch 1 (V)                          63.94    63.94    118.69
Ch 2 (V)                          122.11   0.00     60.02
Ch 3 (A)                          1.06     0.00     59.79
```

Figure 9. Oscilloscope measurements at solar irradiance levels of 500 W/m^2 and 1000 W/m^2.

Table 1. Daytime/nighttime cycle power measurements without energy storage.

Power and energy measurements	Daytime	Nighttime
Home power demand (active power at the AC side of the single-phase grid-tied inverter), P_{grid} (W)	257.9	67.83
Battery power (power at the DC side of the single-phase grid-tied inverter), $P_{BATT.}$ (W)	3.1	3.1
Home energy consumption (energy which the grid supplied to the home during the simulated daytime/nighttime cycle), E_{Grid} (Wh)	30.1	

Table 2 shows measurements of power demand and consumption from the grid was then explored for times when an energy storage device is used, instead of relying on immediate power generation from the grid at the time of demand. In this part of the procedure, the battery was charged by the grid during the nighttime cycle when the power demand from the grid was lower. The charged battery then supplied power to the grid during the daytime cycle to lower the power demand from the generation sources.

Table 2. Daytime/nighttime cycle power measurements with energy storage.

Power and energy measurements	Daytime	Nighttime
Home power demand (active power at the AC side of the single-phase grid-tied inverter), P_{grid} (W)	192.7	192.4
Battery power (power at the DC side of the single-phase grid-tied inverter), $P_{BATT.}$ (W)	87.8	-89.1
Energy exchange at the battery after the simulated daytime interval), $E_{BATT.,DAY}$ (Wh)	7.8	
Home energy consumption (energy which the grid supplied to the home during the simulated daytime/nighttime cycle), E_{Grid} (Wh)	44.52	
Energy exchange at the battery after the simulated daytime/nighttime interval, $E_{BATT.,DAY/NIGHT}$ (Wh)	0.7	

Learning Outcomes of the Electrical Power and Machinery Course

The students were expected to gain foundational knowledge of standalone and grid-tied energy production using power system operation, battery storage, and energy conversion techniques in conventional and alternative energy systems. Through the course of the laboratory projects, students became familiar with the components used in grid-tied and standalone energy systems, such as a boost chopper, single-phase inverter/rectifier, and transformer for use of voltage isolation, insulated DC-to-DC converter, DACI, and the LVDAC system software by Festo. Upon completion of the course, students were expected to achieve the following outcomes that would also enhance the program's data-collection and assessment efforts aligned with ABET-ETAC criteria:

- Apply the theory of electrical machines—motors-generators-transformers—to the practical industrial settings with appropriate drives and controls.
- Learn the theory of single-phase and three-phase electrical power, stationary and rotating electrical machines operating on DC/AC, and their relevant control systems.
- Establish the concepts of electrical power production, transmission, application, and control relating to industrial and commercial settings.
- Learn fundamentals of the National Electric Code and Electrical Safety Rules.
- Apply creativity in the design of components and systems based on specified requirements and known design techniques.
- Design and carry out experiments and tests, analyze and interpret data, and make iterative improvements by using safe and technically correct laboratory methods.
- Collaborate with each other in laboratory settings to work effectively in teams.

Conclusions

An undergraduate summer research project at SHSU produced an effective teaching curriculum with laboratory projects in the area of smart grid electrical power systems. A new junior-level class on electrical power and machinery would be offered in the 2018-19 academic year with the laboratories described in this paper. The teaching modules covered were: 1) stand-alone home energy production; 2) grid-tied home energy production using an inverter; and, 3) large-scale energy storage for the implementation of a basic smart grid. The results of the new curriculum were very promising in terms of increasing student interest and enthusiasm about modern electrical power systems integrated into a smart grid through a state-of-the art data acquisition and instrumentation system. The authors also reported the work of undergraduate students on smart grids to investigate and implement self-healing from power quality issues, providing efficient energy management, incorporating smart metering, and integration of distributed power generation, renewable energy resources including solar, wind, and hydrogen fuel cell and power storage units.

Acknowledgments

The SHSU Office of Research Administration is greatly appreciated for providing summer funding, enhancing undergraduate research experiences and creative activities, and faculty and student team awards. The authors would also like to thank Philippe Ranger from Festo Didactic Inc., for his valuable guidance and delivering informative instructions on the smart grid electrical power system equipment used in the project.

References

Belu, R. G., & Cioca, L. I. (2016). Development and implementation of an undergraduate course on smart grids. *Proceedings of the 123rd ASEE Annual Conference & Exposition*. Washington, DC: ASEE.

Cardenas, J. A., Gemoets, L., Ablanedo Rosas, J. H., & Sarfi, R. (2014). A literature survey on smart grid distribution: An analytical approach. *Journal of Cleaner Production, 65*(C), 202-216.

Celeita, D., Justo J. J., Mwasilu, F., Lee, J., & Jung, J. W. (2013) AC-microgrids versus DC-microgrids with distributed energy resources: A review. *Renewable Sustainable Energy Review*, *24*, 387-405.

Celeita, D., Hernandez, M., Ramos, G., Penafiel N., Rangel, M., & Bernal, J. D. (2016). Implementation of an educational real-time platform for relaying automation on smart grids. *Electrical Power System Research, 130*(12), 156-166. Retrieved from http://dx.doi.org/10.1016/j.epsr.2015.09.003

Dumitru, C., & Gligor, A. (2014). Designing of a renewable energy training program for engineering education. *Procedia Technology*, *12*, 753-758.

El-Khattam, W., & Salama, M. A. (2004). Distributed generation technologies, definitions and benefits. *Journal of Electric Power Systems Research, 71* (2), 119-128.

Fang, X., Misra, S., Xue, G., & Yang, D. (2012). Smart grid –The new and improved power grid: A survey. *IEEE Communications Surveys & Tutorials*, *14*(4), 944-980. Retrieved from https://ieeexplore.ieee.org/document/6099519/

Festo Didactic Inc. (2017). *Home energy production*. Québec, Canada: Festo Didactic Ltee/Ltd.

Festo Didactic Inc. (2017). *Smart grid technologies training system-Unit 8010-C, Festo Didactic Inc.* Eatontown, NJ: Festo.

Jennings, P. (2009). New directions in renewable energy education. *Renewable Energy*, *34*(2), 435-439. Retrieved from https://doi.org/10.1016/j.renene.2008.05.005

Jerin, A. R. A., Natarajan, ., Kumar, N. M., Kaliannan, P., Subramaniam, U., Pierluigi, . (2018). Smart grid and power quality issues. In F. Hina, N. Parbaharan, K. Akhtar, M. Saad, & J. Jackson (Eds.). *Hybrid-Renewable Energy Systems in Microgrids* (pp. 195-202). Philadelphia: Woodhead Publishing.

Justo, J. J., Mwasilu, F., Lee, J., & Jung, J. W. (2013). AC-microgrids versus DC-microgrids with distributed energy resources: A review. *Renewable and Sustainable Energy*, *24*(C), 387-405.

Khodayar, M. E., & Wu, H. (2015). Demand forecasting in the smart grid paradigm: Features and challenges. *The Electricity Journal, 28*(6), 51-62. Retrieved from https://www.sciencedirect.com/science/article/pii/S1040619015001268

Luo, Y., Shi, L., & Tu, G. (2014). Optimal sizing & control strategy of isolated grid with wind power & energy storage system. *Energy Conversion Management, 80,* 407-415.

Qadrdan, M., Jenkins, N., & Wu, J. (2018). Smart grid and energy storage. In S. A. Kalogirou (Ed.), *McEvoy's handbook of photovoltaics* (pp. 915-928). Atlanta, GA: Elsevier Academic Press. Retrieved from https://doi.org/10.1016/B978-0-12-809921-6.00025-2

Reka Sofana, S. and Dragicevic, T. (2018). Future effectual role of energy delivery: A comprehensive review of Internet of Things and smart grid. *Renewable and Sustainable Energy Reviews, 91*, 90-108. Retrieved from https://doi.org/10.1016/j.rser.2018.03.089

Sandeep, K., & Saurabh, C. (2018). Smart operations of smart grids integrated with distributed generation: *Journal of Renewable & Sustainable Energy Review, 81*, 524-535.

Uludag, S., Lui, K. S., Ren, W., & Nahrstedt, K. (2016). Secure, scalable data collection with time minimization in the smart grid. *IEEE Transactions on Smart Grid, 7*(1), 43-54.

Wadghule, T. M. (2013). A review of plug-in hybrid electric vehicles as new storage & transportation system for smart grid. *International Journal of Engineering Research & Technology, 2*(3), 1-7.

Yong, J. Y., Ramachandaramurthy, V. K., Tan, K. M., & Mithulananthan, N. (2015). A review on the state-of-the-art technologies of electric vehicle, its impacts and prospects. *Renewable Sustainable Energy Review, 49*, 365-385. Retrieved from https://doi.org/10.1016/j.rser.2015.04.130

Zahedi, A. (2018). Smart grids and the role of the electric vehicle to support the electricity grid during peak demand. In L. A. Lamont & A. Sayigh (Eds.), *Application of Smart Grid Technologies* (pp. 415-428). Elsevier Academic Press. Retrieved from https://doi.org/10.1016/B978-0-12-803128-5.00013-1

Biographies

REG PECEN is a Quanta Endowed Professor of Engineering Technology in the College of Science and Engineering Technology at Sam Houston State University. Dr. Pecen served as president and professor at the North American University at Stafford from July 1, 2012, to December 12, 2016. Dr. Pecen was formerly a professor and program chairs of EET and graduate programs in the Department of Technology at the University of Northern Iowa between 1998 and 2012. Dr. Pecen updated the former Electromechanical Systems program to EET and secured ABET-ETAC accreditation. He served as chair, chair-elect, and past chair of the Energy Conversion & Conservation Division of the American Society of Engineering Education during 2011-2013. Dr. Pecen is a senior member of IEEE, and member of ASEE and the Tau Beta Pi-National Honor Society. Dr. Pecen may be reached at regpecen@shsu.edu

FARUK YILDIZ is an associate professor and department chair of engineering technology at Sam Houston State University. His primary teaching areas include electronics, computer-aided design, and alternative energy systems. His research interests include low-power energy harvesting systems, renewable energy technologies, and education. Dr. Yildiz may be reached at fxy001@shsu.edu

KALI M. JOHNSON is a senior majoring in electronics and computer engineering technology in the Department of Engineering Technology at SHSU. She may be reached at kmj059@shsu.edu

ANDRES AGUIRRE is a senior majoring in electronics and computer engineering technology in the Department of Engineering Technology at SHSU. He may be reached at axa153@shsu.edu

ULAN DAKEEV is an assistant professor in the Industrial Technology Department in the College of Engineering at Texas A&M University, Kingsville. His areas of research include virtual reality, augmented reality, renewable energy, quality in higher education, motivation, and engagement of students. He has served as a webmaster of the Energy Conservation and Conversion Division of the American Society for Engineering Education since 2015. Dr. Dakeev may be reached at ulan.dakeev@tamuk.edu

EVALUATION OF SEISMIC DESIGN AND BUCKLING STRENGTH OF LIQUID-FILLED STEEL CYLINDRICAL TANKS

Wiriyachai Roopkumdee, University of North Dakota; Iraj Mamaghani, University of North Dakota

Abstract

In this paper, the authors develop practical seismic design equations for estimating the buckling strength of liquid-filled cylindrical tanks subjected to earthquake loads. A pseudo-equilibrium path criterion was used to evaluate buckling strength, and finite element analysis was performed using ANSYS. The modeling method, appropriate element types, and necessary number of elements to use in subsequent numerical analyses are recommended. Characteristics of earthquake excitations play an important role in buckling strength of liquid-filled steel cylindrical tanks. Based on an extensive parametric study, seismic design equations, and design curves representing the interactions of D/t and H/D ratios for the cylindrical tanks of various geometries subjected to El Centro 1940, Parkfield 2004, and Northridge 1994 earthquakes are presented and discussed. Results revealed that the D/t ratio is an important parametric factor in the seismic buckling strength of a liquid-filled cylindrical tank. The dynamic buckling capacity of the tank decreased significantly when the D/t ratio increased. An increase in the H/D ratio also seemed to have a negative effect on the seismic buckling strength; however, its effect was less significant compared to the D/t ratio.

Introduction

Liquid storage tanks are subjected to horizontal and vertical ground accelerations during the earthquakes. Damages to petroleum storage tanks were reported due to the earthquakes of 1933 Long Beach, 1952 Kern County, 1964 Alaska, 1971 San Fernando, 1979 Imperial Valley, 1983 Coalinga, 1989 Loma Prieta, 1992 Landers, 1994 Northridge, and 1995 Kobe (Cooper & Wachholz, 1999). The American Lifelines Alliance (2005) reported that the failure modes occurred due to steel storage tanks. In this current study, the authors were interested in the shell buckling mode of liquid-filled cylindrical tanks subjected to the horizontal earthquake accelerations. The hydrodynamic behavior of liquid-filled cylindrical tanks when subjected to earthquakes can be separated into two types (Housner, 1963). First, impulsive mass, a mass of water is rigidly attached to the tank at the proper height. Second, convective mass, the horizontal accelerations from the tank excite a mass of water into oscillations. Veletsos and Yang (1977) reported that liquid-filled cylindrical tanks have a cantilever beam mode when the tanks are subjected to horizontal excitation. Housner (1963), Haroun and Housner (1981), and Veletsos and Yang (1977) reported that, when the horizontal excitations were applied to the liquid-filled cylindrical tank, a cantilever-beam mode was detected. From past earthquakes, recorded data show that tanks filled with liquid are more prone to suffering damage (American, 2005).

Sezen et al. (2008) used ANSYS to study liquefied gas-structure interaction and a simplified model of three tanks in Turkey that experienced an earthquake on August 17, 1999; they reported that shear and bending moments are overestimated if the fluid is modeled as a single rigid mass. Virella et al. (2006) presented the critical value of peak ground acceleration (PGA) for conical roof tanks subjected to horizontal acceleration using ABAQUS finite element analysis software, where the critical values of PGA for cylindrical tanks filled with liquid up to 90% of the height of the tanks were between 0.25g and 0.35g. The nature of the dynamic buckling response can be estimated using the deformations and stresses around the critical level of the earthquake excitation (Djermane, Zaoui, Labbaci, & Hammadi, 2014).

Djermane et al. (2014) and Virella et al. (2006) used Budiansky and Roth (1962) to conduct the pseudo-equilibrium path to find a significant increase rate of the deformation. This significant increase rate of deformation can be used to indicate the dynamic buckling of the steel cylindrical tanks. Kazaz et al. (2006) conducted a numerical simulation of a reinforced concrete load-bearing structural wall model subjected to effective earthquake forces. Many other studies have looked at the seismic behavior of liquid-filled steel cylindrical tanks. However, little effort has been devoted to investigating the interactive effects of D/t and H/D ratios on seismic buckling capacities when the liquid-filled steel cylindrical tanks are subjected to different earthquake excitations.

In this current study, finite element method (FEM) was used to investigate the effects of D/t and H/D ratios of the liquid-filled steel cylindrical tanks when different characteristics of earthquake loads are applied to the tanks. The structure response to the base excitation was modeled using the concept of effective earthquake forces; therefore, acceleration input was to create an acceleration field acting on all the nodes of the model. In addition, the time steps were divided such that they would be small enough to accurately capture the periods of oscillations.

Modeling of Cylindrical Tanks

Five geometric configurations of the cylindrical tanks were analyzed with height-to-diameter (H/D) ratios of 0.43, 0.67, 1.00, 1.46, and 2.41, and diameter-to-thickness (D/t) ratios of 910, 1013, 1216, 1612, and 2130, in order to investigate the buckling behaviors of various sizes of cylindrical tanks. Table 1 and Figure 1 illustrate the geometries of the cylindrical tanks. Figure 2 shows the FEA modeling of model A.

Table 1. Geometries of the cylindrical tanks.

Model	H (m)	D (m)	t (mm)	Hr (m)	H/D	D/t
A	6.1	9.1	10.0	0.853	0.67	910
B	18.3	7.6	7.5	0.713	2.41	1013
C	15.2	15.2	12.5	1.425	1.00	1216
D	20.0	13.7	8.5	1.284	1.46	1612
E	9.1	21.3	10.0	2.000	0.43	2130

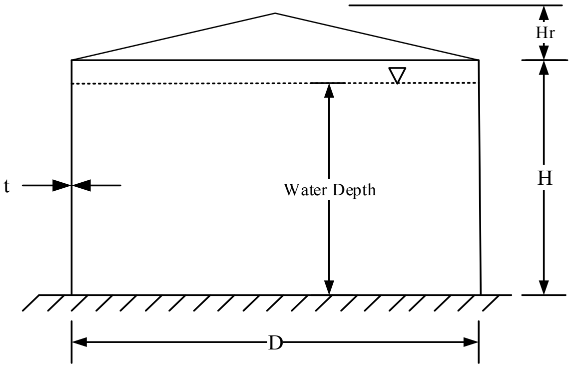

Figure 1. Cylindrical tank geometry.

The material for all cylindrical storage tanks was steel with a modulus of elasticity, E, equal to 200 GPa, a Poisson's ratio, ν, of 0.3, and a mass density, ρ, or 7850 kg/m^3. Bilinear isotropic hardening of the steel was included with the yield stress of 345 MPa and the tangent modulus of 13.79 GPa. The liquid used to fill the cylindrical tanks was water with a bulk modulus of 2068.4 MPa and a mass density of 1000 kg/m^3. For FEA modeling, all cylindrical tanks were considered fixed at the base and free on the top. The histogram of earthquake excitation, in terms of acceleration, was applied to every node of the cylindrical tanks. Therefore, the structural response to the base excitation was modeled using the concept of effective earthquake forces (Chopra, 2011), as illustrated in Figure 3.

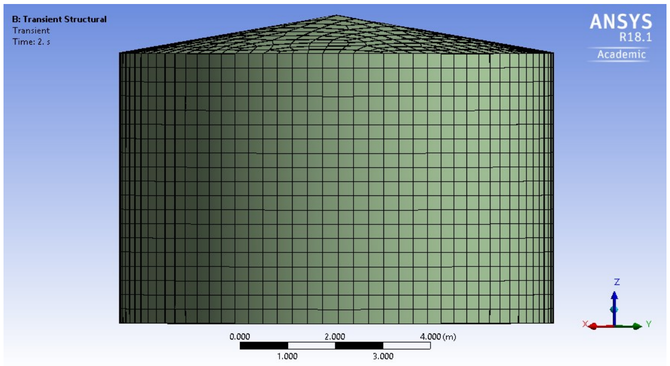

Figure 2. FEA modeling of model A.

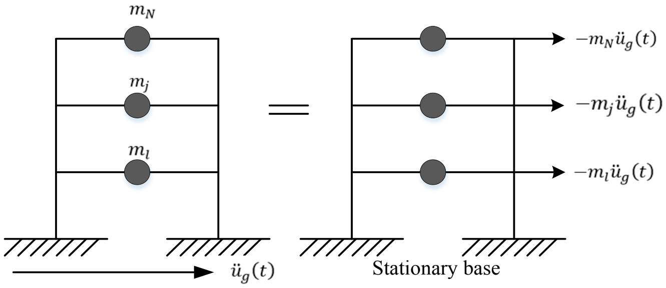

Figure 3. Ground excitation and effective earthquake forces.

ANSYS was used for all computations. SHELL181 element was used as the element for the steel cylindrical tanks. SOLID186 element was used as the element for the water inside the cylindrical tanks. SHELL181 is a four-node element with six degrees of freedom at each node (translation in x, y, and z directions, and rotation about the x, y, and z axes). SOLID186 is a higher order 3-D solid 20-node element having three degrees of freedom per node that exhibits quadratic displacement behavior (ANSYS, 2009). The elements of SHELL181 for models A, B, C, D, and E were modeled with 4174, 5513, 8838, 7941, and 7198 elements, respectively. The elements of SOLID186 for models A, B, C, D, and E were modeled with 850, 941, 1180, 1021, and 978 elements, respectively.

Damping Ratios

Rayleigh Damping is a procedure of classical damping, which is used in the ANSYS computer program. For simplicity and numerical efficiency, damping was assumed as Rayleigh mass proportional damping, as given by Equations 1 and 2:

$$[C] = a_0 [M] \tag{1}$$

$$a_0 = 2\omega_n \zeta_n \tag{2}$$

where, a_0 is mass coefficient and ζ_n is critical damping ratio.

For the steel structure, the critical damping ratio is generally between 2% and 3% (Djermane et al., 2014). In this study, a value of 2% was adopted. This mass coefficient (a_0) was to be inputted into the transient analysis to indicate the damping ratio of the structure. Table 2 shows the mass coefficients of each model.

Table 2. First natural frequencies and mass coefficients of the tanks filled with water up to 90% height.

Model	First Natural Frequency (Hz)	Mass Coefficient (a_0)
A	4.259	1.070
B	1.993	0.501
C	2.293	0.576
D	1.824	0.458
E	2.070	0.520

Nonlinear Seismic Analysis

The transient dynamic analysis can be used in FEM to study the dynamic behavior of a structure when it is subjected to time-dependent loading. Inertia and damping effects were considered for the transient dynamic analysis. The equation of motion, Equation 3, was solved by the transient structure simulation in ANSYS.

$$[M]\{\ddot{u}\} + [C]\{\dot{u}\} + [K]\{u\} = \{F_{(t)}\} \tag{3}$$

where, $[M]$ is the mass matrix; $[C]$ is the damping matrix; $[K]$ is the stiffness matrix; $\{\ddot{u}\}$ is the nodal acceleration vector; $\{\dot{u}\}$ is the nodal velocity vector; $\{u\}$ is nodal displacement; $\{F_{(t)}\}$ is the load vector; and, t is time.

Data sets of earthquake loads for El Centro 1940, Parkfield 2004, and Northridge 1994 were collected from the United States Geological Survey (Index, 2014). Numerical values of these earthquakes are in units of g. Figures 4-6 show the accelerations due to gravity for the El Centro, Parkfield, and Northridge earthquakes, respectively.

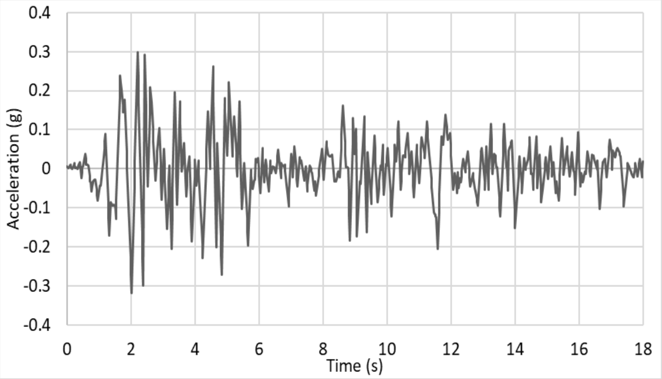

Figure 4. Accelerogram of north-south component of the El Centro earthquake, 1940.

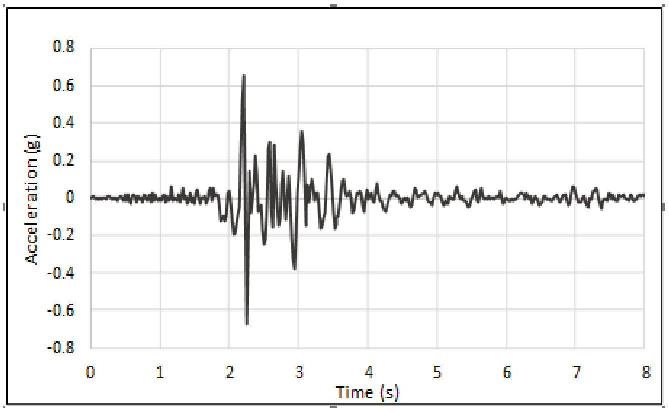

Figure 5. Accelerogram of north-south component of the Parkfield earthquake, 2004.

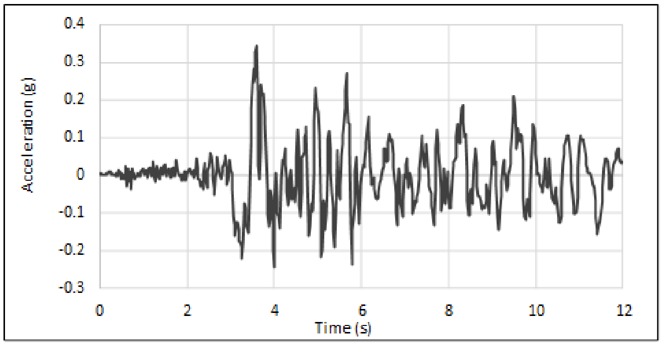

Figure 6. Accelerogram of north-south component of the Northridge earthquake, 1994.

Pseudo-Equilibrium Paths

El Centro Earthquake:

The Budiansky and Roth criterion (1962) was used to generate pseudo-equilibrium paths in this study. Buckling instability occurred when a small increase in the pulse intensity caused a strong increase in the rate of deflection. Therefore, different analyses of the structure for several loads (PGAs) had to be constructed. The node that provided maximum displacement of each model was used to find the pseudo-equilibrium path. For example, Figure 7 shows that node 2638 had a maximum displacement when PGA was 0.7g. Figure 8 illustrates the pseudo-equilibrium paths and the dynamic buckling values of models A and C. The dynamic buckling values of models A and C were 0.72g and 0.56g, respectively. Figure 9 illustrates the pseudo-equilibrium paths and the dynamic buckling values of model B. The dynamic buckling value of model B was 0.55g. Figure 10 illustrates the pseudo-equilibrium paths and the dynamic buckling values of models D and E. The dynamic buckling values of models D and E were 0.15g and 0.075g, respectively. Transient response curves, in terms of nodal displacement with an increase in PGA, were also observed in this study. Figure 11 shows a significant jump in the nodal displacement of model C, which indicated that the structure was unstable for PGA = 0.6g.

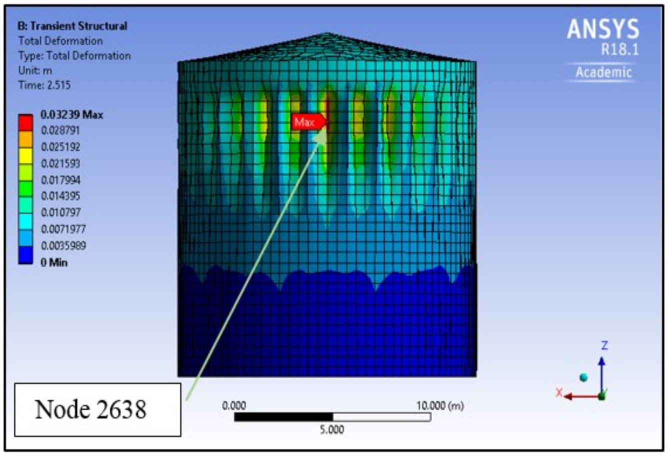

Figure 7. Deformation of model C subjected to the El Centro earthquake.

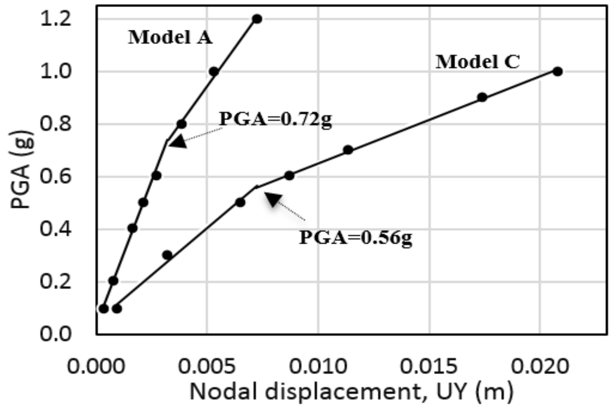

Figure 8. Pseudo-equilibrium paths for model B.

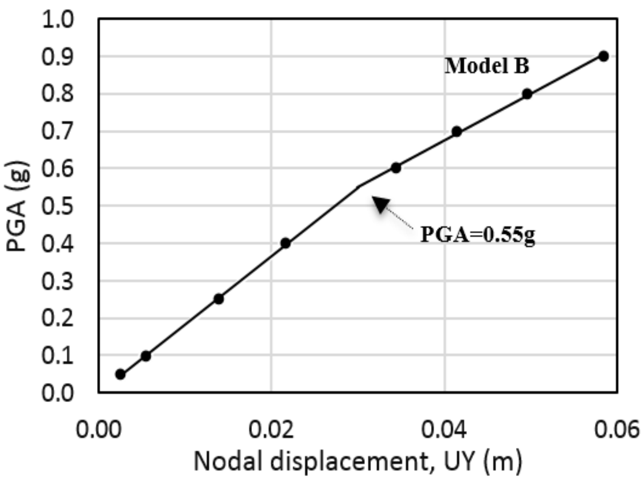

Figure 9. Pseudo-equilibrium path for models A and C.

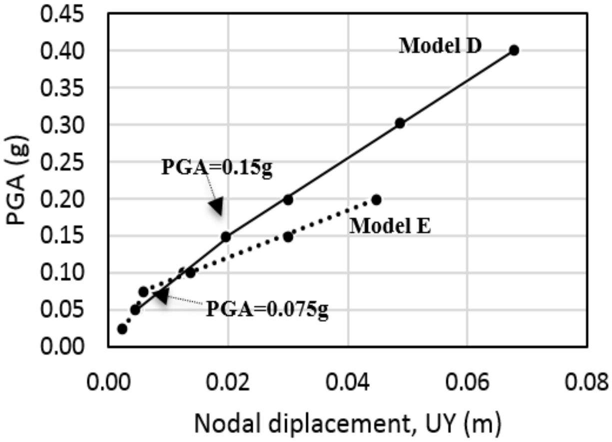

Figure 10. Pseudo-equilibrium paths for models D and E.

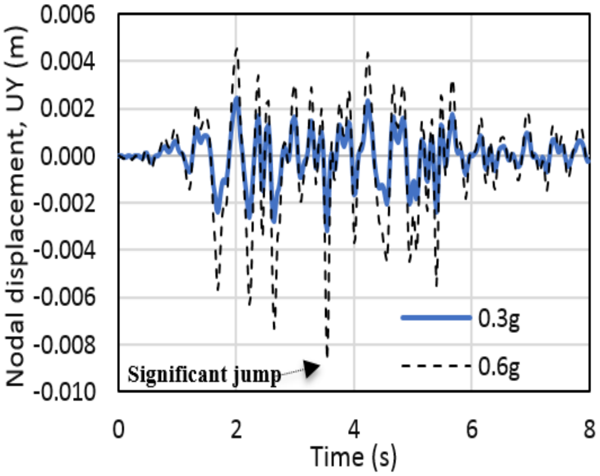

Figure 11. Transient response for model C.

Parkfield Earthquake:

The Parkfield earthquake was chosen to be one of the applied loads for studying the dynamic buckling strength of liquid-filled steel cylindrical tanks when the tanks were applied different characteristics of earthquake loads. Nodes that gave the maximum displacement to the steel cylindrical tanks when they were subjected to the Parkfield earthquake were nodes 2623, 2876, 5580, 1076, and 1436 for models A, B, C, D, and E, respectively. Figure 12 illustrates the pseudo-equilibrium path and the dynamic buckling value of model A. The dynamic buckling value of model A was 1.30g. Figure 13 illustrates the pseudo-equilibrium paths and the dynamic buckling values of models C and D. The dynamic buckling values of models C and D were 0.88g and 0.40g, respectively. Figure 14 illustrates the pseudo-equilibrium path and the dynamic buckling value of model B. The dynamic buckling value of model B was 1.20g. Figure 15 illustrates the pseudo-equilibrium path and the dynamic buckling value of model E. The dynamic buckling value of model E was 0.33g.

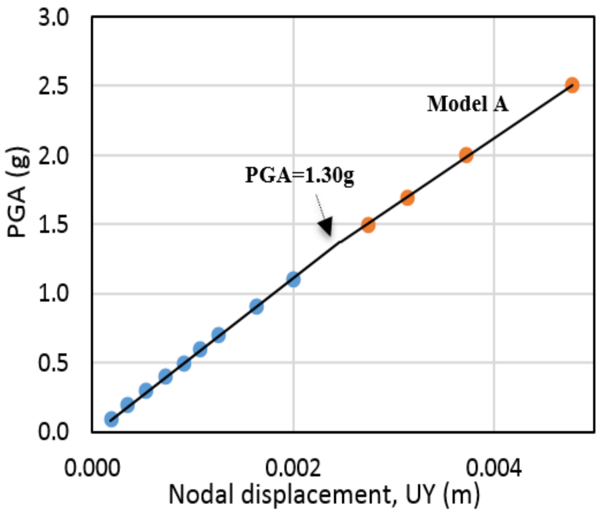

Figure 12. Pseudo-equilibrium path for models C and D.

Northridge Earthquake:

The FEM results using the El Centro and Parkfield earthquakes indicated that the dynamic buckling capacities decreased when D/t ratios increased; however, the effect of the H/D ratio could not be simplified. Thus, the Northridge earthquake was included in this study to interpret the uncertain effect of the H/D ratio. Figure 16 illustrates the pseudo-equilibrium paths and the dynamic buckling values of models A and C. The dynamic buckling values of models A and C were 1.34g and 0.70g, respectively.

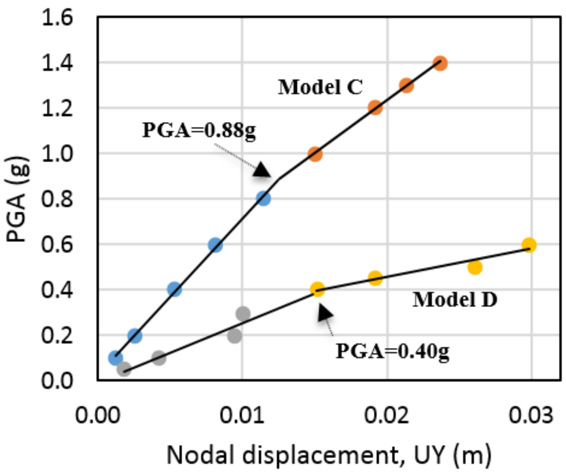

Figure 13. Pseudo-equilibrium paths for model A.

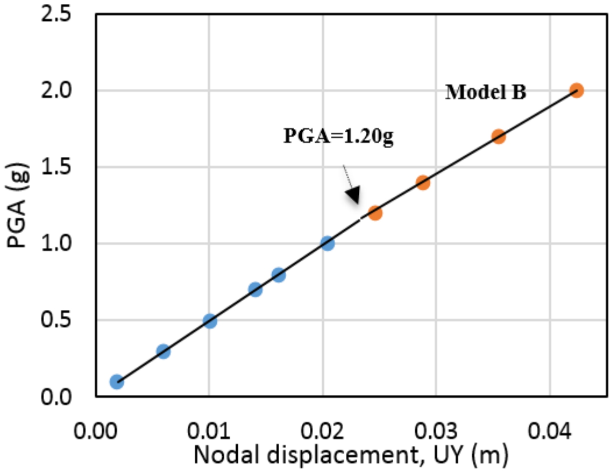

Figure 14. Pseudo-equilibrium path for model B.

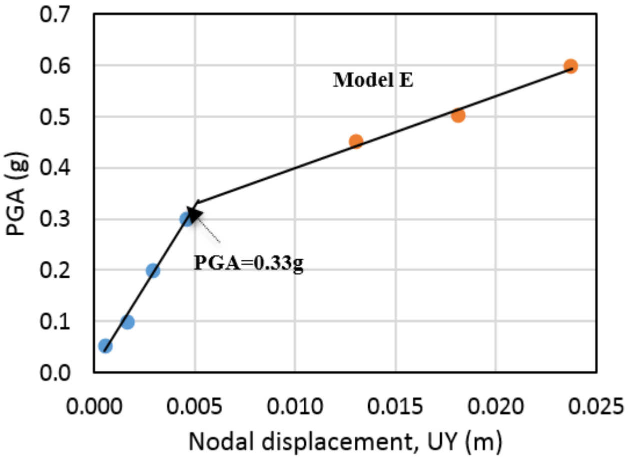

Figure 15. Pseudo-equilibrium path for model E.

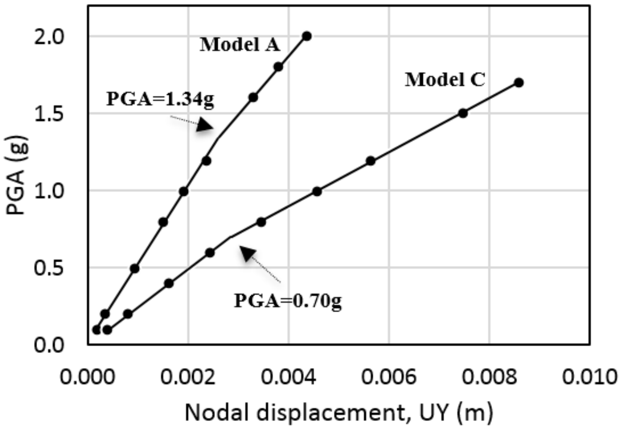

Figure 16. Pseudo-equilibrium paths for models A and C.

Figure 17 illustrates the pseudo-equilibrium path and the dynamic buckling value of model B. The dynamic buckling values of model B was 0.63g. Figure 18 illustrates the pseudo-equilibrium paths and the dynamic buckling values of models D and E. The dynamic buckling values of models D and E were 0.21g and 0.20g, respectively. Figure 19 illustrates the significant jumps from transient response curves for model D.

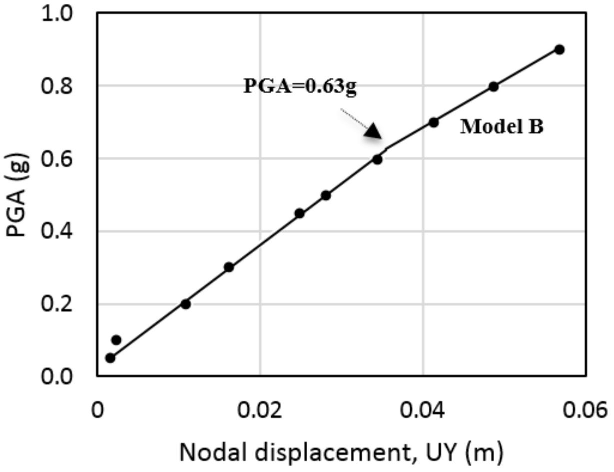

Figure 17. Pseudo-equilibrium path for model B.

Estimated Design Equation

To estimate the interaction effects of the H/D and D/t ratios on the seismic buckling strengths of the steel cylindrical tanks, a nonlinear regression analysis was adopted to estimate a design equation. From the El Centro, Parkfield, and Northridge earthquake cases, the design equation can be estimated as shown in Equation 4:

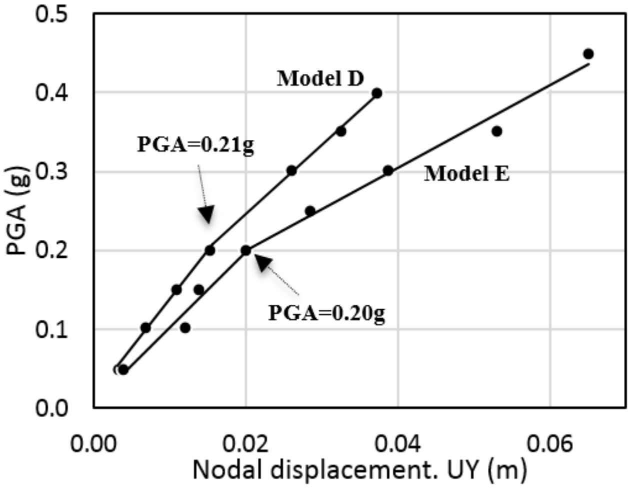

Figure 18. Pseudo-equilibrium paths for models D and E.

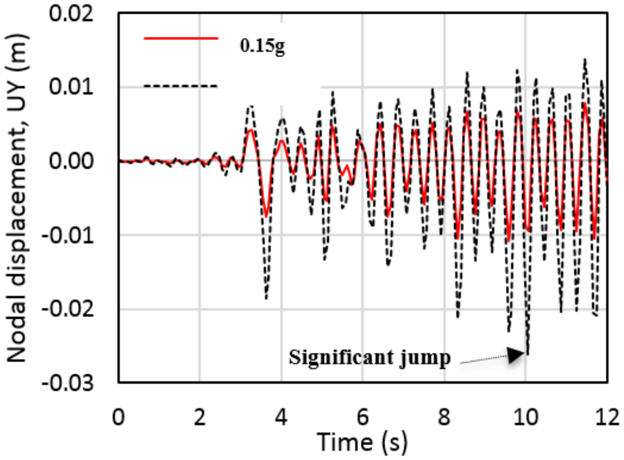

Figure 19. Transient response for model D.

$$PGA = -0.28375 \ln\left(H/D\right) - 2.93\left(10^{-7}\right)\left(D/t\right)^{2} + 1.23015;\ R^{2} = 0.7018 \tag{4}$$

From Equation 4, the D/t ratio had a significant negative effect on the dynamic buckling capacity. If the D/t ratio increased, the dynamic buckling capacity would significantly decrease. An increase in the H/D ratio also showed a negative effect on dynamic buckling capacity; however, when the H/D ratio increased, the buckling capacities would decrease at a diminishing rate. Equation 4 was estimated from geometries of the tanks based on this study. Therefore, the estimated design equation may have to be reinvestigated if the dimension of the steel cylindrical tank is not one covered in this study.

Conclusions

In this study, the authors evaluated the seismic buckling capacities of liquid-fill steel cylindrical tanks using various sizes of the steel cylindrical tanks. The interaction effects of D/t and H/D ratios on the dynamic buckling were investigated, and estimated design equations were proposed. Results showed that the D/t ratio is an important parametric factor of the seismic buckling strength of liquid-filled cylindrical tanks. The dynamic buckling capacity of the tanks decreased significantly when the D/t ratio increased. An increase in the H/D ratio also seemed to have a negative effect on the seismic buckling strength; however, its effect was less significant when compared to the D/t ratio.

References

American Lifelines Alliance. (2005, March). *Seismic guidelines for water pipelines*. Retrieved from https://www.americanlifelinesalliance.com/pdf/SeismicGuidelines_WaterPipelines_P3.pdf

ANSYS, Inc. (2009). *ANSYS training manual*. Canonsburg, PA: Ansys.

Budiansky, B., & Roth, R. S. (1962). Axisymmetric dynamic buckling of clamped shallow spherical shells. *Proceedings of the 11th International Congress of Applied Mechanics*. Munich: Springer-Verlag.

Chopra, A. K. (2011). *Dynamics of structures: Theory and application to earthquake engineering*. (4th ed.). Upper Saddle River, NJ: Prentice Hall.

Cooper, T. W., & Wachholz, T. P. (1999). Optimizing post-earthquake lifeline system reliability. *Proceedings of the 5th US Conference on Lifeline Earthquake Engineering*. Reston, VA: ASCE.

Djermane, M., Zaoui, D., Labbaci, B., & Hammadi, F. (2014). Dynamic buckling of steel tanks under seismic excitation: Numerical evaluation of code provisions. *Engineering Structures*, *70*, 181-196.

Haroun, M. A., & Housner, G. W. (1981). Earthquake response of deformable liquid storage tanks. *Journal of Applied Mechanics*, *48*(2), 411-418.

Housner, G. W. (1963). The dynamic behavior of water tanks. *Bulletin of the Seismological society of America*, *53*(2), 381-387.

Index to NSMP data sets. (2014, March 19). Retrieved from https://escweb.wr.usgs.gov/nsmp-data/

Kazaz, İ., Yakut, A., & Gülkan, P. (2006). Numerical simulation of dynamic shear wall tests: a benchmark study. *Computers & Structures*, *84*(8-9), 549-562.

Sezen, H., Livaoglu, R., & Dogangun, A. (2008). Dynamic analysis and seismic performance evaluation of above-ground liquid-containing tanks. *Engineering Structures*, *30*(3), 794-803.

Veletsos, A. S., & Yang, J. (1977). Earthquake response of liquid storage tanks. *Proceedings of the Second Engineering Mechanics Specialty Conference*. Reston, VA: ASCE.

Virella, J. C., Godoy, L. A., & Suárez, L. E. (2006). Dynamic buckling of anchored steel tanks subjected to horizontal earthquake excitation. *Journal of Constructional Steel Research*, *62*(6), 521-531.

Biographies

WIRIYACHAI ROOPKUMDEE is a PhD student in the Civil Engineering Department at the University of North Dakota. Wiriyachai Roopkumdee may be reached at wiriyachai.roopkumde@und.edu

IRAJ H.P. MAMAGHANI is an associate professor of civil engineering at the University of North Dakota. He received his BSc in Civil Engineering from Istanbul Technical University, with 1st Class Honors, in 1989. He continued his Master and Ph.D. studies at the University of Nagoya, Japan, where he obtained his Master and Doctor of Engineering degrees in Civil Engineering. Dr. Mamaghani works in the area of civil engineering with emphasis on structural mechanics and structural engineering. His areas of interest inlcude cyclic elastoplastic material modeling, structural stability, seismic design, advanced finite element analysis and ductility evaluation of steel, composite (concrete-filled steel tubular), and masonry structures. Dr. Mamaghani may be reached at iraj.mamaghani@engr.und.edu

DESIGN AND ANALYSIS OF AU AND ITO THZ ANTENNAS

Sai Dittakavi, Northern Illinois University, Ibrahim M. Abdel-Motaleb Northern Illinois University

Abstract

The terahertz gap is defined as the range from of frequencies between 0.3 THz and 3 THz, or wavelengths between 1000 and 100 µm. THz frequencies can be used in medical imaging, security, communications, scientific instrumentations, and military applications. Because THz radiation is non-ionizing, it is safe for use in medical applications. To realize the full advantages of THz radiation, efficient antennas or detectors need to be designed. In this study, the authors designed bow-tie antennas using gold (Au) and Indium Tin Oxide (ITO) on silica. The antennas were analyzed using the finite element, multi-physics program, COMSOL. Au was used for its low resistivity and ITO was used for its ability to vertically integrate with optical devices. The bow-tie antenna is composed of two triangles facing each other at the apex, with a nanometer-gap between them. This gap acts as a capacitor. The absorption of THz radiation results in the creation of an electric field across the gap. The dimensions of the antenna were changed and the electric field across the gap was calculated.

As expected, the results showed that the electric field increased with a decrease in the gap dimension. Hence, the minimum size of the gap is related to the critical dimension of the fabrication process. The results also showed that the electric field increased with metal thickness. This can be attributed to the decrease of the antenna's resistance as metal thickness increased. On the other hand, the width dimension seemed not to substantially affect the output field. This may be because the width only affects the magnetic field and does not affect the electric field measured across the gap. The increase in the length of the antenna, L, resulted in a decrease in the peak frequency, f_0. This is because f_0 is proportional to 1/L. Therefore, by combining several antennas with different lengths, a THz detector with a wider range of frequency detection can be built. The behavior of the ITO antennas was similar to the Au antenna, but with lower field values. This can be attributed to the high resistivity of ITO compared with Au.

Introduction

The terahertz region is sandwiched between the microwave and the infra-red regions. The THz spectrum offers many applications in engineering, such as medical imaging, security, communications, scientific instrumentations, and military applications (Sabaawi, Tsimenidis, & Sherif, 2013). This range is also known as the sub-mm wave range, since its wavelength falls between 1 mm and 0.1 mm (Wu, Cheng, Djerafi, & Hong, 2012). The antennas used in this study were bow-tie antennas, where a bow-tie-shaped metal was deposited on top of a dielectric substrate. The performance of the antenna was mainly affected by the dielectric strength of the substrate. Low-dielectric substrates, such as silica, have been used to build THz antennas, and their performance has been reported in the literature (Chattopadhyay, Reck, Jung-Kubiak, Lee, Siles, Chahat, Cooper, Schlecht, Alonso-delPino, & Mehdi, 2014; Llombart, Lee, Alonso-delPino, Chattopadhyay, Jung-Kubiak, Jofre, & Mehdi, 2013; Hou, Xiong, Hong, Goh, & Chen, 2012).

The metal used to build THz antennas is normally gold (Au). Gold is chosen because it is biocompatible and has a very high conductivity. On the other hand, Au is opaque in the optical spectrum. Hence, vertical integration with optical/optoelectronic devices may be adversely affected. Using a transparent metal may provide the advantage of vertical integration with optical devices. Indium-Tin-Oxide (ITO) can provide this advantage, if used as a metal for the antenna. ITO is a transparent, wide bandgap, degenerate semiconductor, with very high conductivity. Therefore, ITO can act as a metal. In this study, a bow-tie nano-antenna made of ITO on silica was designed and analyzed using finite element numerical analysis in the THz range. Silica can have dielectric constants as low as 2.03, if not lower. For comparison, a similar antenna using Au on silica was also designed and analyzed using the same numerical analysis. The wide bandgap of ITO allows almost all infrared and visible light photons to be transmitted through. To the best knowledge of the authors, there is no publication of a similar THz antenna having been built using ITO on silica.

Analysis

The COMSOL multi-physics program was used to conduct the study. The bow-tie antenna shape has previously been studied by many research groups (Wu, Le-Wei, & Liu, Geometric, 2010; Wu, Le-Wei, & Liu, Gold, 2010; Sabaawi, Tsimenidis, & Sherif, 2012) and was shown to exhibit enhanced performance. Figure 1 shows that this antenna is basically two triangles with a nano-gap between the vertices. The antenna has 16 µm length, 9 µm width, 1µm thickness, and a 100-nm gap between the two apexes. Figure 2 shows the simulation geometry with the various boundaries used in the COMSOL simulation. Also shown in Figure 2 is how the antenna is placed on top of a 20-µm silica substrate. On the top of the antenna, a 20-µm column of air was placed. To avoid reflections from the boundaries, a perfectly matched layer (PML) with a thickness of 10 µm was used on the top and under the bottom of the model (Hou et al., 2012). The antenna was illuminated vertically by an electromagnetic wave using COMSOL's feature port that applied 1 V/m magnitude propagating in the Z-direction. The port was excited with an electric source placed 20 µm above the antenna metal and just below the upper PML layer.

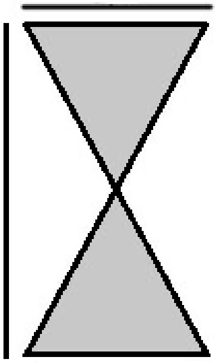

(a) Geometry of the bow-tie antenna used in this study.

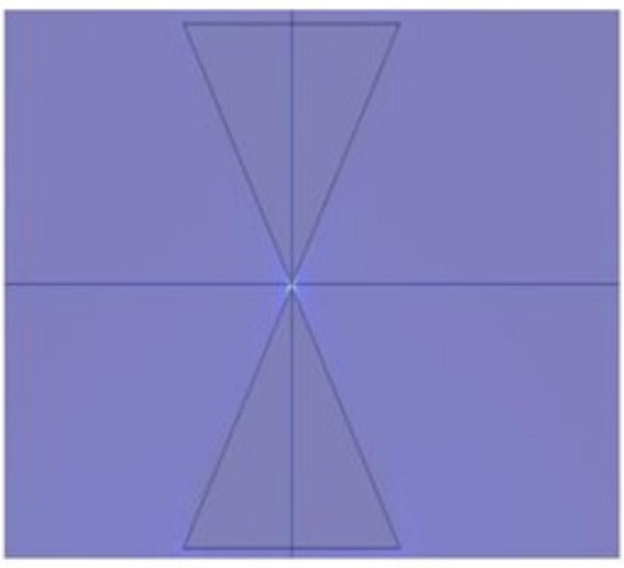

(b) COMSOL simulation of the electric field showing the highest intensity across the gap.

Figure 1. The bow-tie antenna.

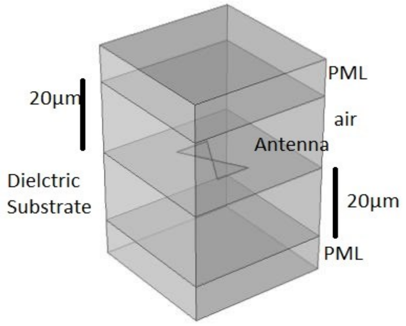

Figure 2. A 3-D view of the geometry and domains simulated in COMSOL with a perfectly matched layer (PML) on the top and at the bottom.

The dielectric constant was obtained for the metal from the Drude model, given by Equation 1 (Ordal, Long, Bell, Bell, Alexander, & Ward, 1983):

$$\varepsilon(\omega) = \varepsilon_{\infty} - \frac{\omega_p^2}{\omega^2 - j\omega_\tau} \tag{1}$$

where, ε_∞ represents the contribution of the bound electrons to the relative dielectric constant; ω_p is the plasma frequency; and, ω_τ is the damping frequency.

The dielectric parameter is a complex value, since it depends on the frequency (see again Equation 1). COMSOL uses Equation 1 to obtain the complex dielectric value at different frequencies (Gonzalez, Alda, Simon, Ginn, & Boreman, 2009). As noted earlier, in order to eliminate reflection, PMLs were used. The PML is not a boundary condition but rather an additional domain that absorbs incident waves without producing reflections. The captured electric field at the gap was the output of the nano-antenna. In COMSOL, Maxwell's equations (Equation 2) were used to obtain the electric field:

$$\nabla \cdot \mu_r^{(-1)}(\nabla \cdot E) - k_0^2 \varepsilon_r E = 0 \tag{2}$$

where, μ_r is the relative permeability; ε_r is the relative dielectric constant; k_0 is the wave number equal to (ω/c); ω is the radial frequency; and, c is the speed of light.

The gap between the two triangles of the bow-tie dipole antenna affects the performance of the antenna. The electric field is created at gap of the antenna due to Coulomb's field. In this case, the gap acts as a capacitor (Sabaawi, Tsimenidis, & Sherif, 2012). Therefore, the gap dimension affects the antenna's performance, as will be explained later.

Results and Discussion

To ensure that the current simulation was correct, the results of simulations for the bow-tie Au/silica antenna published by Sabaawi, Tsimenidis, Sherif (2012) were compared with the simulation in this current study. In this simulation, the conductivity of Au was taken to be 45.6x10^6 S/m and the dielectric constant equal to the complex value -8.49+1.62j. For silica, the dielectric constant was assumed to be 2.03, and the resonant frequency was 5.57 THz. Figure 3(a) shows the published results; Figure 3(b) shows the results of this current study. As can be seen from the figures, the current simulation results are almost identical to the published results. The match between the two results provides the necessary confidence in the reliability of the current analysis and results.

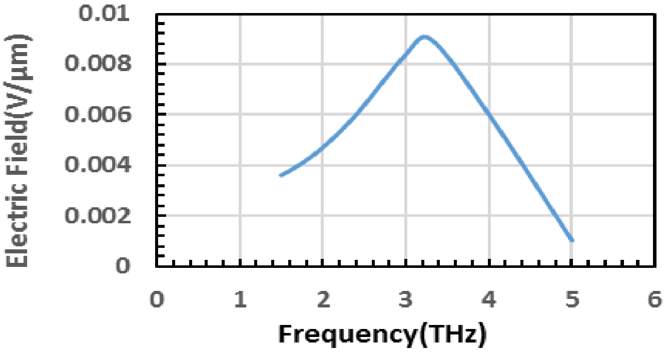

(a) Output of Au/silica antenna reported by Sabaawi, Tsimenidis, & Sherif, 2012.

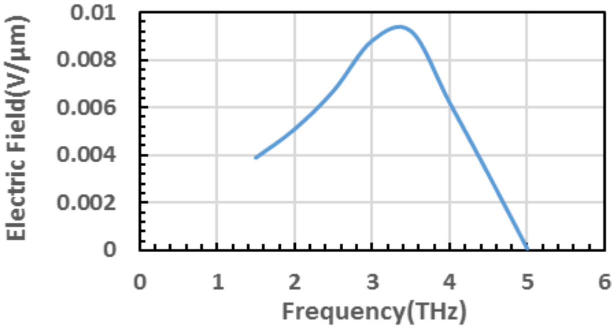

(b) Output of Au/silica antenna from this study.

Figure 3. Antenna output.

Next, ITO and Au antennas on silica substrates were analyzed. For ITO, the conductivity was taken to be 1.3x10^4 S/m and the dielectric constant to be 3.37+0.01j. The two antennas were simulated using gap spacings of 100, 200, 300, 400, and 500 nm. The results showed that the electric field increased with the decrease of the gap separation. Figure 4 (a) shows the electric field as a function of the gap separation for the Au/silica antenna, and Figure 4(b) shows the same results for the ITO/silica antenna. The two figures show also that the resonant frequency does not change with the gap separation. This is because the resonant frequency is independent of this gap dimension. The highest electrical field was found to be at 100 nm and the lowest at 500 nm. The maximum electric field strength can be obtained at the minimum gap dimension, which was determined by the minimum line-width of the fabrication process used. The increase of the field with the decrease of the gap can be attributed to the fact that the electric field is the potential over the gap distance; consequently, as the gap decreased, the electric field strength increased.

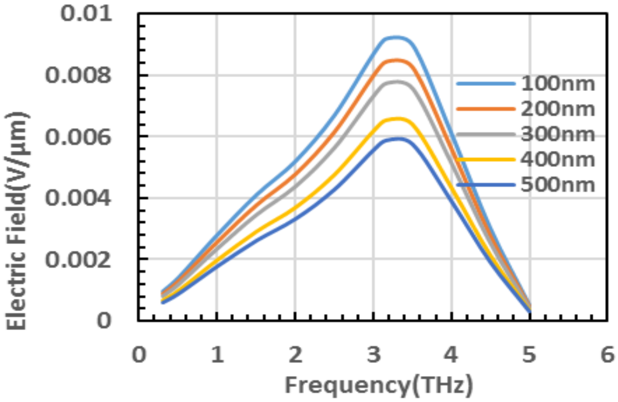

(a) Au/silica antenna.

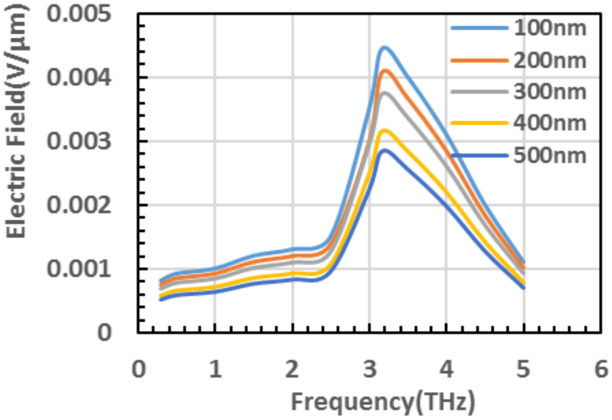

(b) ITO/silica antenna.

Figure 4. Electric Field as a function of the gap separation.

The antennas' performance was then analyzed for different metal thicknesses, but with the original width, length, and gap dimensions. The simulation was done using thicknesses of 0.2, 0.5, 1, 3, and 5 µm. Figure 5(a) shows the results of the study for the Au antenna, and Figure 5(b) for the ITO antenna. For both antennas, a higher thickness resulted in a higher output field. The skin depth for the metals was found to have no effect, since it was found to be much smaller than the minimum thickness used. The resonant frequencies of the Au and ITO antennas were the same, indicating that this frequency is independent of the metal's thickness. Therefore, the increase in the electric field with the thickness might be attributed to the increase of the metal's conductance.

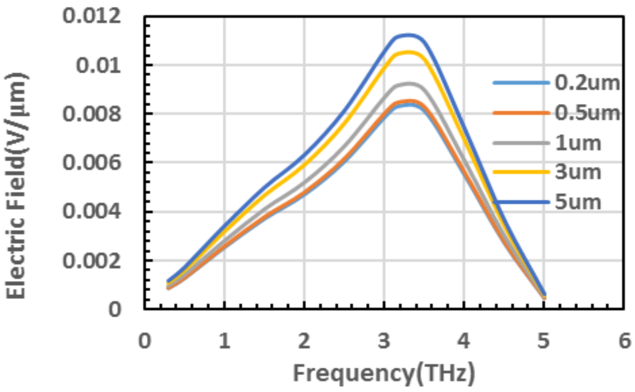

(a) Au/silica antenna.

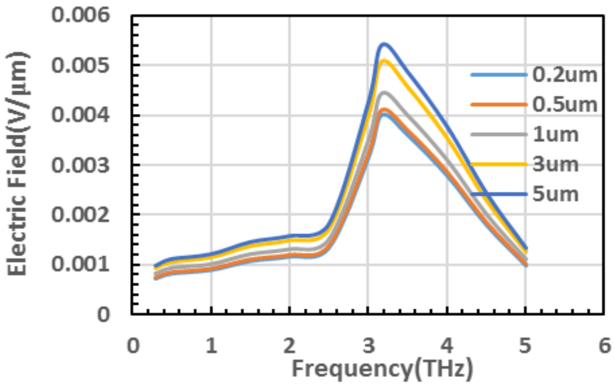

(b) ITO/silica antenna.

Figure 5. Electric Field as a function of the thickness.

The investigation next focused on the effect of the width dimension on the antenna's response. The antennas were simulated with widths of 2, 4, 9, 10, and 12 µm. Figure 6(a) shows the results for the Au antenna, while Figure 6(b) shows the results for the ITO antenna. The two figures show that the electric field strength was almost invariant with the width. This can be attributed to the fact that the applied electromagnetic wave has the magnetic field parallel to the width and the electric field parallel to the length. This means that the width dimension affects only the magnetic field, and the length dimension only affects the electric field. Therefore, the electric field stays constant with the width variation. Figure 6(a) shows the electric field as a function of the width dimension for the Au/silica antenna (left), and Figure 6(b) shows the same for the ITO/silica antenna (right). The impact of the length on the output electric field was also investigated. The antennas were simulated using lengths of 25 µm, 20 µm, 16 µm, 12 µm, and 8 µm, as shown in Figure 7.

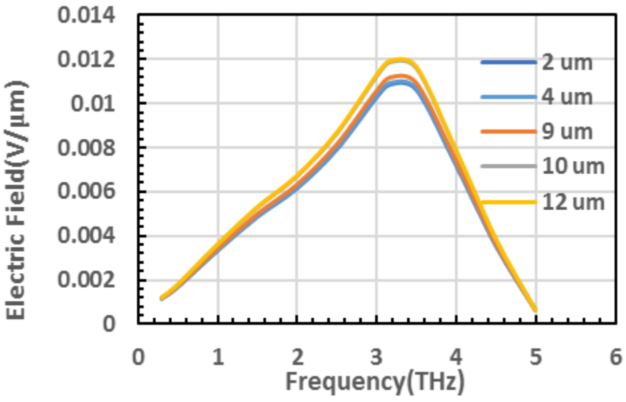

(a) Au/silica antenna.

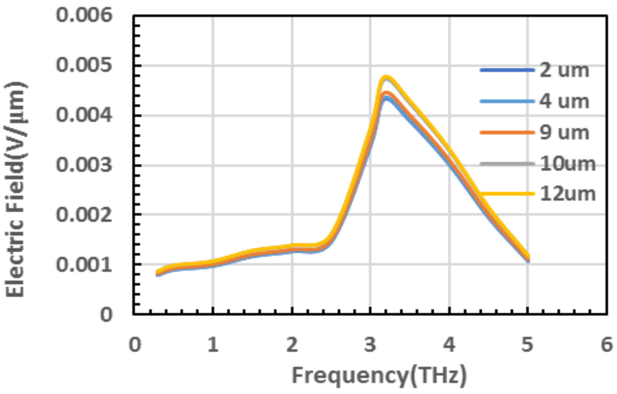

(b) ITO/silica antenna.

Figure 6. Electric Field as a function of the width dimension.

In an antenna, there may exist multiple peaks, since these antennas resonate at frequencies f_0/n^2, f_0/n, f_0, nf_0, n^2f_0, where n is an integer and f_0 is the fundamental frequency. The resonant frequency, in this case, can be obtained from Equation 3:

$$f_0 = \frac{c}{2 \cdot L \cdot \sqrt{\varepsilon_{eff}}} \tag{3}$$

where, c is the speed of light; L is the length of the antenna; and, ε_{eff} is the effective dielectric constant at f_0.

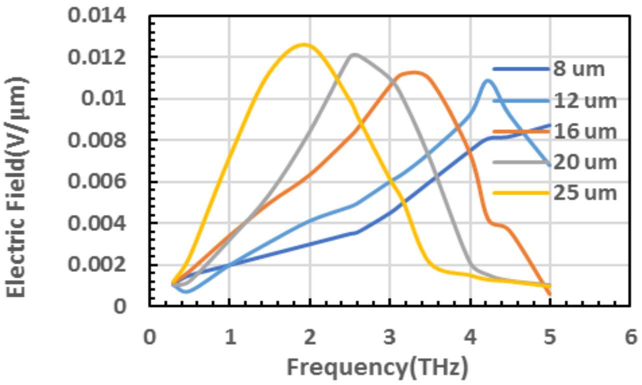

(a) Au/silica antenna.

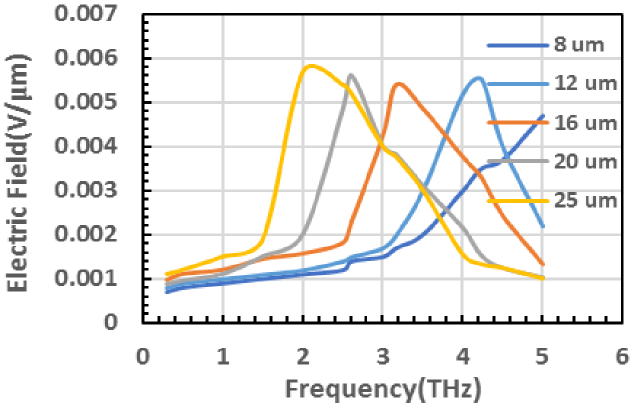

(b) ITO/silica antenna.

Figure 7. Electric Field as a function of the length.

Using a dielectric constant of 2.03 for the silica and a length of 16 μm, the resonant frequencies obtained using Equation 3 were found to be 6.58 THz. This fundamental resonant frequency is not shown, because it lies outside the simulation range for this study, which was from 0.3-5.0 THz. However, a secondary resonant frequency would be $f_0/2$=3.29 THz. Figure 4 shows that this value was in full agreement with the value obtained from the simulation. Equation 3 also shows that the resonant frequency does not depend on the width, but rather on the length. Figure 7 (a) shows the simulation results for the Au antenna, and Figure 7(b) shows the results for the ITO antenna with different lengths. The simulation results show that the resonant frequency depends on the length. The results further show that the resonant frequencies for both antennas were about 2.1 THz, 2.63 THz, 3.29 THz, and 4.38 THz, for the lengths 25 μm, 20 μm, 16 μm, and 12 μm, respectively. For the length 8 μm, the resonant frequency was 6.58 THz, which lies outside the simulation range.

The results given in Figures 3-7 indicate that the electric field for Au antennas was higher than that for the ITO antennas. The reason for this can be attributed to the high conductivity of Au (45.6x10^6 S/m) compared to that of ITO (1.3x10^4 S/m). The value of the electric field and the voltage across the gap were proportional to the accumulated charge density generated by the absorption of the incident wave. The voltage across the gap, as well as the electric field, increased if the antenna's internal resistance decreased. Therefore, it was believed that high metal conductivity contributes to an increase in the electric field.

Conclusions

Au/silica and ITO/silica bow-tie antennas were successfully designed and analyzed using different dimensions. ITO antennas can be used for vertical integration of optical and optoelectronic devices. Au/silica antennas can provide higher outputs. This study showed that these antennas can be used as bandpass filters, allowing the detection of a narrow band of signals. Using an integrated array, the output strength can be increased several-fold. Assuming the area of each antenna to be 50 μm x 50 μm, one can place an array of 40,000 antennas in one cm^2, increasing the field by the same value. For space exploration, the antenna array can be in square meters. The array can detect wideband signals if it is composed of antennas with different lengths. The change in length will shift the resonant frequency, resulting in a wider range of detection. In this study, the authors focused only on a normal application of the electromagnetic waves. However, by changing the incident angles, the antenna's response can be expected to change. Such a study may explore other properties of bow-tie antennas that were not explored in this study.

References

Chattopadhyay, G., Reck, T., Jung-Kubiak, C., Lee, C., Siles, J., Chahat, N., Cooper, K., Schlecht, E., Alonso-delPino, M., & Mehdi, I. (2014). Terahertz antennas with silicon micromachined front-end. *Proceedings of the 8th European Conference on Antennas and Propagation*. Brussels, Belgium: EurAAP.

Gonzalez, F. J., Alda, J., Simon, J., Ginn, J., & Boreman, G. (2009). The effect of metal dispersion on the resonance of antennas at infrared frequencies. *Infrared Physics and Technology*, *52*(1), 48-51.

Hou, D., Xiong, Y.-Z., Hong, W., Goh, W. L., & Chen, J. (2012). Silicon-based on-chip antenna design for millimeter-wave/THz applications. *Proceedings of the 2011 IEEE Electrical Design of Advanced*

Packaging and Systems Symposium. Piscatawny, NJ: IEEE.

Llombart, N., Lee, C., Alonso-delPino, M., Chattopadhyay, G., Jung-Kubiak, C., Jofre, L., & Mehdi, I. (2013). Silicon micromachined lens antenna for THz integrated heterodyne arrays. *IEEE Transactions on Terahertz Science and Technology*, *3*(5), 515-523.

Ordal, M. A., Long, L. L., Bell, R. J., Bell, S. E., Alexander, Jr., R. W., & Ward, C. A. (1983). Optical properties of the metals Al, Co, Cu, Au, Fe, Pb, Ni, Pd, Pt, Ag, W, and Ti in the infrared and far infrared. *Applied Optics*, *22*, p. 1099.

Sabaawi, M. A., Tsimenidis, C. C., & Sherif, B. S. (2012). Bow-tie nano-array rectenna: Design and optimization. *Proceedings of the 6th European Conference on Antennas and Propagation*. Piscatawny, NJ: IEEE.

Sabaawi, M. A., Tsimenidis, C. C., & Sherif, B. S. (2013, September). Planar bowtie nanoarray for THz energy detection. *IEEE Transactions on Terahertz Science and Technology*, *3*(5), 524-530.

Wu, K., Cheng, Y. J., Djerafi, T., & Hong, W. (2012). Substrate-integrated millimeter-wave and terahertz antenna technology. *Proceedings of the IEEE*, *100* (7), 2219-2232.

Wu, Y. M., Le-Wei, L., & Liu, B. (2010). Geometric effects in designing bow-tie nanoantenna for optical resonance investigation. *Proceedings of the IEEE Asia-Pacific Symposium on Electromagnetic Compatibility*. Piscatawny, NJ: IEEE.

Wu, Y. M., Le-Wei, L., & Liu, B. (2010). Gold bow-tie shaped aperture nanoantenna: Wide band near-field resonance and far-field radiation. *IEEE Transactions on Magnetics*, *46*(6), 1918-1921.

Biographies

SAI MARUTHI RAM DITTAKAVI is pursuing his Master of Science in Electrical Engineering degree at Northern Illinois University. He holds a BTech in Electrical and Electronics Engineering from Lakireedy Balireddy College of Engineering, JNTUK, INDIA. His areas of interest include semi-conductor fabrication, MEMS sensors, and control engineering. Sai Dittakavi may be reached at sdittakavi@niu.edu

IBRAHIM M. ABDEL-MOTALEB, Ph.D., PE, is a professor of electrical engineering and the director of the microelectronics laboratory at Northern Illinois University. He holds BS degrees in Electrical Engineering and Physics, both from Cairo University. He received his MS degree in physics from the University of Manitoba, Canada, and his PhD in electrical engineering from the University of British Columbia, Canada. His areas of expertise include fabrication, characterization, modeling of electronic devices and integrated circuits, electronic material growth and characterization, MEMS design and fabrication, and biomedical engineering instrumentation. Dr. Ibrahim may be reached at ibrahim@niu.edu

INSTRUCTIONS FOR AUTHORS: MANUSCRIPT FORMATTING REQUIREMENTS

The INTERNATIONAL JOURNAL OF MODERN ENGINEERING is an online/print publication designed for Engineering, Engineering Technology, and Industrial Technology professionals. All submissions to this journal, submission of manuscripts, peer-reviews of submitted documents, requested editing changes, notification of acceptance or rejection, and final publication of accepted manuscripts will be handled electronically. The only exception is the submission of separate high-quality image files that are too large to send electronically.

All manuscript submissions must be prepared in Microsoft Word (.doc or .docx) and contain all figures, images and/or pictures embedded where you want them and appropriately captioned. Also included here is a summary of the formatting instructions. You should, however, review the sample Word document on our website (http://ijme.us/formatting_guidelines/) for details on how to correctly format your manuscript. The editorial staff reserves the right to edit and reformat any submitted document in order to meet publication standards of the journal.

The references included in the References section of your manuscript must follow APA-formatting guidelines. In order to help you, the sample Word document also includes numerous examples of how to format a variety of scenarios. Keep in mind that an incorrectly formatted manuscript will be returned to you, a delay that may cause it (if accepted) to be moved to a subsequent issue of the journal.

1. **Word Document Page Setup:** Two columns with ¼" spacing between columns; top of page = ¾"; bottom of page = 1" (from the top of the footer to bottom of page); left margin = ¾"; right margin = ¾".
2. **Paper Title:** Centered at the top of the first page with a 22-point Times New Roman (Bold), small-caps font.
3. **Page Breaks:** Do not use page breaks.
4. **Figures, Tables, and Equations:** All figures, tables, and equations must be placed immediately after the first paragraph in which they are introduced. And, each must be introduced. For example: “Figure 1 shows the operation of supercapacitors.” “The speed of light can be determined using Equation 4:”
5. **More on Tables and Figures:** Center table captions above each table; center figure captions below each figure. Use 9-point Times New Roman (TNR) font. Italicize the words for table and figure, as well as their respective numbers; the remaining information in the caption is not italicized and followed by a period—e.g., “*Table 1*. Number of research universities in the state.” or “*Figure 5*. Cross-sectional aerial map of the forested area.”
6. **Figures with Multiple Images:** If any given figure includes multiple images, do NOT group them; they must be placed individually and have individual minor captions using, “(a)” “(b)” etc. Again, use 9-point TNR.
7. **Equations:** Each equation must be numbered, placed in numerical order within the document, and introduced—as noted in item #4.
8. **Tables, Graphs, and Flowcharts:** All tables, graphs, and flowcharts must created directly in Word; tables must be enclosed on all sides. The use of color and/or highlighting is acceptable and encouraged, if it provides clarity for the reader.
9. **Textboxes:** Do not use text boxes anywhere in the document. For example, table/figure captions must be regular text and not attached in any way to their tables or images.
10. **Body Fonts:** Use 10-point TNR for body text throughout (1/8" paragraph indention); indent all new paragraphs as per the images shown below; do not use tabs anywhere in the document; 9-point TNR for author names/affiliations under the paper title; 16-point TNR for major section titles; 14-point TNR for minor section titles.

Incorrect

Correct

11. **Personal Pronouns:** Do not use personal pronouns (e.g., “we” “our” etc.).
12. **Section Numbering:** Do not use section numbering of any kind.
13. **Headers and Footers:** Do not use either.

14. **References in the Abstract:** Do NOT include any references in the Abstract.

15. **In-text Referencing:** For the first occurrence of a given reference, list all authors—last names only—up to seven (7); if more than seven, use "et al." after the seventh author. For a second citation of the same reference—assuming that it has three or more authors—add "et al." after the third author. Again, see the sample Word document for specifics.

16. **More on In-Text References:** If you include a reference on any table, figure, or equation that was not created or originally published by one or more authors on your manuscript, you may not republish it without the expressed, written consent of the publishing author(s). The same holds true for name-brand products.

17. **End-of-Document References Section:** List all references in alphabetical order using the last name of the first author—last name first, followed by a comma and the author's initials. Do not use retrieval dates for websites.

18. **Author Biographies:** Include biographies and current email addresses for each author at the end of the document.

19. **Page Limit:** Manuscripts should not be more than 15 pages (single-spaced, 2-column format, 10-point TNR font).

20. **Page Numbering:** Do not use page numbers.

21. **Publication Charges:** Manuscripts accepted for publication are subject to mandatory publication charges.

22. **Copyright Agreement:** A copyright transfer agreement form must be signed by all authors on a given paper and submitted by the corresponding author before that paper will be published. Two versions of the form will be sent with your manuscript's acceptance email.

    Only one form is required. Do not submit both forms!

    The form named "paper" must be hand-signed by each author. The other form, "electronic," does not require hand signatures and may be filled out by the corresponding author, as long as he/she receives written permission from all authors to have him/her sign on their behalf.

23. **Submissions:** All manuscripts and required files and forms must be submitted electronically to Dr. Philip D. Weinsier, manuscript editor, at philipw@bgsu.edu.

24. **Published Deadlines:** Manuscripts may be submitted at any time during the year, irrespective of published deadlines, and the editor will automatically have your manuscript reviewed for the next-available issue of the journal. Published deadlines are intended as "target" dates for submitting new manuscripts as well as revised documents. Assuming that all other submission conditions have been met, and that there is space available in the associated issue, your manuscript will be published in that issue if the submission process—including payment of publication fees—has been completed by the posted deadline for that issue.

    Missing a deadline generally only means that your manuscript may be held for a subsequent issue of the journal. However, conditions exist under which a given manuscript may be rejected. Always check with the editor to be sure. Also, if you do not complete the submission process (including all required revisions) within 12 months of the original submission of your manuscript, your manuscript may be rejected or it may have to begin the entire review process anew.

CUTTING EDGE JOURNAL OF RESEARCH AND INNOVATION IN ENGINEERING

www.ijeri.org

Print ISSN: 2152-4157
Online ISSN: 2152-4165

www.iajc.org

INTERNATIONAL JOURNAL OF ENGINEERING RESEARCH AND INNOVATION

ABOUT IJERI:

- IJERI is the second official journal of the International Association of Journals and Conferences (IAJC).
- IJERI is a high-quality, independent journal steered by a distinguished board of directors and supported by an international review board representing many well-known universities, colleges, and corporations in the U.S. and abroad.
- IJERI has an impact factor of **1.58**, placing it among an elite group of most-cited engineering journals worldwide.

OTHER IAJC JOURNALS:

- The International Journal of Modern Engineering (IJME)
  For more information visit www.ijme.us
- The Technology Interface International Journal (TIIJ)
  For more information visit www.tiij.org

IJERI SUBMISSIONS:

- Manuscripts should be sent electronically to the manuscript editor, Dr. Philip Weinsier, at philipw@bgsu.edu.

  For submission guidelines visit
  www.ijeri.org/submissions

TO JOIN THE REVIEW BOARD:

- Contact the chair of the International Review Board, Dr. Philip Weinsier, at philipw@bgsu.edu.

  For more information visit
  www.ijeri.org/editorial

INDEXING ORGANIZATIONS:

- IJERI is currently indexed by 16 agencies. For a complete listing, please visit us at www.ijeri.org.

Contact us:

Mark Rajai, Ph.D.

Editor-in-Chief
California State University-Northridge
College of Engineering and Computer Science
Room: JD 4510
Northridge, CA 91330
Office: (818) 677-5003
Email: mrajai@csun.edu

www.tiij.org

www.ijme.us

THE LEADING JOURNAL OF ENGINEERING, APPLIED SCIENCE AND TECHNOLOGY

The latest impact factor (IF) calculation (Google Scholar method) for IJME of 3.0 moves it even higher in its march towards the top 10 engineering journals.

IJME IS THE OFFICAL AND FLAGSHIP JOURNAL OF THE
INTERNATIONAL ASSOCATION OF JOURNALS AND CONFERENCE (IAJC)
www.iajc.org

The International Journal of Modern Engineering (IJME) is a highly-selective, peer-reviewed journal covering topics that appeal to a broad readership of various branches of engineering and related technologies. IJME is steered by the IAJC distinguished board of directors and is supported by an international review board consisting of prominent individuals representing many well-known universities, colleges, and corporations in the United States and abroad.

IJME Contact Information

General questions or inquiries about sponsorship of the journal should be directed to:

Mark Rajai, Ph.D.
Editor-in-Chief
Office: (818) 677-5003
Email: editor@ijme.us
Department of Manufacturing Systems Engineering & Management
California State University-Northridge
18111 Nordhoff St.
Northridge, CA 91330